Dissertation

submitted to the
Combined Faculties of Natural Sciences
and Mathematics
of the Ruperto-Carola University of Heidelberg, Germany
for the degree of
Doctor of Natural Sciences

Put forward by

Sergej Lebedev

Born in: St. Petersburg, Russia

Oral examination: 30.06.2021

Motion Compensation

in Cardiac X-Ray Computed Tomography

Referees: Prof. Dr. Peter Bachert

Prof. Dr. Marc Kachelrieß

Motion Compensation in Cardiac X-Ray Computed Tomography

Motion artifacts in cardiac CT remain an issue that can degrade image quality. In addition to artifacts originating from cardiac motion in general, irregular motion in particular may lead to unique artifacts for scanners with partial coverage of the heart. If multiple sub-volumes, or stacks, have to be reconstructed to cover the heart, irregular motion may introduce discrepancies between these stacks. The resulting artifacts in the finally assembled CT volume are, herein, referred to as stack transition artifacts. A stack transition artifact removal (STAR) method based on symmetric image registration was developed. The registration computed a smooth motion vector field using data from the overlap of neighboring stacks. The extent of the vector field smoothing was set automatically for individual registration tasks. Furthermore, a motion compensation (MoCo) was developed to address the general motion artifacts in short-scan data. This method is based on partial angle reconstructions to which a 4D motion model is applied. The latter was optimized using a cost function consisting of a penalized image entropy. The penalties refer to cardiac velocity and strain. Both methods were applied to single-phase reconstructions from clinical data. In addition, simulations were used with STAR. STAR considerably improved image quality. Discontinuities were removed or clearly reduced. The MoCo improved image quality for all artifact impaired reconstructions. In case of artifact-free images, image quality was maintained, however, a tendency for a minor blurring in the motion-compensated images was observed. Finally, both artifact correction methods showed a capability to clearly improve image quality.

Bewegungskompensation in der Röntgen-Computertomographiebildgebung des Herzens

Bewegungsartefakte in der CT-Bildgebung des Herzens können zu einer Reduktion der Bildqualität führen. Zusätzlich zu direkt von der Herzbewegung erzeugten Artefakten, kann irreguläre Bewegung zu einer speziellen Art von Artefakten bei CT-Geräten mit einer partiellen Abdeckung des Herzens führen. Werden mehrere Teilrekonstruktionen (Stacks) zur Abdeckung des Herzens benötigt, kann irreguläre Bewegung zu Diskrepanzen zwischen den Stacks führen. Die resultierenden Artefakte im final zusammengesetzten CT-Volumen werden folgend als Stackübergangsartefakte bezeichnet. Ein Stack-Transition-Artifact-Removal (STAR), basierend auf symmetrischer Bildregistrierung wurde entwickelt. Die Registrierung berechnet unter Nutzung von Daten aus dem Überlapp benachbarter Stacks glatte Bewegungsvektorfelder. Die Stärke der Vektorfeldglättung wird dabei automatisch angepasst. Weiterhin wurde eine Bewegungskompensationsmethode/Motion Compensation (MoCo) zur Korrektur der direkten Bewegungsartefakte in Kurz-Scan-Daten entwickelt. Diese basiert auf Teil-Winkel-Rekonstruktionen, auf die ein 4D-Bewegungsmodell angewandt wird. Das Modell wird mithilfe einer regularisierten Bildentropie als Kostenfunktion optimiert. Die Regularisierung bezieht sich auf die Geschwindigkeit und die Dehnung/Stauchung im Herz. Beide Methoden wurden auf einphasigen Rekonstruktionen aus klinischen Daten angewendet. Für STAR wurden zusätzlich Simulationen durchgeführt. STAR verbesserte die Bildqualität erheblich. Die Diskrepanzen wurden entfernt oder deutlich reduziert. Die MoCo verbesserte die Bildqualität in allen artefaktbehafteten Bildern. Bei artefaktfreien Fällen wurde die Bildqualität beibehalten. Jedoch wurde eine Tendenz der MoCo eine leichte Glättung der Bilder zu erzeugen festgestellt. Beide Artefaktkorrekturen haben Kapazitäten gezeigt, die Bildqualität deutlich zu verbessern.

Contents

List of Acronyms

Notation	Description
1D	1-dimensional
2D	2-dimensional
3D	3-dimensional
AV	Aortic valve
CBCT	Cone-beam CT
CT	Computed tomography
CTA	Computed tomography angiography
CTDI	Computed tomography dose index
DSCT	Dual-source computed tomography
ECG	Electrocardiogram
FBP	Filtered backprojection
FOV	Field of view
ICRP	International commission on radiological protection
MAM	Motion artifact metric
MoCo	Motion compensation
MPR	Multiplanar reconstruction
MSCT	Multi-slice computed tomography
MVF	Motion vector field
PAR	Partial angle reconstruction
RCA	Right coronary artery
RMSE	Root mean square error
ROI	Region of interest
STAR	Stack transition artifact removal
WFBP	Weighted filtered backprojection

List of Figures

List of Tables

1 Introduction

This work deals with cardiac computed tomography (CT) and the software-based compensation of motion encountered during the CT scan. CT imaging of the heart has come to be applied in many clinical tasks, such as the examination of the coronary arteries, checks for stenosis, checks for calcification or pre-interventional planning (e.g. for cardiac valve replacement), just to name a few [1, 2, 3]. The application, research and development in this field are motivated, to a major degree, by cardiac and cardio-vascular disease being among the top causes of death [3, 1]. The rapid motion of the heart can lead to motion artifacts in the reconstructed CT images, degrading image quality. Figure 1.1 illustrates the cardiac motion and artifacts using CT images including longitudinal cross sections of the heart. Single slice spiral CT was introduced around 1996 into clinical routine and the first multi-slice computed tomography (MSCT) scanners followed in subsequent years. These developments considerably advanced the abilities to image the heart. Numerous hardware-and software-based solutions, for CT in general, and for cardiac CT in particular, have been conceived. Various technical solutions, such as slip ring technology, enabled ever higher gantry rotation speeds for improved temporal resolution. Currently, gantry rotation speeds of around 250 ms are available [4, 5]. The introduction of electrocardiogram (ECG) gating and phase selective reconstructions by Kachelrieß et al. [6] were crucial for cardiac CT as well. Generally, a gated cardiac CT scan can be performed in two ways, either using prospective or retrospective gating. In a retrospectively gated spiral CT scan, the continuous acquisition allows to capture an entire volume at multiple cardiac phases [6, 7, 8, 9]. In order to reduce patient dose, during phases of low interest, the x-ray tube current is reduced. That is referred to as ECG-based tube current modulation [10, 5]. The gating enables data extraction for individual phases. Using prospective gating, sequence scans at different positions aimed at one cardiac phase can be performed. Such a sequence scan, also known as step-and-shoot, can be utilized for multiple cardiac imaging tasks. Prospectively gated scans can generally be associated with a low dose [11, 12, 13, 14]. In case of high heart rates (e.g. > 60 bpm) and arrhythmic cardiac motion (e.g. due to cardiac arrhythmia) retrospectively gated scans may still be recommended [14]. MSCT scanners enable the capture of larger volumes at once, i.e. in one (half) resolution of the gantry. If the heart cannot be imaged at once, data may have to be acquired or extracted in multiple steps, with each step corresponding to different times, but ideally to the same heart phase. The cardiac reconstructions can then yield

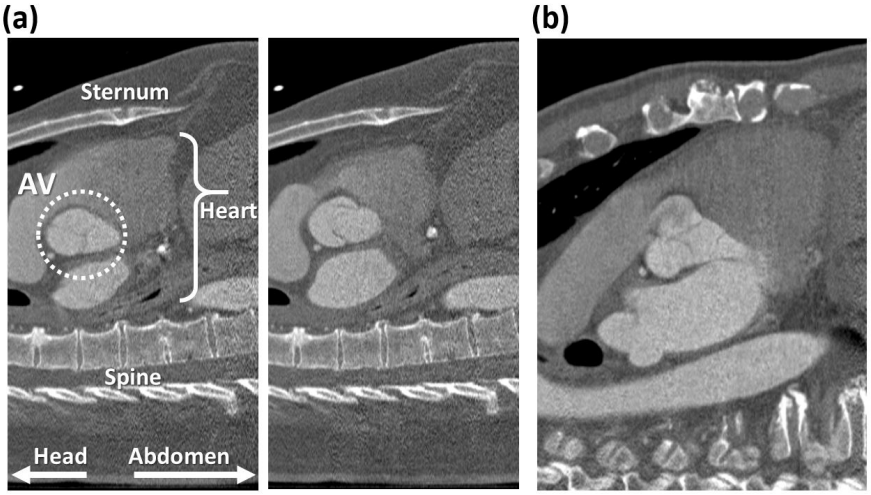

Figure 1.1: **(a)** Two sagittal (side view) cardiac CT images from one patient at two times during the cardiac cycle. The heart can be observed in different states of contraction and the aortic valve (AV) in its open and closed state. **(b)** Sagittal cardiac CT image with motion artifacts at the AV.

sub-volumes, or stacks, that share these characteristic and that cover longitudinal parts of the volume. They need to be combined to acquire a complete CT volume. Another solution well suited for cardiac CT is the use of dual-source computed tomography (DSCT) scanners. The second x-ray source and detector array reduce the necessary scan angle coverage from 180° to 90° and therefore improve the temporal resolution by a factor of about two, compared to the use of a single source CT [5]. The temporal resolution may be improved via software solutions as well. For example, iterative reconstructions that use smaller scan angle coverages compared to the 180° (+ fan angle) required by analytical methods, were proposed but have not found their way into the clinical routine [15, 16, 17]. Another software-based solution to improve cardiac image quality is motion compensation (MoCo). A common approach is to use spatially redundant information from multiple cardiac phases to estimate cardiac motion [18, 19, 20, 21, 22, 23]. There are also approaches that do not require multiple cardiac phases. The available data are split into sections that are reconstructed into so-called partial angle reconstructions (PARs). Image registration can be used to match PARs that are "separated" by 180° of projections to estimate a motion vector field (MVF)[24]. Furthermore, the lack of additional information from multiple phases can be overcome by optimizing motion artifact metrics (MAMs) that penalize the presence of motion artifacts [25, 26, 24]. Machine learning was applied to motion estimation as well. The networks were trained to estimate motion in image domain based on simulated data [27, 28, 29, 30]. The occurrence of motion artifacts depends on many factors and studies including the impact of motion artifacts are often task specific [31, 32, 33, 34]. Artifacts may reduce image quality to a point, that renders them non diagnostic. Furthermore, in case of size measurements, e.g. for valve replacement surgery, precision is key and

may easily be impeded by motion artifacts [1]. Another, specific type of motion artifact can appear when the CT volume has to be assembled from multiple stacks and the latter do not represent exactly the same volume. For example, because of breathing motion or cardiac arrhythmia. The resulting discontinuities between the stacks and in the final CT volume have, among other, been referred to as streak, banding or stack transition artifacts. These issues have been addressed in the past [35, 36, 37]. However, severe artifacts, e.g. due to cardiac arrhythmia still posed a problem [37]. Said artifacts can arguably be considered as a type of motion artifact, however, they will hereafter be referred to as stack transition artifacts and should not be confused with the motion artifacts in reconstructions from individual (short-scan) data segments.
This work focuses, on one hand, on the development of a stack transition artifact removal (STAR) method, and on the other hand on the development of a motion compensation algorithm for the aortic valve (AV) using short-scan data. The latter method will hereafter be referred to as the valve MoCo.

2 Fundamentals

2.1 X-ray Radiation

Wilhelm Conrad Röntgen made his Nobel Prize-winning discovery in the year 1895 [38]. It became invaluable for modern medicine due to the combination of x-ray radiation characteristics regarding penetration of and interaction with matter, as well as the relative ease with which it can be generated (in the diagnostic range). The relevant energy range for CT is 50 keV to 140 keV [38]. In clinical applications, energies beyond that are typically only found in radiation therapy, where radiation with energies of up to 25 MeV are used [39].

2.1.1 X-ray Interaction with Matter

X-ray attenuation happens through multiple processes involving absorption and scattering of photons. The overall attenuation in matter can be represented by the linear attenuation coefficient μ. The Beer-Lambert law postulates an exponential drop of radiation intensity with penetration depth:

$$I = I_0 e^{-\mu d}. \tag{2.1}$$

Here, I_0 is the initial intensity and I the intensity after passage trough the depth d within the attenuating object. (2.1) is only valid for monochromatic electromagnetic radiation and a homogeneous attenuating object with a total attenuation coefficient μ. A multi-energy Beer-Lambert law for heterogeneous objects ($\mu = \mu(\boldsymbol{r}, E)$) can be written as

$$I(E) = I_0(E) e^{-\int_L \mu(\boldsymbol{r},E)\boldsymbol{dr}}. \tag{2.2}$$

Here, E is the radiation energy, L the x-ray path and $\boldsymbol{r}$ denotes a position in the attenuator. The linear attenuation can also be normalized by the material density ρ yielding the mass attenuation coefficient $\frac{\mu}{\rho}$.
The linear attenuation coefficient can be computed as $\mu = n\sigma$ using the particle density n and the cross section σ for attenuating processes. The computation may be performed with the total, as well as with crossections for individual interaction processes.
For mixtures, as well as chemical compounds, the linear attenuation coefficient can be approximated by a weighted sum of the individual coefficients. The weights are the

(a) Water

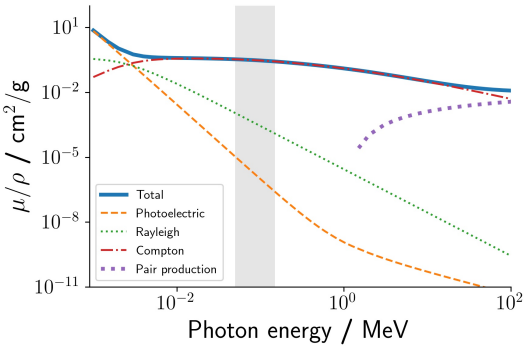

(b) Iodine

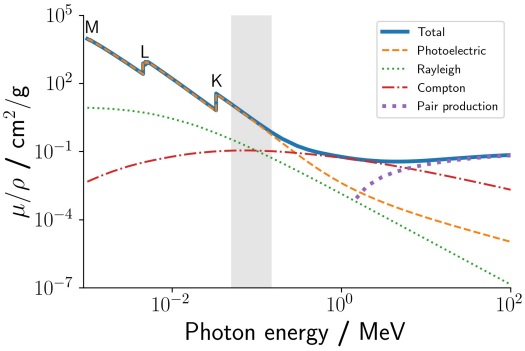

(c) Gadolinium oxysulfide

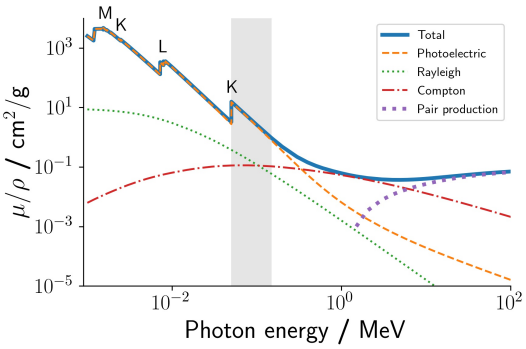

(d) Organic and anorganic materials

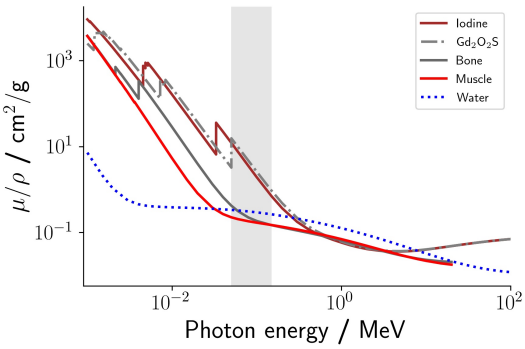

Figure 2.1: (a)–(c) Linear mass attenuation coefficients (total, photoelectric effect, Rayleigh scattering, Compton effect and pair production) for various materials. (d) Comparison between organic and anorganic materials. The K, L and M edge locations are marked. The grey areas mark the CT-relevant 50 keV to 150 keV range. Source of data: [42]

normalized mass fractions. For example, the mass attenuation coefficient for water can be expressed as [40, 41]

$$\left(\frac{\mu}{\rho}\right)_{H_2O} = \frac{1}{9}\left(\frac{\mu}{\rho}\right)_{H} + \frac{8}{9}\left(\frac{\mu}{\rho}\right)_{O}.$$

The major attenuation processes, through which photons interact with matter include the photoelectric effect, the Compton effect, Rayleigh scattering and pair production. Figure 2.1 displays the mass attenuation coefficients for water, iodine (commonly used in contrast agents) and gadolinium oxysulfide (scintillator material commonly used in detectors), as well as bone and muscle.

Photoelectric effect

The photoelectric effect is the absorption of a photon by an atomic electron with the latter being emitted as a free electron. Therefore, the photon energy $E_\gamma = h\vartheta$ (h: Planck constant; ϑ: radiation frequency) needs to exceed the binding energy E_B of the electron. The emitted electron will have a kinetic energy $E_\mathrm{e} = E_\gamma - E_\mathrm{B}$ [38, 40]. The linear attenuation coefficient μ_P for this process is strongly dependent on the atomic number Z and the photon energy. For diagnostic energy ranges, it can be found empirically that [38, 41]

$$\mu_\mathrm{P} \propto \frac{Z^4}{E_\gamma^3}.$$

The Z^4 dependence is particularly relevant for the selection of radiation-shielding materials (e.g. Pb; Z=82) or x-ray contrast agents (e.g. I; $Z = 53$) [38].
A precise computation of the cross section requires a quantum mechanical approach. The wave functions of the photon and the electron in its bound and continuum state, as well as the potential of the nucleus have to be computed. Different approximations can be made for different atomic numbers and photon energies. A non-relativistic approximation for K-shell interaction is [43]

$$\sigma_\mathrm{K} = \frac{4\sqrt{2}Z^5\alpha^4}{E_\gamma^{7/2}}\phi_o \left(2\pi \left(\frac{\epsilon_\mathrm{K}}{E_\gamma}\right)^{1/2} \frac{\exp(-4n_1 \cot^{-1}(n_1)}{1-\exp(-2\pi n_1)}\right),$$

where $\phi_0 = \frac{8}{3}\pi\alpha^2$ is the Thomson cross section, α is the fine structure constant, ϵ_K is the K-shell binding energy and $n_1 = (\epsilon_\mathrm{K}/(E_\gamma - \epsilon_\mathrm{K}))^{1/2}$. Generally, factors including energy range, atomic number, relativistic effects and spin -or polarization states can have a considerable impact [43]. The edges in the cross section/attenuation profile where new atomic shells become available to the photoelectric effect with increasing photon energy display fine structure (except the K-edge). It originates from the presence of multiple electron energy states due to angular-momentum coupling, e.g. L-S coupling for light and j-j coupling for heavy atoms. For photon energies beyond ϵ_K, the photoelectric effect at K–shell electrons will make up more than 80% of all photoelectric events [38].

Compton effect

The Compton effect is the process of inelastic scattering of a photon on an atomic electron. The latter is emitted from the atom. After taking energy and momentum conservation into account, the energy of the outgoing photon can be expressed as a function of the photon scatter angle θ and the initial photon energy E_γ:

$$E_\gamma^{'} = E_\gamma \frac{1}{1+\frac{E_\gamma}{m_0c^2}(1-\cos(\theta))}.$$

The differential cross section can be approximated by the Klein-Nishina formula, that assumes scattering on free electrons [41]:

$$\frac{d\sigma_{\mathrm{KN}}}{d\Omega} = \frac{r_0^2}{2}(1+\cos(\theta)^2)\left(\frac{1}{1+a(1-\cos(\theta))}\right)^2\left(\frac{a^2(1-\cos(\theta))^2}{1+a(1-\cos(\theta))(1+\cos(\theta)^2)}\right)^2,$$

where r_0 is the classical electron radius and $a = E_\gamma/m_0c^2$. Integration yields the total cross section [38, 41]

$$\sigma_{\mathrm{KN}} = 2\pi r_0^2\left(\frac{1+a}{a^2}\left(\frac{2(1+a)}{1+2a} - \frac{\ln(1+2a)}{a}\right) + \frac{\ln(1+2a)}{2a} - \frac{1+3a}{(1+2a)^2}\right).$$

The bound state of the electrons can be accounted for in the differential cross section by introducing the incoherent scattering function $S(k, Z)$ with the transferred momentum k:

$$\frac{d\sigma_C}{d\Omega} = \frac{d\sigma_{\mathrm{KN}}}{d\Omega}S(k, Z).$$

Numerical integration yields

$$\sigma_C \propto Z\sigma_{\mathrm{KN}}$$

for the corrected Compton cross section [41]. The chance of scattering at high angles, where the largest impulse transition happens for backscattering ($\theta = 180°$), is of high importance for radiation protection and dose calculations. As can bee seen in figure 2.1, Compton scattering is the dominant attenuation process for water in the diagnostic energy range.

Rayleigh scattering

The elastic scattering of a photon on an electron is referred to as Rayleigh scattering. The photon energy is conserved and only its direction changes. The differential cross section can be estimated as

$$\frac{d\sigma}{d\Omega} = \frac{r_0^2}{2}(1+cos(\theta)^2)|F(k,\theta)|^2.$$

This approach includes the Thomson differential crossection for elastic scattering that is corrected by the form factor F to account for the bound state of the electrons. θ is the scattering angle and k is the transferred momentum. The form factor is the Fourier-transformed charge distribution [44] but can also be measured for different materials [45].

Pair production

In pair production, a photon is converted into an electron–positron pair within the electric field of a nucleus. The photon energy must exceed two rest masses of an electron, $2m_0c^2 = 1022$ keV, and is therefore beyond the diagnostic range. The presence of the nucleus is required to maintain momentum conservation and the atomic number does have an impact on the cross section. It can be found to be approximately $\propto Z^2$ [41, 40].

2.1.2 X-ray Generation

X-ray tubes are a common source for diagnostic x-rays. They are required to deliver increasing amounts of power in ever shorter times [4]. The main components of an x-ray tube are the cathode and anode placed in a vacuum. Figure 2.2 illustrates the basic setup of a reflection x-ray tube. A current is passing through and heating the cathode to high temperatures ($\approx$ 2400 K), releasing electrons through a series of processes [38]. The emitted electrons are accelerated by a voltage U_a applied between cathode and anode. The tube voltage affects the energy range of the emitted spectrum, while the tube current affects the radiation intensity. In CT, acceleration voltages and tube currents are chosen mostly between 80 kV and 140 kV and between 100 mA and 1000 mA, respectively. The electron beam is focused by electron optics on a small area on the anode [38]. Diagnostic x-ray tubes are generally capable of producing focal spot sizes of 0.1 mm to 2 mm [46]. Radiation is (mostly) emited from the area of the focal spot and smaller focal spots improve the spatial resolution. Some tube designs enable to rapidly switch the focal spot position, which is referred to as a flying focal spot [47]. The anode is generally made of high-Z materials like tungsten [46]. Fast electrons are decelerated in the anode turning most of their energy into heat and converting a small part ($\approx$ 1 %) to x-rays [38]. The decelerated electrons emit a continuous x-ray spectrum, the Bremsstrahlung. The latter is superimposed by a characteristic spectrum originating from atomic electron transitions. Usually, multiple photons are generated from one electron in a chain of inelastic scattering events [38]. The incoming electron energy is $E_\mathrm{e} = e \cdot U_\mathrm{a}$ with e being the elementary charge. The upper energy limit for emitted x-rays is therefore

$$E_\mathrm{max} = E_e = e \cdot U_\mathrm{a}. \tag{2.3}$$

The intensity of the Bremsstrahlung in an energy range $[E, E + dE]$ can be expressed as

$$I(E)\,dE = \frac{1}{m_\mathrm{a}} \int_E^{E_e} d\sigma_\mathrm{rad} \left(\frac{1}{\rho} \frac{dE_e}{dx} \right)^{-1} dE_e$$

with the target density ρ and the target atomic mass m_a [48]. For the differential crossection for photon emission $d\sigma_\mathrm{rad}$ it can be found that

$$d\sigma_\mathrm{rad} \propto \frac{Z^2}{E_e} \frac{dE}{E}.$$

The term $\frac{1}{\rho}\frac{dE_e}{dx}$ is the mass stopping power of the target and can be measured experimentally. The emitted photons also experience attenuation within the anode before exiting it, mostly in the lower energy range.
The characteristic part of the spectrum originates from atomic shell transitions after ionization of atoms. For example, the binding energy of the tungsten K-shell is approximately 69.5 keV [49]. All transition peaks will consequently be found at lower or equal energies. Tungsten x-ray spectra simulated using a semi-empirical model [48]

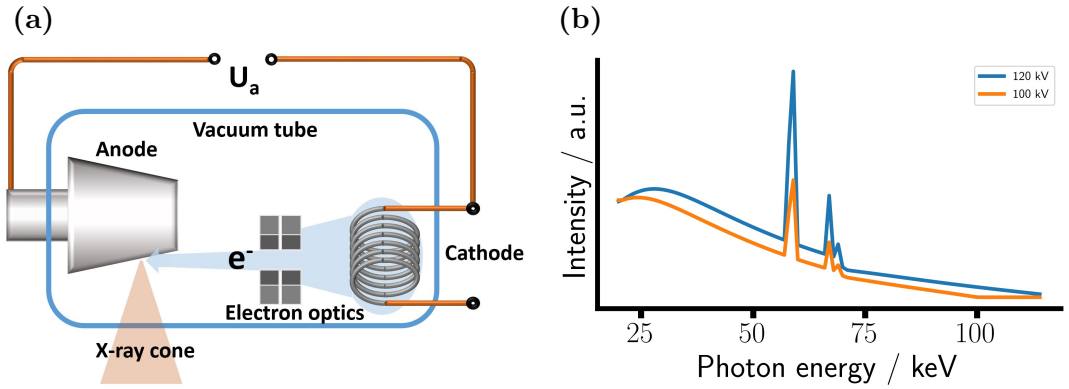

Figure 2.2: **(a)** Schematic of a reflection x-ray tube. **(b)** Tungsten target x-ray spectra simulated using a semi empirical method [48]. Tube potentials of 100 kV and 120 kV were simulated.

are displayed in figure 2.2. The temperature load on the anode is considerable and thermal conductivity and the melting point are important factors to take into account. To enable higher tube output, larger anodes with larger heat capacities were designed. Furthermore, tube designs that include direct cooling via a cooling medium, as well as rotating anodes that distribute the thermal load over larger parts of the anode were developed [4, 47, 38].

2.1.3 X-ray Detection

Indirect conversion detectors

Current CT scanners generally use indirect conversion detectors. The main elements are an anorganic scintillator layer coupled to a photodiode. X-ray photons enter the scintillator and interact with a high probability ($\approx 90\%$), setting off a chain of processes that ultimately result in the emission of optical photons. Figure 2.3 illustrates an indirect conversion detector. The interaction occurs via the photoelectric effect and Compton scattering, creating electron-hole pairs that populate the valence and conduction energy bands of the scintillator. The electron-hole pairs migrate through the material and can recombine at luminescence centers (impurities in the the scintillator crystal purposely introduced through activator materials) under emission of an optical photon [50, 47]. Undesired effects include non-radiative recombination before and reabsorption after photoemission. The luminescence is registered by the photodiodes. An example for a scintillator material used in CT is gadolinium oxysulfide (Gd_2O_2S) [47]. Photons emitted away from the diodes are reflected back from a layer on top and on the sides of the detector pixel. The photo signal is subsequently amplified and converted to a digital signal. The signal pulse width from one registered photon is roughly 2500 ns (for Gd_2O_2S), preventing individual photons to be distinguished [47]. Signals from individual photons are added up, which relates to the term energy integrating detector. Multiple corrections have to be applied to the raw signal before it can be used for image reconstruction, such as the correction for the dark current, the afterglow, non-linearity or geometric corrections [38, 47].

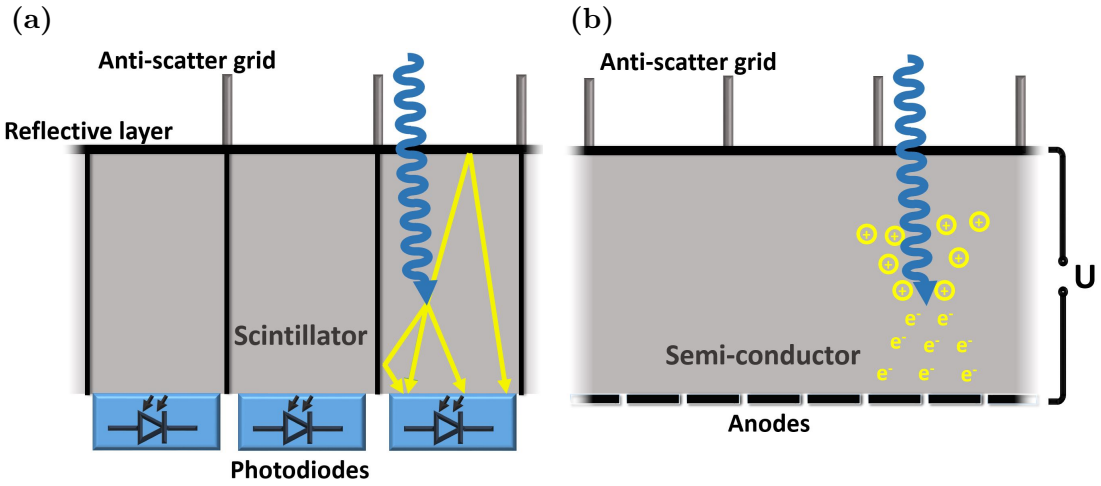

Figure 2.3: **(a)** Illustration of an indirect conversion detector. **(b)** Illustration of a direct conversion detector.

In a CT scanner, detector elements are arranged in rows of hundreds (for axial field of view (FOV)) and slices of tens (up to 320) [51]. Detector pixel sizes are generally in the range of 0.5 mm to 0.6 mm [5]. Single detector elements are optically separated to

minimize cross-talk between the pixels [47]. The detector arrays are also equipped with an anti scatter grid. Without it, scattered radiation would significantly degrade the image quality. The quotient between radio sensitive and total detector area is referred to as geometric efficiency. It must be considered in addition to the quantum efficiency of the scintillator for an imaging system. The separating layer between the detector elements and the anti-scatter grid are limiting factors for the geometric efficiency.

Direct conversion detectors

Direct conversion detectors revealed a lot of potential in CT prototypes in recent years [5, 47]. Instead of scintillators, semiconductors are used, in which incident photons create a charged cloud that is caught through an applied voltage. The resulting signal is very short (≈ 25 ns) enabling individual photons to be counted. In addition, the created charge is proportional to the incident energy. As a consequence, this type of detector is able to differentiate between energies in addition to being photon counting [47]. A typically used semiconductor is cadmium tellurite (CdTe) [52]. Solid semiconductor crystals are underlined with pixelated anodes [53]. No separation layers between detector pixels are required like for indirect conversion detectors, enabling smaller detector pixel sizes. Reconstructing smaller image pixels will result in higher noise, unless dose is increased. Alternatively, iterative reconstruction or processing methods can be used. Furthermore, it has been shown that using smaller detector pixels, while maintaining reconstructed image resolution, still benefits image noise [54, 52]. Considerable issues include the management of exposure to not exceed the count rate limits and pile up effects resulting in the underestimation of photon numbers (and overestimation of photon energy). Photon counting detectors have not been implemented in the clinical routine as of yet and research is ongoing [47, 5].

2.2 Dose

A basic physical dose quantity is the absorbed dose D. It is defined as the locally absorbed radiation energy per unit mass and has the unit Gray ($1\,\mathrm{Gy} = 1\,\mathrm{J/kg}$) [55, 56].

$$D = \frac{dE}{dm}$$

It can be estimated using phantom measurements, Monte Carlo simulations and other analytical or numerical approaches [57, 58, 59, 60, 61, 62, 63, 64]. In CT, the computed tomography dose index (CTDI) is a standard measure for the radiation output of a CT system and is used to compute other dose quantities [10, 51]. It is defined as the integral of the absorbed dose in one CT slice over the entire rotational axis of the CT scanner. In order to measure the CTDI, standardized phantoms in different sizes (representing the head or torso) are used. In order to measure primary and scattered/secondary radiation, a 100 mm long, pencil-shaped ionization chamber is typically used. As the dose varies depending on the position in the phantom, another CTDI quantity has been defined, that weights the dose in the center and the outer parts of the phantom

Organ/Tissue	w_T
Lung, stomach, colon, bone marrow, breast, remainder*	0.12
Gonads	0.08
Thyroid, oesophagus, bladder, liver	0.04
Bone surface, skin, brain, salivary glands	0.01

Radiation type	w_R
Photons	1
Electrons, muons	1
Protons, charged Pions	2
α–particles, fission fragments, heavy ions	20
Neutrons	$w(E)$

Table 2.1: Organ-specific weights w_T and radiation-specific weights w_R for the computation of the equivalent and effective doses as recommended by the ICRP [56]. w_T: The remainder tissues are adrenals, extrathoracic tissue, gall blader, heart, prostate, small intestine, spleen, thymus and uterus. w_R: The value for neutrons is an energy-dependent function $w(E)$ that peaks at roughly $E = 1$ MeV with w_{Neutrons}=21.

[55, 65, 51]. For spiral CT, the volume CTDI is computed via further division by the pitch. To account for the entire irradiated region (along the rotational axis of the CT scanner), the dose length product can be computed by integrating the CTDI along said axis. Another scan characteristic value is the tube current-time product that can be normalized by the pitch to gain the effective tube current-time product (eff. mAs) [9]. These measures quantify the radiation output, but are not enough to estimate actual biological risks [64]. To estimate the risks, specific dose quantities are used. These are generally given in units of Sievert ($1\,\text{Sv} = 1\,\text{J/kg}$). For a tissue or organ denoted T, the equivalent dose H_T is the sum over the absorbed doses for all encountered radiation types R (x–ray, α, β, etc.), each weighted by the respective factor w_R.

$$H_T = \sum_R w_R D_{T,R}$$

The weighting factor for photons is one for all energies. From it, the effective dose D_{eff} is computed as the sum over all organ doses, each multiplied by an organ specific weighting factor w_T [66, 10].

$$D_{\text{eff}} = \sum_T w_T H_T = \sum_T w_T \sum_R w_R D_{T,R}$$

The radiation and organ-specific factors, as recommended by the International commission on radiological protection (ICRP) [56], can be found in table 2.1. The effective dose is a standard radiological protection quantity and has been adopted by many legislations [10, 56]. In order to estimate the effective dose for cardiac CT scans, the dose length product can be multiplied by a conversion factor. However, this approach has been found to underestimate the dose and more sophisticated methods including

measurements on anthropomorphic phantoms and Monte Carlo simulations have been proposed [10, 67, 68].
The total mean annual dose in Germany amounts to 2.1 mSv from natural sources and 1.7 mSv originating from human-made sources [69]. The dose can vary considerably for one type of cardiac CT examination, depending on the varying scan protocols and hardware used on different sites [70, 71, 72, 73, 74, 75]. Effective doses from CT examinations of the head, chest and abdomen stated in recent studies include values in the range of 2 to 3 mSv, 6 to 13 mSv and 5 to 10 mSv, respectively [70, 72]. For retrospectively and prospectively gated cardiac CT, reported mean effective doses included 5 mSv [74] and 1 to 4 mSv [75, 71, 74], respectively. These values are subject to change in the future, as there is a strong incentive to reduce patient dose. In the last ten years, individual measures such as the installation of new scanners or optimized scanning protocols have resulted in considerable reductions of patient doses, with improvements of up to 50% per measure taken [76, 77, 78]. With ultra low dose CT protocols, doses in the sub mSv range have been achieved. For ultra low dose chest CT, reported values include 0.1 mSv to 0.4 mSv, reducing dose by a factor of roughly ten compared to standard dose CT protocols used in the studies [79, 80, 81, 82, 83, 84]. Other applications included limb fracture imaging (0.03 mSv) [85] or head imaging (0.62 mSv) [86]. In addition, ultra low dose protocolls were applied to coronary computed tomography angiography (CTA) with reported doses of 0.3 mSv to 0.5 mSv [87, 88, 89], however it has also been demonstrated that values<0.1 mSv are possible [90].

2.3 CT Setup and CT scan

A clinical CT scanner acquires x-ray projections using an x-ray tube and a detector array that rotate around the imaged patient. Modern MSCT scanners simultaneously acquire multiple x-ray projection slices (up to 320) along the longitudinal axis/patients long axis [5]. Figure 2.4 displays a MSCT setup, with the z-axis/longitudinal axis parallel to the patient. The x- and y-axes span the axial plane, the x- and z-axes the coronal plane and the y- and z-axes the sagittal plane. The (collimated) x-ray cone is characterized by the fan-angle Φ in the axial plane and by the cone angle Γ longitudinally. Some CT scanners have two tube–detector pairs (DSCT). The number of simultaneously acquired slices and the slice thickness determine the CT scanners collimation and therefore, the volume that can be covered in one rotation. The detector array is generally curved around the x-ray source, unless it is a flat panel detector in a cone-beam CT (CBCT) system. The FOV of modern CT scanners is often 50 cm, with the second tube-detector pair in DSCT systems having a smaller FOV [5]. The collimations vary between vendors and models. They are in the range of 38 mm to 160 mm for most devices [5]. Some scanners utilize a flying focal spot in z-direction to double the amount of acquired slices, while the collimation remains unchanged. The rotation time of the gantry determines the temporal resolution, as conventional image reconstructions require at least 180° (+Φ) of coverage. Rotation times of down to 0.25 seconds have been achieved [5]. DSCT systems reduce the necessary angular coverage from 180° to 90° improving the temporal resolution by a factor of two. Table 2.2 shows

different CT-scanners with some of their specifications. Given a circular scan, the detector slices acquire data, sampling the scanned volume. The slice sensitivity profile can be used to describe the resolution in z-direction. It is defined as the reconstruction of a delta object and may be approximated with a rectangle function for a circular scan [38, 6]. Spiral/helical CT can be used to acquire large volumes beyond the scanners collimation. Therein, the x-ray source travels on a spiral trajectory around the patient. The forward motion is described by the pitch $p = d/C$, where d is the patient table shift per rotation and C is the collimation. Figure 2.4 illustrates trajectories and detector coverage at different pitch values. For $p = 1$ each region is irradiated once. Smaller values result in regions being irradiated more than once. To offset the resulting dose increase, the tube current-time product can be adjusted (automatically). Maintaining a constant effective mAs value results in constant dose [91]. Typical pitch values are in the range 1–1.5 [38]. Exceptions are found in specific cardiac CT applications, where the beating heart is scanned with $p < 1$ to enable data acquisition for a range of its states/phases. The pitch can also be related to the rotation time and the heart rate, in order to cover all regions sufficiently [6, 7]. In order to express the slice sensitivity profile, the contribution of each slice to the reconstruction of the delta object, which may be a function of not just space but also time/phase (e.g. cardiac gating), should be considered [7]. In 3-dimensional (3D) spiral CT reconstruction, the slice position(s) can be chosen arbitrarily, as data for a slice may be interpolated from the continuously acquired spiral data set. Interpolation neighbors for one projection angle are spaced 180° apart. Making use of the direction invariance of x-ray projections, a second spiral can be rebinned enabling 180° interpolation [38]. Multiple projection slices, that were not necessarily all acquired simultaneously, can contribute to one reconstructed slice. Weighting/filtering in z-direction relying on the slices distance from the reconstruction plane can be used. A z-filter that yields the interpolation of two neighboring slices achieves the optimal z-resolution, which is the detector slice thickness [7, 9].
The CT scan acquires the raw projection data. The data are corrected to account for various issues related to the detector and logarithmized. The final projection data that are used in subsequent reconstructions corresponds to the line integral over the linear attenuation coefficient $\int_L \mu(\boldsymbol{r}, E)\boldsymbol{dr}$ in (2.2) (see sec. 2.1). However, in CT reconstruction the x-ray spectrum is usually assumed to be monochromatic and the energy dependence in (2.2) is not considered.

(a) MSCT setup (b) Spiral MSCT

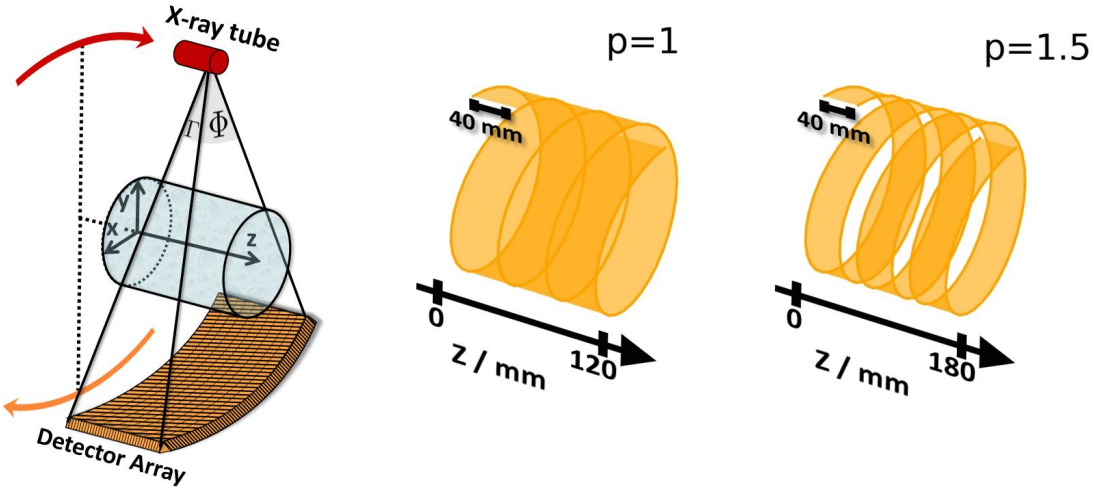

Figure 2.4: **(a)** MSCT setup. **(b)** Illustration of detector coverage for pitch values $p = 1;\ 1.5$; for a collimation of 40 mm and three rotations. Not to scale.

Vendor	Model	#Slices × depth	FOV	collimation	rot. time	
Canon	Aquilion One Genesis	320×0.5 mm	50 cm	160 mm	0.275 s	
Canon	Aquilion Precision	160×0.25 mm	50 cm	40 mm	0.35 s	
GE	Revolution Apex	256×0.625	50 cm	160 mm	0.28 s	
GE	CardioGraph	192×0.73 mm	25/15 cm	140 mm	0.24 s	
Philips	Brilliance iCT	2·128×0.625 mm	50 cm	80 mm	0.27 s	ffs
Phillips	IQon	2·64×0.625 mm	50 cm	40 mm	0.27 s	ffs
Siemens	Somatom Edge Plus	2·64×0.6 mm	50 cm	38.4 mm	0.28 s	ffs
Siemens	Somatom Force	2·96×0.6 mm	50/35 cm	57.6 mm	0.25 s	DSCT ffs

Table 2.2: Modern CT scanner specifications [5]: Vendor and model name; number of (longitudinal) slices and slice depth; collimation; rotation time. DSCT and flying focal spot (ffs) are marked for the respective systems. With ffs, the number of slices is doubled.

2.4 Analytic Image Reconstruction

Parallel Geometry

Parallel-beam geometry is the simplest approach to CT reconstruction. While it has not been used in CT hardware in a long time, the common fan-beam geometry can be rebinned to parallel geometry for reconstruction. The geometry and the parameters are illustrated in figure 2.5. Generally, the raw/projection data are expressed in projection space. The latter is spanned by the coordinates (ξ, ϑ) in 2-dimensional (2D) space. A point in projection space states the line integral of an x-ray at an angle ϑ originating from a source at a distance ξ from the central ray passing the isocenter of the gantry. In an actual scanner, the detector slices add the third z-coordinate. However, here, individual slices (perpendicular to the z-axis) are regarded. Filtered backprojection (FBP) is an analytical image reconstruction commonly used in CT. The raw data are filtered and transformed to image space. Individual projections will be summed up in image space to form the final CT image. The following section is a derivation of the FBP formula in 2D. (2.10) is the final result.

The x-ray is described as a straight line:

$$x\cos\vartheta + y\sin\vartheta = \xi. \tag{2.4}$$

The point $\boldsymbol{r} = (x, y)^{\mathrm{T}}$ is expressed in the reference system of the object of interest. The projection $p(\vartheta, \xi)$ resulting from the integral along the x-ray is:

$$p(\vartheta, \xi) = \int d\boldsymbol{r}\ f(\boldsymbol{r})\delta(x\cos\vartheta + y\sin\vartheta - \xi), \tag{2.5}$$

where $f(\boldsymbol{r})$ is the object function describing the spatial distribution of the attenuation coefficients and δ is Dirac's delta function, which sets the integration path in the integral. (2.5) can be simplified using $x\cos\vartheta + y\sin\vartheta = \boldsymbol{r}\cdot\boldsymbol{\vartheta}$ with $\boldsymbol{\vartheta} = (\cos\vartheta, \sin\vartheta)$:

$$p(\vartheta, \xi) = \int d\boldsymbol{r}\ f(\boldsymbol{r})\delta(\boldsymbol{r}\cdot\boldsymbol{\vartheta} - \xi). \tag{2.6}$$

The transform that converts f to p is the x-ray transform X and reconstructing the image means finding the inverse transform X^{-1}. In order to do that, we formulate the Fourier transform $\mathcal{F}(p) = P$ of the projection data p with respect to ξ and the Fourier transform $\mathcal{F}(f) = F$ of the image f in two dimensions. It can then be shown that:

$$F(u_{\mathrm{x}} = u\cos\vartheta, u_{\mathrm{y}} = u\sin\vartheta) = P(\vartheta, u), \tag{2.7}$$

where u_{x} and u_{y} are the coordinates in Fourier space in x- and y-direction, while u and the projection angle ϑ are polar coordinates in Fourier space. (2.7) is known as the Fourier slice theorem [92, 38]. Finally, an inverse Fourier and a coordinate transform, as well as exploiting some symmetry properties of the Fourier transform, yield an expression for the image f:

(a) Parallel-beam geometry

(c) Fan-to-parallel rebinning

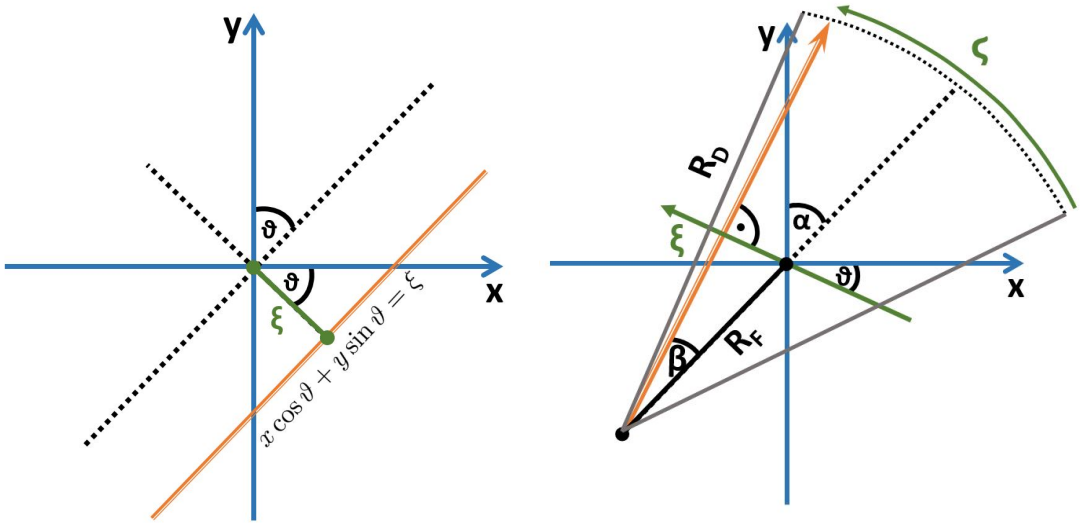

Figure 2.5: Illustration of parallel and fan-beam geometry and fan-to-parallel rebinning.

$$f(\boldsymbol{r}) = \int_0^{\pi} d\vartheta \int_{-\infty}^{\infty} du\ P(\vartheta, u)|u|\ e^{2\pi i u\, \boldsymbol{r}\boldsymbol{\vartheta}}. \tag{2.8}$$

The product $|u|P(\vartheta, u)$ followed by an inverse Fourier transform in (2.8) is a convolution that is realized by a multiplication of the two functions in Fourier domain. The absolute value $|u|$ is known as the ramp kernel. In spatial domain it yields:

$$k(\xi) = \int du\ |u| e^{2\pi i u \xi} = -\frac{1}{2\pi^2 \xi^2}. \tag{2.9}$$

Now, (2.8) can be rewritten as follows:

$$f(\boldsymbol{r}) = \int_0^{\pi} \mathrm{d}\vartheta\ p(\vartheta, \xi) * k(\xi)\Big|_{\xi = \boldsymbol{r}\cdot\boldsymbol{\vartheta}}. \tag{2.10}$$

It now states, that the projection data p have to be convolved or filtered with a reconstruction kernel $k(\xi)$ at first. (2.10) describes the filtered backprojection in parallel beam geometry. The kernel $k(\xi)$ acts as a filter for spatial frequencies and can be chosen to be different than the ramp kernel. For instance, a smoother reconstruction kernel allows for less noise in the image but the spatial resolution is reduced as well. A more detailed derivation of the filtered backprojection for parallel beam geometry can be found in the literature [38, 92].

Fan-to-Parallel Geometry Rebinning

MSCT projection data are generally acquired in fan-beam geometry, or strictly speaking in cone-beam geometry. In this section, 2D fan-beam geometry slices (perpendicular

to the z-axis) are discussed. As indicated in figure 2.5, a ray is now defined by the projection angle α and the fan angle β. $R_\mathrm{F}/R_\mathrm{D}$ are the distances of the x-ray focus to the isocenter/detector and a ray can be assigned a coordinate on the curved detector $\varsigma = \beta\, R_\mathrm{D}$. Fan-beam reconstruction can be achieved by rebinning to parallel geometry and reconstructing afterwards.
Each fan beam ray (α, β) can be expressed in parallel beam coordinates as $(\vartheta = \alpha+\beta, \xi = -\sin(\beta)\, R_\mathrm{F})$. Consequently, it is possible to transform fan beam data into parallel data via rebinning and perform a parallel beam reconstruction [92, 47]. One now seeks to find fan-beams $\hat{p}_\alpha(\beta)$ to populate parallel beam projections $p_\vartheta(\xi)$ with corresponding beams/rays. As illustrated in figure 2.5, a fan beam (α, β) corresponds to a ray from $p_\vartheta(\xi)$ at another angle ϑ. Given the parallel detector coordinate $\xi = \sin(\beta)\, R_\mathrm{F}$ and the angular relation $\vartheta = \alpha + \beta$, corresponding beams can be matched:

$$\hat{p}_\alpha(\beta) = p_{\alpha+\beta}(\sin(\beta)\, R_\mathrm{F}) = p_{\alpha+\beta}(\xi).$$

Given $\beta = \arcsin(\xi/R_\mathrm{F})$ and $\alpha = \vartheta - \beta$, the parallel projections can be populated as

$$p_\vartheta(\xi) = \hat{p}_{\alpha-\beta}(\beta) = \hat{p}_\gamma\left(\arcsin\left(\frac{\xi}{R_\mathrm{F}}\right)\right) \text{ with } \gamma = \vartheta - \arcsin(\xi/R_\mathrm{F}).$$

Note that $p_\vartheta(\xi)$ can only be acquired in accordance to the original fan-beam FOV. A more detailed derivation of fan-to-parallel geometry rebinning can be found in the literature [38].

3D Image Reconstruction

3D CT imaging is commonly achieved using spiral CT and CBCT, with the former being relevant for cardiac CT [93]. As the x-ray source moves on a spiral trajectory, every single projection now corresponds to a different position along the z-axis. The spiral cone-beam data consist of fan-beam projections with different inclinations with respect to the z-axis and can be rebinned to parallel geometry. The weighted filtered backprojection (WFBP) is a commonly used 3D reconstruction method. It is a 3D FBP including a voxel-specific weighting to achieve 180° equivalent reconstructions [47, 94].

2.5 Iterative Image Reconstruction

Iterative approaches have been shown to reduce dose significantly, while providing superior or similar image quality at lower doses compared to analytical reconstructions obtained from normal dose scans. The reported dose reductions are in the range of up to 60% and in some cases higher [95, 96, 97, 98, 99, 100, 101, 102, 103]. The precise characteristics depend on the actual algorithm. Iterative methods may require considerably more computation time compared to analytical methods. Nevertheless, they are gaining importance [5]. Iterative methods have also been used and/or developed specifically for cardiac CT [15, 16, 17, 104].
Unlike analytic reconstruction methods, e.g. FBP, iterative methods seek the image that best agrees with the measured rawdata, while utilizing models for noise and artifact

reduction [102, 105, 17, 4]. A forward model, in other words a simulation of the CT-scan, is often included and may contain varyingly complex models for rays or photon statistics. Prior knowledge about the volume is also used to improve quality [5]. Given the rawdata $\boldsymbol{p}$ and the CT image $\boldsymbol{f}$ one can write

$$\boldsymbol{p} = \mathsf{X}\boldsymbol{f}, \tag{2.11}$$

with the system matrix (incorporating the forward model) X. Due to the size and complicated structure of X in CT, a matrix inversion to solve the system of equations is not an option. Instead, the cost function

$$C = ||\mathsf{X}\boldsymbol{f} - \boldsymbol{p}||_2^2 \tag{2.12}$$

can be minimized to acquire a so called pseudo solution. (2.12) just considers the agreement with the raw data (raw data fidelity). The minimization (optimization) can be performed in many ways and the optimal method may vary depending on the task. Analytical solutions may be available to compute individual optimization steps/updates. Beyond that, optimization methods such as the gradient descent can be used. The latter computes the derivative of the cost function to acquire a search direction in solution space, along which the minimal cost function value can be found. More sophisticated methods, such as conjugate gradient methods, seek to optimize the successive search directions to accelerate the optimization. Modern iterative reconstructions often optimize more complicated cost functions that include prior knowledge and regularization, requiring other optimization methods. One can define an optimization task for an iterative reconstruction as:

$$\boldsymbol{f}_{\text{final}} = \underset{\boldsymbol{f}}{\operatorname{argmin}}\{L(\boldsymbol{f}) + \alpha R(\boldsymbol{f})\}, \tag{2.13}$$

where the final CT image $\boldsymbol{f}_{\text{final}}$ is acquired by minimizing a cost function that consists of a term L that measures rawdata fidelity and a regularization term R weighted by a parameter α. Naturally, the rawdata fidelity (with L2-norm) in (2.12) can be modified, substituted or extended. In statistical methods, where a log likelihood function is defined, the negative likelihood function has to be minimized to acquire the most probable solution for a given set of rawdata [103]. There are numerous iterative algorithms that have been approved for clinical routine [106, 107, 108, 109].

2.6 Cardiac Computed Tomography

2.6.1 Imaging Relevant Anatomy and Function

In cardiac imaging it is expected to mostly encounter soft tissue, with the potential for the presence of calcifications and soft plaque. Artificially introduced materials include iodine-based contrast agent, e.g. commonly used in CTA, stents, pacemakers or prosthetic heart valves. Most areas of the heart can be the focus of a diagnostic procedure. For example, there is a strong diagnostic focus on the coronary arteries [1].

Another example are the cardiac valves. They include the aortic, pulmonary, mitral and tricuspid valves. The AV has three, opening and closing, leaflets. The base/basal ring/annulus of the AV is generally the narrowest part of the aorta at the AV and is defined as a virtual ring or oval with three anatomical anchor points of the leaflets [110], hereafter referred to as hinge points. The aortic root stretches from the AV anullus to just above the AV (at the sinutubular junction) [111]. The anatomy of the heart is illustrated in figure 2.6. Furthermore, figure 2.7 displays a 3D rendering of a segmented AV with coronary arteries, from a cardiac CT volume. All these features can be imaged with cardiac CT. The motion of the heart poses a big challenge for imaging tasks.

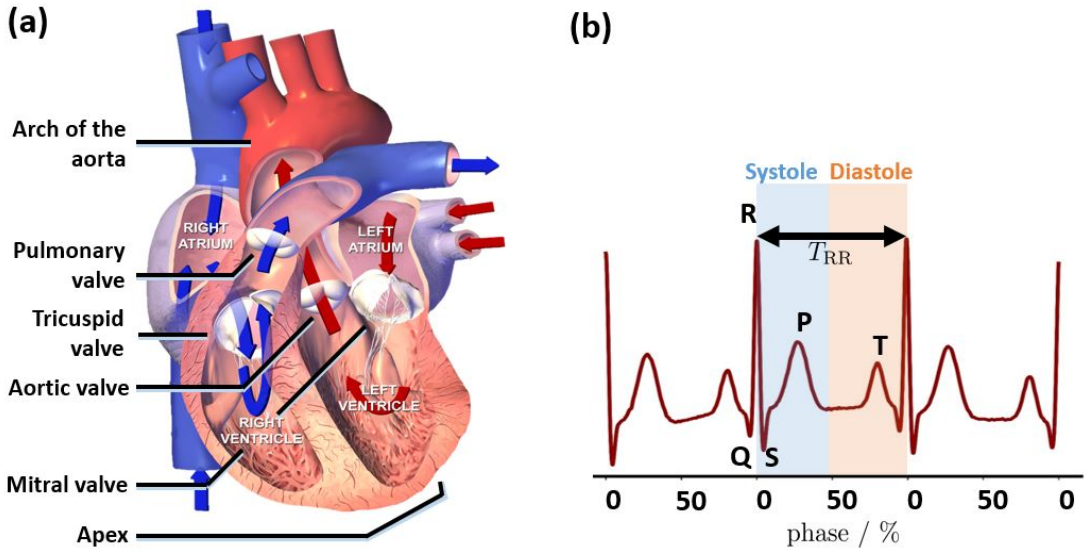

Figure 2.6: **(a)** Sectional anatomy of the heart. Modified image, originally published by Blausen Medical Communications Inc. under the license CC BY 3.0 at `https://commons.wikimedia.org/wiki/File:Blausen_0457_Heart_SectionalAnatomy.png` **(b)** Illustration of an ECG-signal. The peaks, the cardiac period T_{RR} and the coverage of the systole and diastole are marked for one cycle.

The heart rates can vary between 50 bpm and more than 100 bpm [112]. They can be lowered using β-blockers [51, 3]. The heart cycle can be divided, very roughly, in two phases, systole and diastole. During the diastole the ventricles fill, while during the systole they contract pumping blood out into the aorta and the pulmonary artery [113]. The movement during the systole is generally greater [113, 112], but for heart rates greater than 80 bpm matters get more complicated [51]. The motion is correlated with the electric excdata itation of cardiac muscle that can be measured using an ECG. The cardiac phase can be numerically defined using values that are set with respect to the ECG R-peak. This is illustrated in figure 2.6. In CT, it can be used for gating, where acquired data are associated with varying heart phases. Many cardiac CT applications require the use of contrast agent and the respective injection protocols have to be

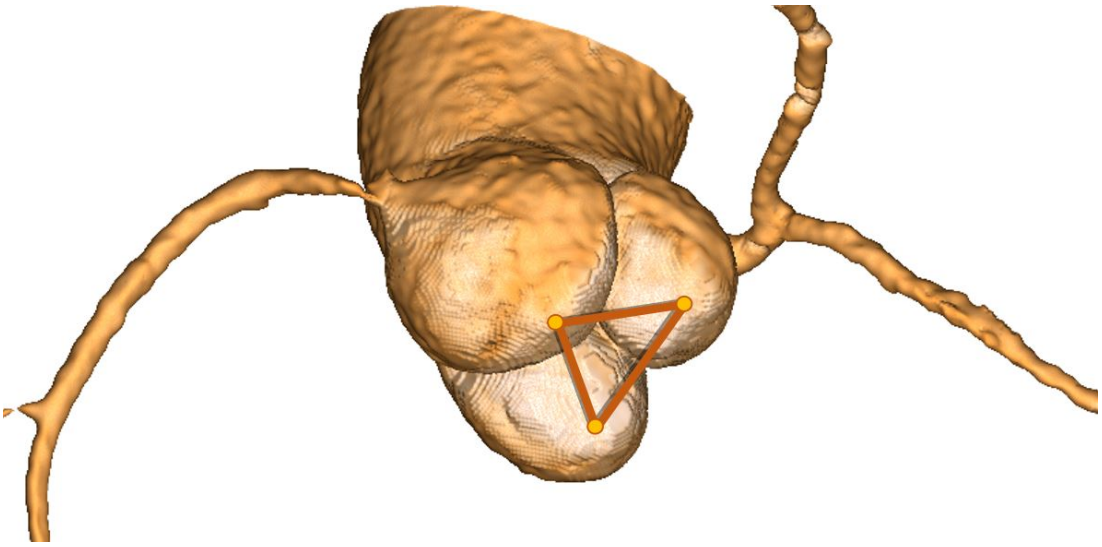

Figure 2.7: 3D rendering of an AV with coronary arteries from a segmented cardiac CT reconstruction. The corners of the triangle mark the locations of the hinge points. The triangle also defines the plane of the AV base (AV plane).

adjusted, depending on where and at what time the contrast agent has to be present (e.g. left or right side of the heart) [1]. The velocities in the myocardium can reach 120 mm/s and sometimes more [114, 115, 116]. The greatest motion has been observed around the apex of the heart [114]. The cardiac motion can be further characterized using cardiac strain. The strain represents the relative deformation, for example of a cardiac wall or a ventricle, with respect to its original length. It can be measured in a beating heart using imaging and typical cardiac strain values vary with region and orientation.

2.6.2 Cardiac Strain

Strain, in the context of cardiac motion, is commonly defined through the relative 1D change of a length, for example the length of the myocardium [117]. Given the fixed initial and final lengths L_0 and L, the strain is

$$\epsilon = \frac{L - L_0}{L_0} = \frac{\Delta L}{L_0}.$$

There are numerous ways to define strain in the heart [117]. Important definitions include the longitudinal, radial and circumferential strain. Longitudinal strain relates to the deformation along the long-axis of the heart, from the base of the heart to the apex. The base of the heart is situated opposite of the apex, towards the head. During the systole, a contraction occurs resulting in $\epsilon < 0$. The radial strain relates to the contraction (diastole) or thickening (systole) of the left ventricular wall. The circumferential strain relates to a rotation of the apex with respect to the base of the

heart. During the systole, this motion results in the reduction of the left ventricle size. During the diastole, as the deformations are reversed, the respective strain values change their sign. Given a 3D MVF $\boldsymbol{d}(\boldsymbol{r})$ at a point in 3D space $\boldsymbol{r}$, the local deformation may be described with the Jacobian

$$\boldsymbol{J} = \left(\frac{\partial \boldsymbol{d}(\boldsymbol{r})_i}{\partial j} \right)_{i,j=x,y,z}.$$

A strain tensor for small deformations ($\Delta L \ll L_0$) can be defined as

$$\epsilon_{ij} = \frac{1}{2} \left(\frac{\partial \boldsymbol{d}(\boldsymbol{r})_i}{\partial j} + \frac{\partial \boldsymbol{d}(\boldsymbol{r})_j}{\partial i} \right)_{i,j=x,y,z},$$

where $\epsilon_{ij}|_{i=j}$ are normal strains and $\epsilon_{ij}|_{i\neq j}$ are sheer strains.
There are numerous methods to estimate cardiac strain. Tissue tracking may be used to determine the change in length within the heart, for example based on the entire myocardium, a ventricle or a wall thickness. The strain may also be computed from derivatives of estimated MVFs [118]. Cardiovascular magnetic resonance (cMR) imaging is a standard for assessing cardiac strain [118]. In addition to tissue tracking, areas in the tissue may be taged by introducing local perturbation of the magnetization and tracked to estimate the motion. The strain may also be directly encoded in an MR image. Echocardiography may be used as well [117, 118]. For example, features may be tracked in 3D or velocities may be measured using tissue Doppler imaging. Strain values vary with location and orientation within the heart. For radial strain, the highest values of up to 40% have been reported, while values for the longitudinal and circumferential strain were roughly 19%. In case of the longitudinal strain, a difference of 4% has been observed between the epicardium and the endocardium (outer and inner layer of the heart wall). Clinically, the cardiac strain can be used to evaluate cardiac function and for prognosis [117, 118, 119].

2.6.3 Clinical Application

Nowadays, cardiac CT has many clinical applications. Heart disease has been identified as the leading cause of death in many countries [3, 1]. The possible goals of cardiac CT examinations are numerous and can be aimed at examining the anatomy/structure or to evaluate cardiac function to either address acute symptoms or to serve a predictive purpose [3, 1]. For example, calcium scoring can yield a predictive value that has been linked to heart disease [3, 1]. It can be performed without the administration of contrast agent. CTA is a common tool to examine the coronary arteries to detect stenoses, coronary calcifications or atherosclerotic plaque. It requires the use of contrast agents and ECG-gating. The latter is generally required whenever phase-selective reconstruction is performed. Other applications include the functional assessment (e.g. in different phases/4D CT) of cardiac valve dysfunction (also for prosthetic valves), vascular anatomy, or the visualization after bypass surgery. CT also plays an important role in pre-interventional planning. For example, before transcatheter aortic (or mitral)

valve implantation, CT is used to asses the valvular anatomy. This includes the measurement of the annulus diameter, the examination of valve leaflets, the examination of the aorta, and requires high (spatial) precision and (motion) artifact-free images. Furthermore, calcifications on the aortic valve and vessel wall can be detected. Other functional assessments include the evaluation of the left or right ventricle function or myocardial perfusion imaging. In the latter, the flow of (contrast agent filled) blood is examined, statically or time-resolved, to find ischemia (lack of blood supply). Delayed enhancement imaging can be used to detect accumulation of contrast agent (5–10 minutes after injection) in tissue affected by necrosis (cell death), fibrosis or scar tissue, or due to vascular obstruction. In case of acute chest pain, cardiac functional imaging can be performed to examine heart wall motion or abnormalities of the ejected fraction (of blood from ventricle volume). [3, 1]

2.6.4 Reading of Cardiac CT Data

Generally, one may want to review features of the heart that do not align with the axial, coronal and sagittal image planes. One application is the examination of the anatomy of cardiac valves, which can benefit from computing multiplanar reconstructions (MPRs) with orientations adjusted to the orientation of an individual valve [110, 120, 121, 122]. MPRs can be described as images that display slices from the (CT) volume that intersect with multiple axial image planes. Given a new image plane, the original volume is resampled on the coordinate system of the former. In order to define the new image plane, anatomical landmarks can be often used. For example, the three hinge points of the AV span a 2D plane at the AV base, that can be used to measure the size of the AV anullus. Said plane will hereafter be referred to as the AV plane. The sagittal and coronal planes can be aligned with the long axis of the aortic root to help find the AV plane, as the latter is approximately orthogonal to said long axis [122]. Figure 2.8 displays MPRs of the AV plane, along with aortic root long-axis aligned image planes. The 4-chamber view can be obtained by adjusting an image plane so that it includes the line connecting the heart apex and the center of the mitral valve. It features both atria and ventricles. Therefrom, a short axis view (short axis of the heart), which is orthogonal to the 4-chamber plane, can be set to, e.g. calculate ventricular volumes and ventricular ejection fractions. Figure 2.9 displays a 4-chamber view and an orthogonal short-axis view, as well as a sagittal slice illustrating the position of the 4-chamber plane. Numerous other possiblities to review cardiac CT data exist [112]. Figure 2.10 displays two further examples. First, a long-axis 3-chamber view that gives an overview over the left atrium and ventricle with the valves. Second, a long-axis 2-chamber view including large portions of the left ventricle and atrium. In order to view coronary arteries in their entirety, curved MPRs that contain a coronary artery can be extracted [123]. Figure 2.14 displays an example with the right coronary artery (RCA).

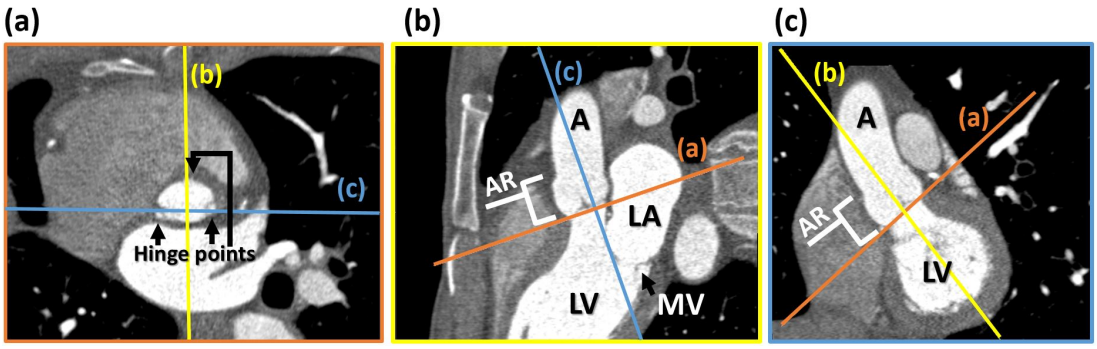

Figure 2.8: Cardiac CT MPRs including the AV. The position of each MPR is marked in the others. The aorta (A), aortic root (AR), left ventricle/atrium (LV/LA), the mitral valve (MV) and the AV hinge points are marked. $C = 200$ HU, $W = 1500$ HU. **(a)** AV plane. **(b)** Tilted sagittal plane aligned with the aortic root. **(c)** Tilted coronal plane aligned with the aortic root.

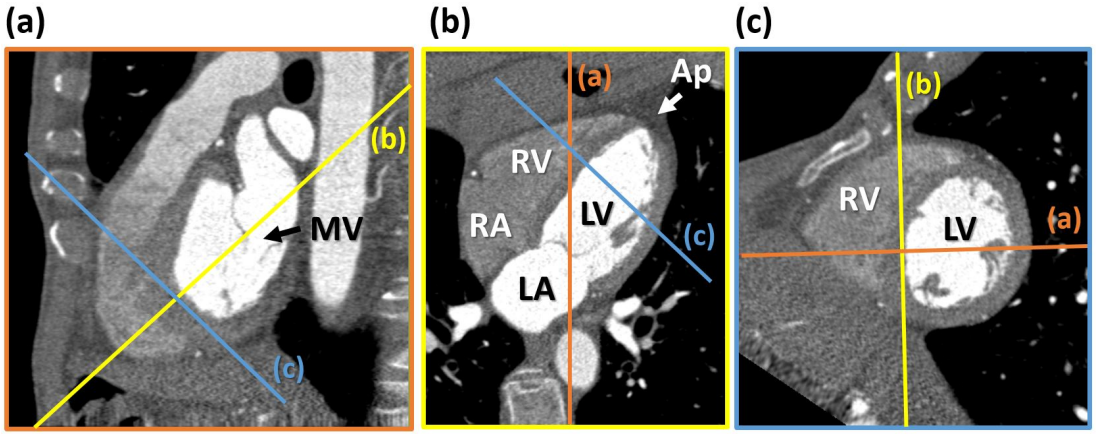

Figure 2.9: Cardiac CT MPRs. The position of each MPR is marked in the others. The mitral valve (MV), the left/right ventricle (LV/RV), the left/right atrium (LA/RA) and the apex (Ap) are marked. $C = 200$ HU, $W = 1500$ HU. **(a)** Sagittal slice. **(b)** 4-chamber view. **(c)** Short-axis view orthogonal to the 4-chamber view.

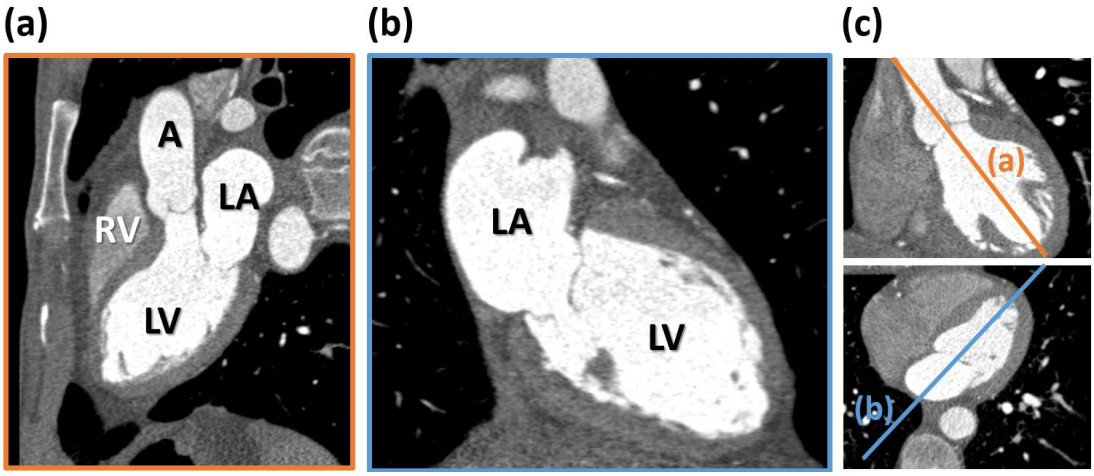

Figure 2.10: Cardiac CT MPRs. The mitral valve (MV), aortic valve (AV), the left atrium/ventricle (LA/LV) are marked. $C = 200$ HU, $W = 1500$ HU. **(a)** Long-axis 3-chamber view. **(b)** Long-axis 2-chamber view. **(c)** Illustration of the positions of (a) and (b) within a coronal slice (top) or an axial slice (bottom).

2.6.5 Imaging Protocols

Retrospectively Gated Cardiac CT

CT scan protocols not specialized for cardiac imaging will yield unsatisfactory results in most cases. Especially when imaging small objects, like the coronary arteries. Reliable imaging of the heart has been enabled by a number of developments [6]. Chief among them are sub second rotation times and submillimeter spatial resolution. During the scan, the patient's ECG is recorded and synchronized with the data. This is referred to as retrospective ECG gating [6]. It is a commonly used technique, for instance in CTA [51, 1]. In theory, with an ECG signal that assigns points in the heart cycle to the data at various time steps, any phase can be reconstructed. To reduce the dose, the x-ray output can be lowered outside the interval where the data are required. This is called ECG-controlled tube current modulation [51, 124].
In order to acquire the heart at multiple phases certain conditions have to be met. An upper limit for the pitch can be defined based on the rotation time t_{rot} and the heart rate $f_{\mathrm{H}} = 1/T_{\mathrm{RR}}$ [6, 7, 91]. The cardiac period T_{RR} is defined as the time interval between two R-peaks in the ECG. Given the requirement that every z-position should be covered by (at least) a detector slice during T_{RR}, the velocity v of the patient table can be limited by $v \leq C/T_{\mathrm{RR}}$, where C is the collimation. At the same time $v = d/t_{\mathrm{rot}}$, with the table shift per rotation d. The pitch $p = d/C$ can therefore be limited by

$$p \leq f_{\mathrm{H}} t_{\mathrm{rot}}. \tag{2.14}$$

For example, given $f_{\mathrm{H}} = 60$ bpm ($T_{\mathrm{RR}} = 1$ s) and $t_{\mathrm{rot}} = 250$ ms, the upper pitch limit is 0.25. The pitch can also be set lower to maintain some overlap as a safety buffer, in case there are irregularities in the ECG signal. The z-coverage by the detector slices as a function of time can be approximated with the interval $Z(t) = [d\ t/t_{\mathrm{rot}}, d\ t/t_{\mathrm{rot}} + C]$. If c is a target phase, the corresponding times $t_c = cT_{\mathrm{RR}} + T_{\mathrm{RR}} \cdot \mathbb{N}$. Volume stacks can be reconstructed from (parallel) data corresponding to the time intervals $[t_c - t_{\mathrm{rot}}/4, t_c + t_{\mathrm{rot}}/4]$. Note, that the angle coverage requirement for the original fan-beam data is $\pi + \Phi$ and while not 100% of the corresponding data may be used in the reconstruction, the actual temporal resolution is still slightly larger than $t_{\mathrm{rot}}/2$ [7]. That has been neglected herein. If the pitch is within limit, the stacks will, together, cover a continuous z-range and a final CT volume that ideally corresponds to the phase c can be assembled. Figure 2.11 illustrates the z-coverage for pitch values below and above the limit set by (2.14). Another limitation for the pitch can be formulated with the requirement that the detector array should not pass a z-position by more than C during the data acquisition. With the angular coverage $\pi + \Phi$, the pitch limit can be approximated by

$$p \leq 2\pi/(\pi + \Phi).$$

This is generally less restrictive than (2.14) [7]. For example, for $\Phi = 52°$, the requirement is $p \leq 1.55$.

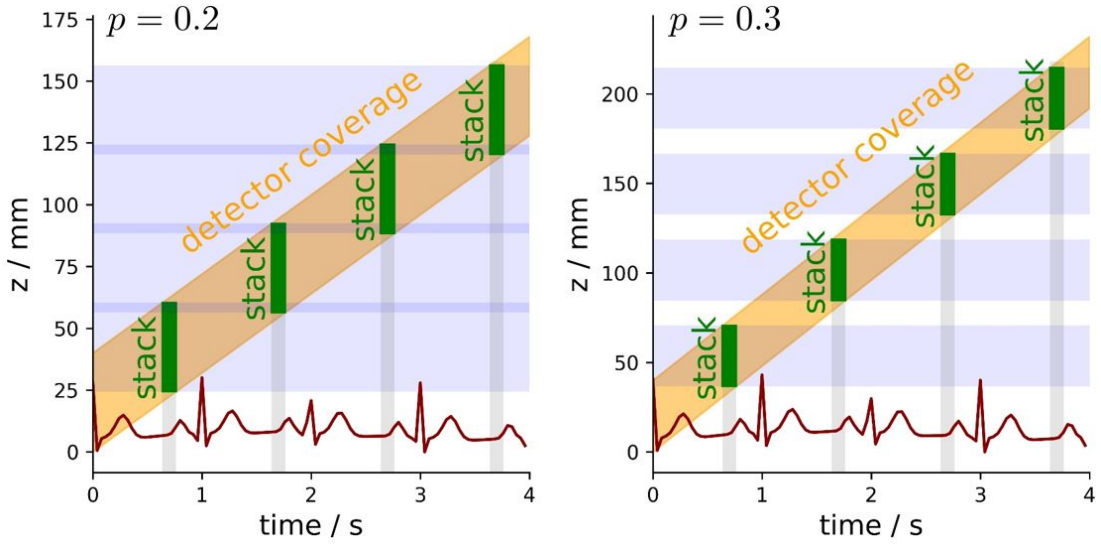

Figure 2.11: Detector coverage along the z-axis with spiral trajectories ($p = 0.2$ and $p = 0.3$). The red graph is an ECG-signal ($f_{\mathrm{H}} = 60$ bpm) and the orange band is the detector coverage ($C = 40$ mm). The green patches represent the reconstructed stack coverage in time ($c = 70\%$) and along the z-axis. The blue areas represent the overall z-coverage of all stacks. For $p = 0.2$ there are overlaps, while for $p = 0.3$ there are gaps.

Prospectively Gated Cardiac CT

In prospective gated cardiac CT, the ECG signal is used to acquire data only at predefined intervals in the cardiac cycle. A series of circular scans is performed, until a region of interest (ROI) has been covered. This is also called step-and-shoot method. Only one phase can be reconstructed, but the dose is significantly reduced [51, 125, 1]. Naturally, when choosing a time window to reconstruct, the choice would usually fall to the heart phase with the least movement. In case of the coronary artery, but not limited to it, that would be the mid or late diastole [51, 4]. However, in the late systole motion is relatively low as well and at heart rates greater than 80 bpm, the lowest velocities of the coronary artery can, in fact, be observed in a time window during the systole [51, 112]. Additionally, there are differences between the left and right arteries. While the events on both sides of the heart are similar, they are not synchronous [51]. This means that the optimal scan parameters vary depending on the specific region within the heart. These considerations are also valid for retrospectively gated scans, when using ECG-controlled tube current modulation. Note, that due to the circular trajectory, complete 180° coverage is not given for all positions. If not addressed, this may lead to cone-beam artifacts [9].

2.6.6 Motion Artifacts

A conventional CT reconstruction requires an irradiation coverage of 180° (+Π) and if a structure is moved or deformed during the scan that requirement is not fulfilled in the respective area. Naturally, the velocity of the motion has a strong impact on the extent of the artifacts. Regarding the CT scanner, the rotation time and therefore the temporal resolution are the most important factors affecting motion artifact occurence. The impact of the motion also varies depending on the motion direction with respect to the projection angles, i.e. the x-ray directions. Therefore, even given similar motion directions, velocities and irradiated areas, the appearance and magnitude of the motion artifacts may vary drastically. The artifact appearances include an apparent blurring, dark spots and streaks or curved tails seemingly emitted from structures. Figure 2.12 displays CT images with different types of artifacts. Figure 2.13 displays axial CT slices with simulated motion of different directions and the resulting motion artifacts. The applied motion is faded out at the image boundaries, but uniform otherwise. Nevertheless, the motion artifacts are only apparent in certain regions.

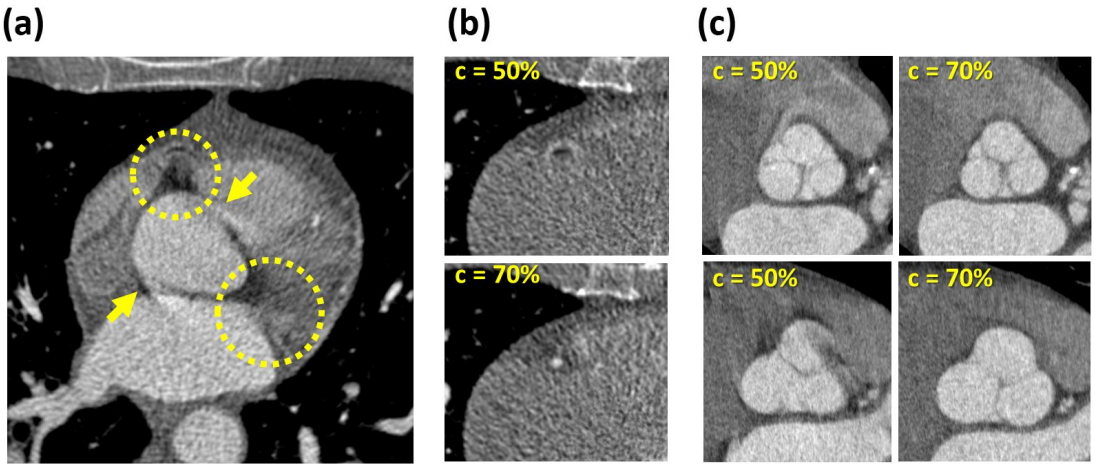

Figure 2.12: Examples for motion artifacts in cardiac CT: **(a)** Axial slice with streaks/tails, blurring and dark spots. The artifact locations are marked. **(b)** ROI (axial) with the coronary artery at two cardiac phases c, with and without artifacts, respectively. **(c)** ROI (oblique plane parallel to the aortic valve base) for two data sets, each at two cardiac phases c, with and without artifacts. $C = 200$ HU, $W = 1200$ HU.

The previously discussed motion artifacts are found in individual stacks. There is another type of motion artifact that is caused by discrepancies between the stacks. As the latter ideally correspond to the same phase, but also to different times, irregular motion may introduce said discrepancies. A phase mismatch between the stacks can also be a factor. Irregular motion has multiple origins. While one can generally not assume the cardiac motion to be 100% identical in each cardiac cycle, relatively large deviations may occur, for instance due to cardiac arrhythmia. Irregular motion can also originate

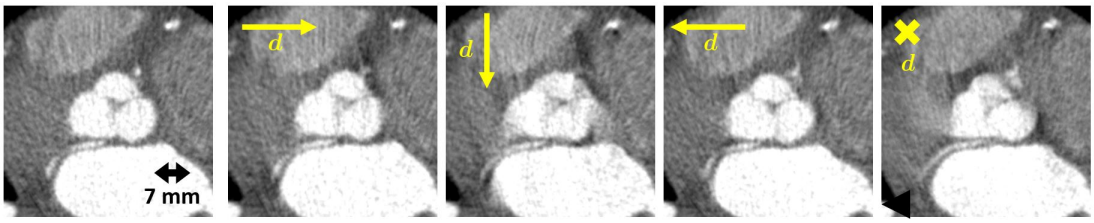

Figure 2.13: Axial slices with simulated linear motion. The motion directions are marked in the images, with the outer left image being motion free. For the outer right image the motion is perpendicular to the image plane. The velocity is 50 mm/s at a temporal resolution of 140 ms. The resulting displacement is approximately 7 mm. This length is illustrated in the motion free image. $C = 0$ HU, $W = 1500$ HU.

from breathing or basically any patient movement during the scan. When assembling the final CT volume, misalignment and discrepancies at stack transitions may arise. These will hereafter be referred to as stack transition artifacts. The longitudinal collimation of a scanner will clearly affect the occurrence of stack transition artifacts but also temporal resolution should have an effect. While faster rotation times do not necessarily help with arrhythmia, breathing or other motions will have a smaller impact. Depending on the severity of the artifacts, image quality may be considerably impaired. For instance, delicate structures like coronary arteries may appear to be broken or discontinued and larger structures like valves, ventricles or the aorta may appear displaced in neighboring slices, as is illustrated in Figure 2.14.

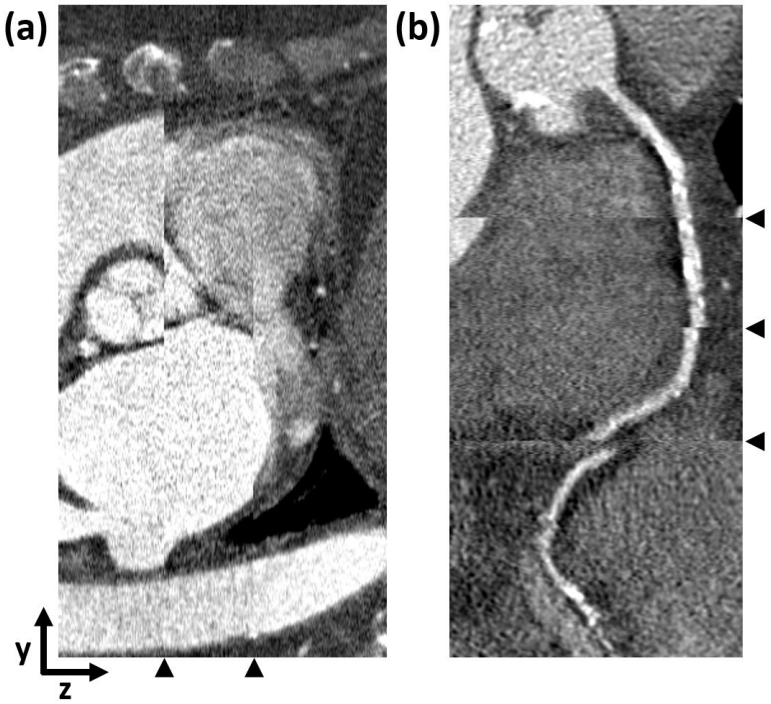

Figure 2.14: Examples for stack transition artifacts: **(a)** Sagittal CT slices. **(b)** MPR including the RCA. The stack transitions are marked with triangles. $C = 200$ HU, $W = 1000$ HU

2.6.7 Motion Compensation

Motion compensation (MoCo) algorithms make use of the fact that organ motion in general and cardiac motion in particular is a continuous type of motion and thus can be modeled using MVFs. Using this prior knowledge allows to overcome the hardware limitation to some extent and to improve on the temporal resolution. Apart from improving the image quality, improving the temporal resolution may decrease the need for drug-related measures such as the use of β–blockers[22].

Numerous MoCo algorithms utilize data from adjacent cardiac phases. Such methods match phase-selective reconstructions, for instance using non-rigid image registration, to estimate the motion that the data are subsequently corrected for [18, 19, 20, 21, 22, 23]. Therein, not necessarily the entire reconstruction is used. For example, the registration may be focused on specific (extracted) features such as the coronary artery tree line [22, 19] or the surface of the ventricles [18]. Non-rigid image registration is capable of computing MVFs that consider the elastic organ deformations. In order to find a suitable transformation, a similarity or distance measure is defined [126]. Such measures can be based on the voxel values or on geometric structures or landmarks (e.g. bones, organ boundaries) [127]. Examples are the mutual information (MI) and the entropy correlation coefficient (ECC). MI measures the amount of information that one

image contains about the other, using the image entropy and the joint entropy. The image entropy is a measure for the information content and also the image sharpness [25, 128]. The joint entropy measures the information content in the combined images [129]. ECC measures the statistical dependence between the images [129]. A measure may be optimized iteratively if no analytical solutions are available. One may also want to use only a single cardiac phase, as it is done in dose-optimized scan protocols that perform short scans (e.g. step-and-shoot method). Using prospective gating, the data acquisition can be limited to a minimal time window within the heart cycle. MoCo approaches, focusing on coronary artery imaging and utilizing short scan data have been proposed [25, 26]. Since no temporal redundancies are available in the single-phase data, the motion has to be estimated using a MAM. MAMs compute a metric/measure for images that can be related to the amount and the magnitude of motion artifacts. For example, the image entropy has been used as MAM [25, 128]. The estimated motion can be applied during the reconstruction process [25] or the motion model may rely on transforming separate PARs [26]. PARs are reconstructions of sub 180° rawdata sections. If a set of the latter covers 180° in the rawdata domain, a set of PARs can be reconstructed, the sum of which results in a CT image. If each PAR corresponds to a time (interval) in a 180° equivalent reconstruction window, the former can be transformed with time dependent MVFs, resulting in changes for the corresponding CT image. PARs were also used in MoCos without MAMs. Therein, motion was estimated by registering PARs separated by 180° [130, 24]. Figure 2.15 displays examples for coronary artery motion compensation performed with the partial-angle and image entropy based PAMoCo [26].

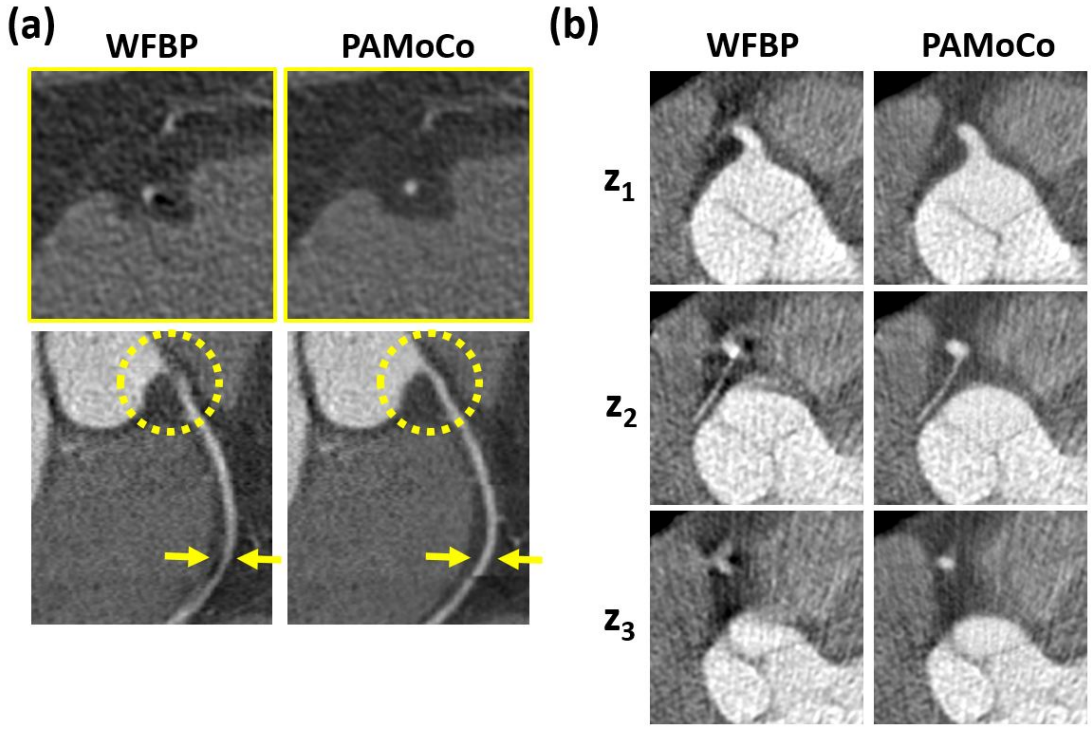

Figure 2.15: **(a)** Axial slices and curved MPRs displaying the RCA reconstructed with WFBP and PAMoCo. The location of the axial slice is marked with arrows in the MPR. $C = 200$ HU, $W = 1200$ HU. **(b)** Series of axial slices spaced 3 mm apart displaying the RCA reconstructed with WFBP and PAMoCo. $C = 0$ HU, $W = 1500$ HU.

3 Methods

3.1 Reconstruction

FOVs are manually selcted for the reconstructions. They will generally cover the entire heart or a large portion of it. Let c_0 be the cardiac target phase for reconstruction. At least one 180° section of raw data is extracted. It corresponds to a phase window $[c_0 - \frac{\Delta c}{2}, c_0 + \frac{\Delta c}{2}] = [c_S, c_E]$. The data are assumed to already have been rebinned to parallel beam geometry. A set of stacks is reconstructed from said sections via WFBP. The stacks, that generally have a longitudinal overlap, can be combined to form a CT-volume that covers the entirety of the FOV. The final CT volume is acquired by populating the voxels with gray values from the stacks. The stack transition, at which the source stack is switched to the next stack, is placed in the center (along the z-axis) of the overlapping region between neighboring stacks. An illustration of the stacks and transitions is displayed in figure 3.1. The reconstructions featured voxel sizes between 0.3 to 0.4 mm and slice increments of 0.3 mm with 0.6 mm slice widths.

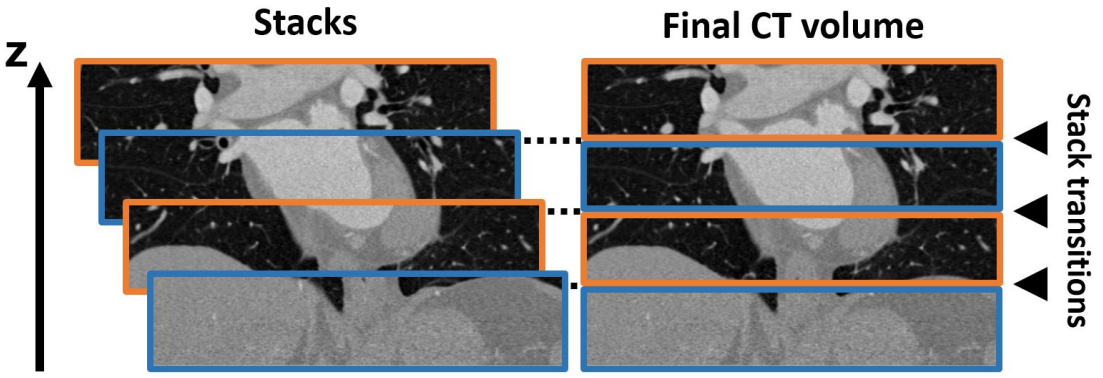

Figure 3.1: 2D illustration of stacks and the assembly of the final CT volume using coronal slices from a cardiac CT reconstruction.

3.2 Stack Transition Artifact Removal

The following section describes the stack transition artifact removal (STAR) algorithm. This method has been published in [131] and similar methods in [132, 133]. Given S longitudinally overlapping stacks g_s, the goal is to compute MVFs in the overlaps, to register the stacks and subsequently expand the MVFs to cover the entire volume via interpolation, in order to perform continuous and smooth transformations that will remove artifacts in the final CT volume. The MVFs are optimized sequentially for each pair of adjacent stacks.

Symmetric Demons algorithm

Symmetric image registration, as implemented and applied in this work, is defined as follows. Given two volumes f_1, f_2, the aim is to compute a MVF $\boldsymbol{d}(\boldsymbol{r})$ such that the transformed volumes $T_{+\boldsymbol{d}}\ f_1(\boldsymbol{r}) = T_{-\boldsymbol{d}}\ f_2(\boldsymbol{r})$ with

$$\begin{aligned} T_{+\boldsymbol{d}}\ f_1(\boldsymbol{r}) &= g_1(\boldsymbol{r} + \boldsymbol{d}(\boldsymbol{r})) \\ T_{-\boldsymbol{d}}\ f_2(\boldsymbol{r}) &= g_2(\boldsymbol{r} - \boldsymbol{d}(\boldsymbol{r})). \end{aligned} \tag{3.1}$$

As can be seen from the equations, the MVF $\boldsymbol{d}$ is applied in opposing directions in both volumes, respectively. A symmetric Demons algorithm was derived similar to the derivation of Thirion's demons algorithm [134, 135]. In accordance with past works in the field, a cost function C is defined. The input consists of a final MVF $\boldsymbol{d}$ and an intermediate MVF $\boldsymbol{e}$. Both are 3D MVFs. The cost function includes a similarity measure, a regularization applied to the MVF $\boldsymbol{d}$, and an auxiliary term named correspondence that introduces a coupling between the intermediate and final results. This enables a decoupling of the optimization of the similarity and the regularization in two separate steps. Given M voxels at positions $\boldsymbol{r}_m$ with $1 \leq m \leq M$ the cost function can be expressed as

$$\begin{aligned} C(\boldsymbol{d}, \boldsymbol{e}) = &\sum_m \frac{1}{\sigma_{\mathrm{i}}^2(\boldsymbol{r}_m)} (T_{+e} f_1 - T_{-e} f_2)^2(\boldsymbol{r}_m) \\ &+ \frac{1}{\sigma_{\mathrm{x}}^2} \sum_m (\boldsymbol{d} - \boldsymbol{e})^2(\boldsymbol{r}_m) + \frac{1}{\sigma_{\mathrm{T}}^2} \sum_m (\nabla \boldsymbol{d}(\boldsymbol{r}_m))^2. \end{aligned} \tag{3.2}$$

The cost function term weights σ_{i}^{-2} and σ_{T}^{-2} account for the image noise and the regularization strength, while σ_{x}^{-2} weights the correspondence and therefore affects the spatial uncertainty between $\boldsymbol{d}$ and $\boldsymbol{e}$. The choice of these parameters will be discussed in a later paragraph. The optimization for one iteration is performed in two steps separating the cost function. First, image similarity and correspondence are optimized and given a MVF $\boldsymbol{d}$ from the previous iteration, an additive update $\Delta\boldsymbol{d}$ is computed to acquire the intermediate result $\boldsymbol{e} = \boldsymbol{d} + \Delta\boldsymbol{d}$. Second, the correspondence and regularization are optimized and given the intermediate result $\boldsymbol{e}$, a MVF $\hat{\boldsymbol{d}}$ is computed as final result for the current iteration. The update steps are as follows.

$$\Delta\hat{\boldsymbol{d}} = \underset{\Delta\boldsymbol{d}(\boldsymbol{r}_m)}{\arg\min} \frac{1}{\sigma_{\mathrm{i}}^2(\boldsymbol{r}_m)}(T_{+d+\Delta d}\, f_1 - T_{-d-\Delta d}\, f_2)^2(\boldsymbol{r}_m) + \frac{1}{\sigma_{\mathrm{x}}^2}\Delta\boldsymbol{d}^2(\boldsymbol{r}_m)$$
$$\hat{\boldsymbol{d}} = \underset{\boldsymbol{d}(\boldsymbol{r}_m)}{\arg\min} \frac{1}{\sigma_{\mathrm{x}}^2}(\boldsymbol{d} - \boldsymbol{e})^2(\boldsymbol{r}_m) + \frac{1}{\sigma_{\mathrm{T}}^2}(\nabla\boldsymbol{d}(\boldsymbol{r}_m))^2$$

Regarding step one, the similarity term can be linearized via a first order approximation. Using the latter and evaluating the cost function at each voxel individually yields an analytic formula for $\Delta\hat{\boldsymbol{d}}(\boldsymbol{r}_m)$ in the first optimization step that can be applied for each voxel independently:

$$\Delta\hat{\boldsymbol{d}}(\boldsymbol{r}_m) = \frac{(T_{+d}f_1 - T_{-d}f_2)(\boldsymbol{r}_m)(T_{+d}\nabla f_1 + T_{-d}\nabla f_2)(\boldsymbol{r}_m)}{\frac{\sigma_{\mathrm{i}}^2}{\sigma_{\mathrm{x}}^2} + (T_{+d}\nabla f_1 + T_{-d}\nabla f_2)(\boldsymbol{r}_m)^2}.$$

As for the second step, the cost function can once again be evaluated at each voxel individually. Using differential calculus and applying the Fourier transform, forth and back, while using one of its unique characteristics, $\mathcal{F}\left(\frac{d^2 f(x)}{dx^2}\right) = -(2\pi u)^2 F(u)$, yields a convolution of the intermediate MVF $\boldsymbol{e} = \boldsymbol{d} + \Delta\boldsymbol{d}$. The resulting convolution kernel is a function proportional to $e^{|\boldsymbol{r}|}$. However, here a Gaussian kernel is used instead. The advantages of the latter include a simple and efficient application. Finally, the symmetric Demons algorithm yields the MVF for the iteration:

$$\hat{\boldsymbol{d}}(\boldsymbol{r}) = \boldsymbol{e}(\boldsymbol{r}) * \frac{1}{\sqrt{2\pi}(\sigma_{\mathrm{x}}/\sigma_{\mathrm{T}})} \exp\left(-\frac{\boldsymbol{r}^2}{2(\sigma_{\mathrm{x}}/\sigma_{\mathrm{T}})^2}\right). \tag{3.3}$$

At this point one may also filter the MVF update $\Delta\hat{\boldsymbol{d}}$ instead of the updated MVF $\boldsymbol{e}$ [135]. However, the resulting, repeated smoothing of the MVF in the latter case may require a smaller smoothing parameter to achieve similar results. Consequently, a smaller convolution kernel may be used improving computational performance in the current implementation.

Motion vector field interpolation

Given S stacks, $S-1$ registrations have to be performed for neighboring stack pairs g_s, g_{s+1}. One registration includes the upper overlapping region of a stack s and the lower overlapping region of the subsequent stack $s+1$, which correspond to f_1, f_2 in (3.1). Each stack g_s covers a z-axis range $z_{s,1}$ to $z_{s,2}$. All registrations yield MVFs $\boldsymbol{d}_s$ that are only valid in the upper overlapping region of their respective stack ($z_{s+1,1} < z < z_{s,2}$). In order to compute smooth MVFs that are valid for an entire stack each, linear interpolations between the deformation vectors from the lower and upper overlapping regions are performed. Based on (3.1), the MVF for the lower overlapping region of a stack g_s is $-\boldsymbol{d}_{s-1}(\boldsymbol{r})$. The interpolations are computed in longitudinal direction only and between the inner edges of the overlap. This means that also the non-overlapping

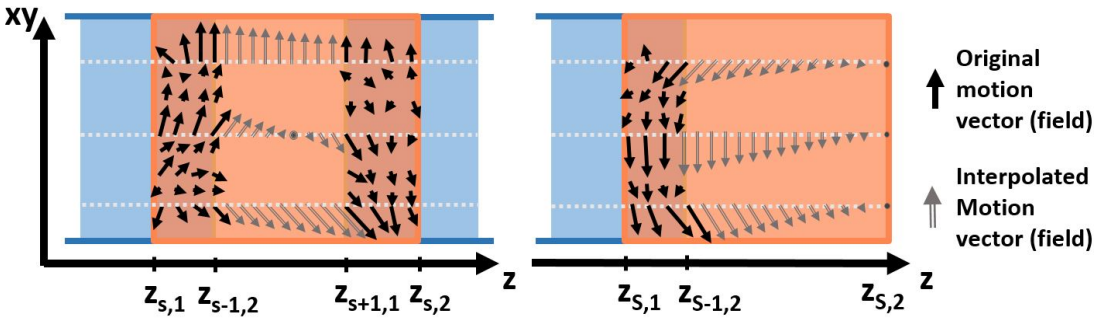

Figure 3.2: 2D illustration of the MVF interpolation.

stack regions are transformed, however this is necessary in order to have a continuous MVF for the stack and the transformation outside the overlaps to be smooth. The transformed stacks $Tg_s(\boldsymbol{r})$ can be computed as

$$\begin{aligned} Tg_s(\boldsymbol{r}) = g_s\Big(\boldsymbol{r} - \left(\frac{z_{s+1,1} - z}{z_{s+1,1} - z_{s-1,2}}\right) \boldsymbol{d}_{s-1}(x, y, z_{s-1,2}) \\ + \left(\frac{z - z_{s-1,2}}{z_{s+1,1} - z_{s-1,2}}\right) \boldsymbol{d}_s(x, y, z_{s+1,1}) \quad \Big). \end{aligned} \tag{3.4}$$

Furthermore, let $\boldsymbol{d}_0$, $\boldsymbol{d}_S = 0$ as well as $z_{0,2} = z_{1,1}$ and $z_{S+1,1} = z_{S,2}$ in order for (3.4) to be valid for the outer stacks ($s = 1; S;$) so that the MVFs are faded out towards their respective outer boundaries. The interpolation is illustrated in figure 3.2.

Parameterization

Given the update equations, one has to choose the parameters σ_i, σ_x, σ_T. The voxel–dependent parameter accounting for the image noise $\sigma_\mathrm{i}(\boldsymbol{r}_m)$ is set to a local estimation of the image noise. This further allows the use of σ_x to directly limit the update length $\sqrt{\|\delta \boldsymbol{d}_m\|_2^2} \leq \sigma_\mathrm{x}/2$ [135]. As can be seen from (3.3) σ_x and σ_T define the standard deviation for the Gaussian kernel. Finally, one can define two free parameters to control the algorithm: δ is the maximum step length for the first optimization step and σ defines the kernel width for the second optimization step, where $\sigma_\mathrm{x} = 2\delta$ and $\sigma_\mathrm{T} = 2\delta/\sigma$. The parameters δ and σ have to be balanced. Strong smoothing compared to small update steps, i.e. $\Delta \ll \sigma$, will compromise the update, limiting registration performance. At the same time, too high a value for Δ may result in extensive MVF updates lacking precision. In the current implementation, Δ is set as a function of the smoothing parameter: $\Delta = \Delta(\sigma) = \sigma$. This leaves the smoothing as the only free parameter. A strong smoothing limits the algorithm, while too little smoothing yields an unrealistic MVF.
A requirement that comes before registration performance is the computation of a realistic MVF. For clinical data this includes not just a smooth MVF but also the

absence of distortions in the final volume. Those may be stretching, contraction or generally extensive manipulation of small structures like coronary arteries or individual cardiac valve leaflets. Therefore, the smoothing parameter must be sufficiently high to prevent this, given all possible magnitudes of deformation that the MVF updates may yield. It is possible to choose one value for σ for all applications, however a high value to ensure the mentioned requirement will presumably unnecessarily limit registration performance for cases without large deformations. A more desirable solution is an adaptive smoothing that is set automatically. For this purpose, the Demons algorithm is initially applied with weak smoothing, e.g. $\sigma_{\text{initial}} = 0.5$ mm, to estimate an initial MVF that reflects the amplitudes necessary to match the volumes. Based on the maximum encountered MVF amplitude MVF_{max} the smoothing for the actual Demons registration is set, e.g. $\sigma = 0.5\ \text{MVF}_{\text{max}}$. This allows for more precision for data sets with less mismatch. A lower limit for the smoothing parameter has to be set to prevent errors in data with little to no mismatch, e.g. $\sigma_{\text{min}} = 2$ mm. This automatic parameter selection is performed with each registration, i.e. sequentially for every stack pair.
The smoothness requirement also means, that some artifacts may remain. Small scale changes, like changing the diameter of a coronary artery or moving individual valve leaflets, must not be allowed. The former may also include fine distributions of contrast agent in a ventricle or even motion artifacts that may vary or be present/absent in one of the stacks. Naturally, stack mismatch due to such reasons can not be corrected as a result.
The iterative updates for the Demons algorithm are, by design, analytical and dependent on local topology. That introduces potential issues when encountering large deformations. Given equivalent, displaced structures that have little or no overlap in the stacks, the registration may fail in the respective region. In order to improve registration performance, the Demons algorithm is applied at multiple resolution levels. The maximum voxel size is limited to 3 mm and the spatial resolution is stepwise improved by a factor of two until reaching the original resolution (e.g. 2.4 mm→1.2 mm→0.6 mm→0.3 mm). A subsequent registration is initialized with the upscaled MVF from the previous resolution. The same smoothing parameter is applied at all resolution levels with the limitation that σ must be larger or equal to the voxel size.
The MVF is computed within the overlapping region, however the algorithm is able to reach outside the overlap to pull gray values in from the rest of the stack.
The Demons algorithm is stopped by a convergence criterion or after reaching a maximal amount of iterations. The convergence criterion checks the change in the mean quadratic difference of the transformed volumes. A maximum iteration number of 100 was found sufficient to ensure satisfactory results.

3.3 Partial Angle Reconstruction-Based Motion Compensation

The following section describes the partial angle reconstruction based motion compensation for cardiac valves (valve MoCo). This method uses a penalized image entropy as

motion artifact metric and requires one reconstruction/data from one cardiac phase. It is based on the previously published partial angle motion compensation (PAMoCo) [128] that was aimed at coronary arteries. The herein described method has been expanded to be applicable to cardiac valves. In particular, the aortic valve. The reconstructed volumes FOV is selected such that it is centered around the aortic valve. The goal is to determine a set of free parameters of a motion model that will ideally result in the removal of motion artifacts in the processed stack.

Partial angle reconstructions

For each section/stack the raw data are split into $2K + 1$ overlapping segments. A set of partial angle reconstructions (PARs) $\boldsymbol{f}_k$ with $-K \leq k \leq K$ is reconstructed. A PAR $\boldsymbol{f}_k$ corresponds to a phase c_k and the central PAR $\boldsymbol{f}_0$ corresponds to the target reconstruction phase c_0. Let the raw data segments be centered around angles $\vartheta_k = \vartheta_0 + k\Delta\vartheta$ with $-K \leq k \leq K$. The step between PARs is $\Delta\vartheta = \pi/(2K + 1)$ and corresponds to a duration $dt_{\Delta\vartheta} = t_{\text{rot}}/(2(2K + 1))$ for single source CT with a rotation time t_{rot}. The segments cover an angular range of $2\Delta\vartheta$ and overlap by $\Delta\vartheta$. The redundancy introduced by the overlap is dealt with by weighting the raw data segments using a $\cos^2$-function prior to reconstruction. The temporal resolution of each PAR is $t_{\text{rot}}/(2K + 1)$. Herein, $K = 15$. With the weighting of the raw data segments, the sum of the PARs yield the conventional reconstruction. Sinogram weighting and PARs are illustrated in figure 3.3.

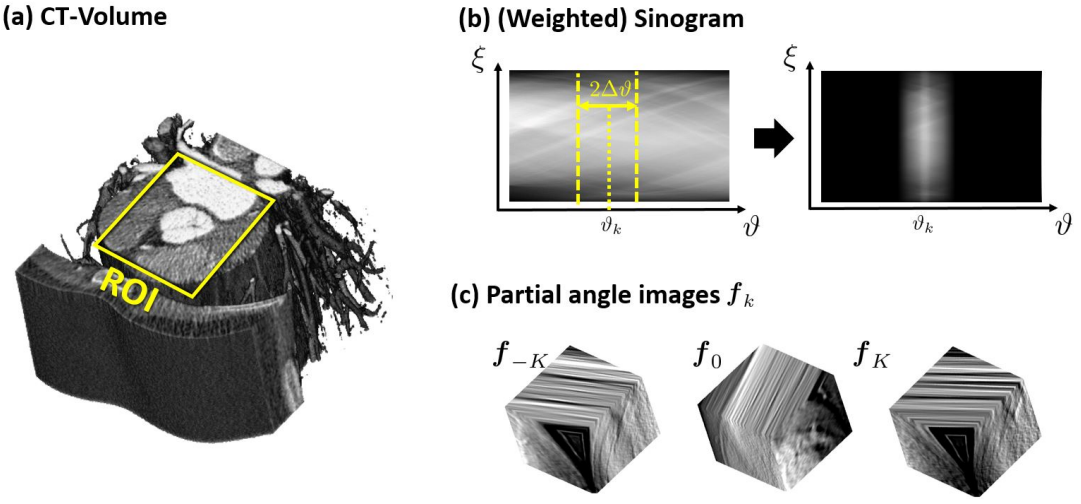

Figure 3.3: Illustrations: **(a)** Cardiac volume. **(b)** Sinogram weighting. **(c)** PARs.

Interpolation

The partial angle reconstruction based motion compensation uses linear interpolation to compute transformed CT volumes. The MVFs are interpolated via monotone piecewise cubic interpolation [136]. The latter is performed as follows. Let L control points P_l with $1 \leq l \leq L$ be located at positions x_l at constant distances h from each other. A piecewise cubic function $f(x)$ with $f(x_l) = P_l$ is computed in an interval $[x_l, x_l + 1]$ as

$$f(x) = P_l H_1(x) + P_{l+1} H_2(x) + \Delta_l H_3(x) + \Delta_{l+1} H_4(x),$$

with the first derivates $\Delta_l = \partial/\partial x \; f(x)|_{x=x_l}$. The polynomials H_1 to H_4 are defined as

$$\begin{aligned} H_1(x) &= \phi((x_{l+1} - x)/h), \\ H_2(x) &= \phi((x - x_l)/h), \\ H_3(x) &= -h\psi((x_{l+1} - x)/h), \\ H_4(x) &= h\psi((x - x_{l+1})/h) \end{aligned}$$

with $\phi(\chi) = 3\chi^2 - 2\chi^3$ and $\psi(\chi) = \chi^3 - \chi^2$ being two hermite basis functions. The derivatives Δ_l are computed as differences between control points. It can be shown, that $f(x)$ is monotone in $[x_l, x_{l+1}]$ [136]. Therefore, finding a minimum or maximum of $f(x)$ only requires evaluations of the control points. In order to perform 2D cubic interpolation on a control point grid $P_{l,m}$, subsequent 1-dimensional (1D) interpolations are performed to compute the functions $f(x, y_m)$ that subsequently serve as control points for a 1D interpolation to compute $f(x, y)$. Similarly, in order to perform 3D cubic interpolation on a control point grid $P_{l,m,n}$, subsequent 2D interpolations are performed to compute the functions $f(x, y, z_n)$ that finally serve as control points for a 1D interpolation to compute $f(x, y, z)$.

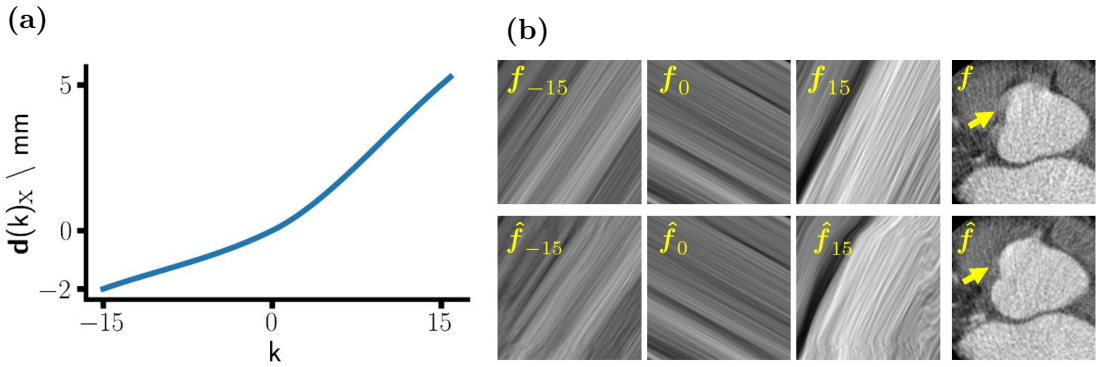

Figure 3.4: **(a)** Plot of a motion model vector component with the temporal control points (-2 mm; 0 mm; 5 mm). **(b)** Axial slices from PARs and the respective CT images $\boldsymbol{f} = \sum_k \boldsymbol{f}_k$ for K=15. The top row shows non transformed PARs and the CT image with motion artifacts. The bottom row shows PARs that were transformed in a way, such that the motion artifacts are removed in the respective CT image. An area with artifacts is marked.

Motion Model

The algorithm computes MVFs $\boldsymbol{d}_k$ that are applied to the PARs $\boldsymbol{f}_k$ as follows:

$$\hat{\boldsymbol{f}}_k(\boldsymbol{r}) = \boldsymbol{f}_k(\boldsymbol{r} + \boldsymbol{d}_k(\boldsymbol{r})). \tag{3.5}$$

Summing up the transformed PARs $\hat{\boldsymbol{f}}_k$, ideally, yields a corrected CT volume. A monotone piece-wise cubic interpolation of a set of control points in temporal domain is performed to acquire motion vectors $\boldsymbol{d}_k$. The temporal control points $\boldsymbol{D}_p \in \mathbb{R}^3$ with $p \in \{-1, 0, 1\}$ are defined at coordinates $k_p \in \{-K, 0, K\}$. Consequently, $h = K$. Let $\boldsymbol{D}_0 = 0$. By design, $\boldsymbol{D}_{-1} = \boldsymbol{d}_{-K}$ and $\boldsymbol{D}_1 = \boldsymbol{d}_K$ are the maximum deformations prior to and after $k = 0$, unless set to zero. The derivatives Δ_p are computed using finite differences. Boundary conditions are required in order to set $\Delta_{\pm 1}$. The former are realized by introducing new control points $\boldsymbol{D}_{\pm 2} = 2\boldsymbol{D}_{\pm 1}$. The derivatives are $\Delta_p = \boldsymbol{D}_{p+1} - \boldsymbol{D}_{p-1}$. The velocity can be acquired as $\boldsymbol{v}_k = \frac{\partial}{\partial k}\boldsymbol{d}_k / dt_{\Delta\vartheta}$. Given $\boldsymbol{D}_0 = 0$, all PARs are transformed with respect to the central PAR $\boldsymbol{f}_0$. Figure 3.4 shows an example for a vector $\boldsymbol{d}$ as a function of k as well as PARs that have been transformed such that the resulting CT image is corrected for motion artifacts.
A smooth MVF that is defined in the entire stack is computed using a motion model that is parameterized on a spatial 3D grid of evenly distributed control points. Each of the spatial control points is indexed via l, m, n and assigned a set of temporal control points $\boldsymbol{D}_{p,l,m,n}$. A 3D monotone cubic interpolation is performed based on the spatial control point grid in addition to the temporal interpolation. Consequently, a 4D MVF $\boldsymbol{d}_k(\boldsymbol{r})$ can be computed. The derivatives $\Delta_{l/m/n}$ are computed using finite differences. The distance h is equal to the control point distances/the grid constant. At the outer boundaries of the 3D grid the control points are continued uniformly for

the interpolation. The MVF is faded out towards the outer boundaries of the ROI. Herein, the target grid constant is 2.5 cm. The minimal grid size is set to $2 \times 2 \times 2$ and the actual grid constants may have to be adjusted in individual directions to fit the grid into the ROI. It is important to keep the MVFs smooth to maintain anatomically realistic deformations. The resulting volume must be distortion-free and the functional state of the valve, primarily the leaflets, must be maintained as well. A smoothness criterion is imposed on the MVF by regularizing the cost function.

Cost function

The cost function of the motion compensation has the function of a MAM that also favors a realistic MVF. The cost function includes the ratio q_E of the image entropy to the initial/input image entropy. The image entropy is computed as

$$E = -\sum_h p(\eta)\log(p(\eta)),$$

where $p(\eta)$ is the probability to encounter the value η. The image entropy is a measure for the information content of an image and has been previously used as a MAM [25, 128]. To impose restrictions on the MVF, two regularization terms R_{vel} and R_{grad} are defined to penalize velocity and the MVF gradient. Let q_{vel} be the ratio of a maximum velocity (for all k, l, m, n) to a reference velocity V_{ref}. Let q_{grad} be the ratio of a maximum gradient metric (for all k, l, m, n) to a reference gradient value G_{ref}. The gradient metric is simply the root of the squared sum of the entries of the MVF Jacobian. The MVF Jacobian $\boldsymbol{J}$ is computed (for each k, l, m, n) as

$$\boldsymbol{J} = \left(\frac{\partial(\boldsymbol{d}_{klmn})_i}{\partial j}\right)_{i,j=x,y,z}.$$

The two penalties are computed as

$$R_{\text{vel/grad}} = \frac{1}{e-1}\left(\exp(q^4_{\text{vel/grad}}) - 1\right).$$

The cost function is

$$C = q_E + \Delta E_{\text{ref}}(R_{\text{vel}} + R_{\text{grad}}).$$

The penalty term weight ΔE_{ref} represents the maximum magnitude by which E is expected to change during the optimization. It is estimated automatically for an individual motion compensation task (i.e. one stack) by applying MVFs with a velocity V_{ref} in different directions and computing the mean change of q_E. Given the cost function, the reference values V_{ref} and G_{ref} act as a soft upper limits, with a sharp increase of the penalty terms for $q > 1$. Velocities in the myocardium of up to 120 mm/s, sometimes more, have been observed [114, 115, 116]. The velocity reference value is set

to $V_{\text{ref}} = 70$ mm/s. Regarding the elasticity of the heart, the entries of the Jacobian can be used to compute cardiac strain values. The strain can be defined as a unitless measure for the relative deformation of a body with respect to an initial length/size. Typical cardiac strain values vary with region and orientation. Strain in the range of 10% to 40% has been observed [137, 138]. The gradient reference value is set to $G_{\text{ref}} = 0.15$.

Optimization

Cost function optimization is achieved using the conjugate directions method by Powell [139]. It starts as a conventional grid search along the solution space basis vectors and gradually replaces search directions by a combination of last iterations searches. For the optimization, PARs with voxel sizes of 0.6 mm $\times$ 0.6 mm $\times$ 0.6 mm are reconstructed. The estimated motion is finally applied to PARs with the original CT volumes resolution. The optimization is at first performed without the penalties $R_{\text{Vel/Grad}}$ as an initialization for a second, penalized optimization.

3.4 Simulation

A simulation was performed based on patient data to generate stack transition artifacts. Two artificial stacks, identical in their overlap, were created from a reconstructed volume. Gaussian noise was simulated resulting in an additional standard deviation of roughly 20 HU in soft tissue. A uniform MVF was then applied symmetrically to generate stack transition artifacts. Outside the overlap it was faded out. This MVF also serves as the ground truth. Note that the total displacement between stacks is twice the MVF amplitude. Depending on the direction and the amplitude of the vector field, data may be moved out of the overlap. These data or structures shared by the two stacks are then missing during the registration. The impact of these missing data is important to consider. Although the simulated MVFs are not realistic they well serve to demonstrate the performance of STAR. Since the MVFs are invertible, apart from a narrow border region where data may have moved out of the stack's FOV, applying an inverted ground truth MVF will yield the original/ground truth stacks, showing how well STAR can reproduce a given ground truth.

3.5 Phantom Measurements

An AV phantom resembling the aorta and the left ventricle, including the AV, was designed and 3D printed. The design was based on a segmentation of a cardiac CT data set. The phantom includes two cavities in the aorta and the left ventricle, which can be filled with water and contrast agent and sealed with screw plugs. The measurement setup was as follows. The AV phantom was attached to a motion phantom capable of generating linear motion. The later was generated only in the z-direction. The AV phantom, still connected to the motion phantom, was submerged in a water basin, in which it could be moved. The water basin was inserted into a thorax phantom. The

AV phantom and the entire phantom setup are displayed in figure 3.5. A more detailed description of the phantoms and the measurements is provided in the appendix. The

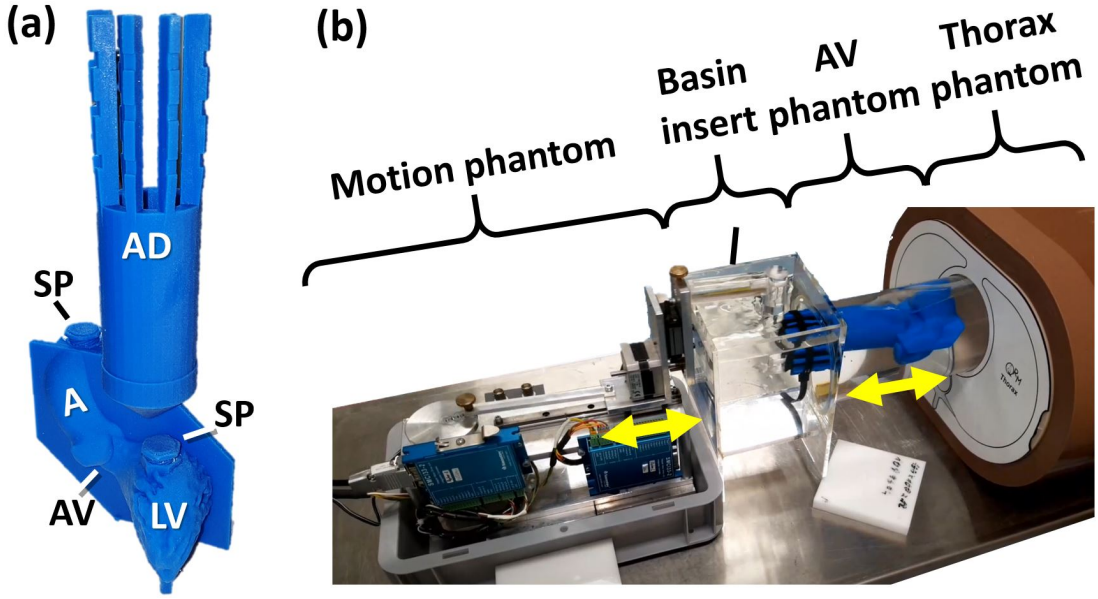

Figure 3.5: **(a)** AV phantom. The following components are marked: aorta (A), left ventricle (LV), aortic valve (AV), screw plugs (SP), attachement device for a pole (AD). **(b)** Phantom setup for the measurement. The water basin is not inserted into the thorax phantom in this image. The motion introduced by the motion phantom are marked with arrows.

phantom was scanned sequentially, in step-and-shoot mode, at a Somatom CounT CT scanner (Siemens Healthineers, Forchheim, Germany) with 100 kV tube voltage, 100 mAs and a rotation time of 0.5 s. Motion-free phantom scans (at 200 mAs) provided a ground truth.

3.6 Evaluation

Stack transition artifact removal

For the evaluation of STAR, clinical data sets including stack transition artifacts were selected. The CT images, both from WFBP and STAR, were visually inspected for the presence of stack artifacts. It was also checked, whether STAR introduced any distortions, i.e. deformations that can be considered excessive and unrealistic in the heart. Axial, sagittal and coronal slices were viewed. In addition, curved MPRs containing the RCA were extracted after manually tracing the RCA in the CT volumes. This procedure is illustrated in figure 3.6. The numerical evaluation was performed via similarity metrics. The root mean square error (RMSE) between neighboring stacks

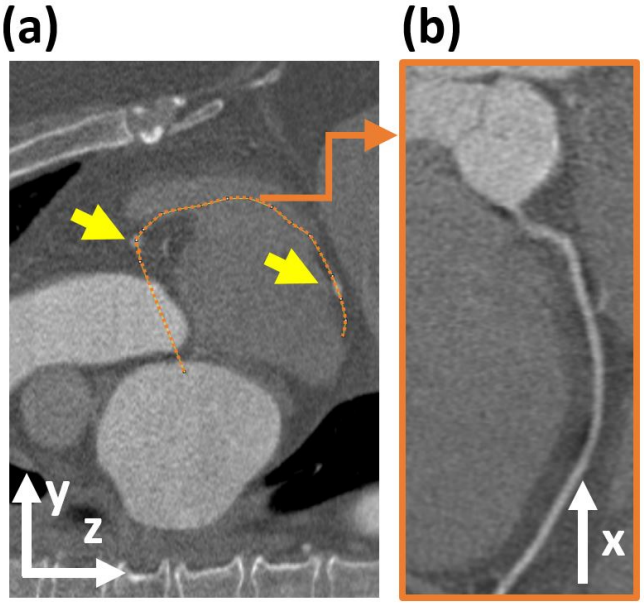

Figure 3.6: **(a)** Illustration of the RCA tracing in a sagittal CT slice. The positions of the RCA within the displayed slice are marked with arrows. The dotted line marks the curved plane containing the RCA. **(b)** MPR containing the RCA. The former is the curved plane from (a) resampled and displayed as a 2D image. $C = 200$ HU, $W = 1200$ HU.

(in the overlap) was computed. Let σ_{diff} be the error for a voxel of the stack overlap difference image $\boldsymbol{f}_{\text{diff}}$. The former is estimated as the standard deviation of $\boldsymbol{f}_{\text{diff}}$. The error propagation for the RMSE yields

$$\sigma_{\text{RMSE}} = \left| \frac{\bar{\boldsymbol{f}}_{\text{diff}}}{\text{RMSE}} \sigma_{\text{diff}} \right| ,$$

where $\bar{\boldsymbol{f}}_{\text{diff}}$ is the difference image mean value. In addition, the image entropy was applied to the difference between two consecutive slices at the stack transition. Figure 3.7 displays examples for various difference images and the respective entropy values. The difference image entropy is also computed for each other neighboring slice pair of the CT volume. The resulting population of entropy values yields a mean value used as reference and a standard deviation used as the error σ_{E} for the difference entropy at the stack transition. The errors of the two described similarity metrics reflect usual variations within the volumes and can be compared against the changes induced by STAR to check for their significance. Regarding the simulation, the results were numerically evaluated for homogeneous MVFs. Furthermore, non-homogeneous MVFs were simulated to check whether the method converges to a given ground truth MVF.

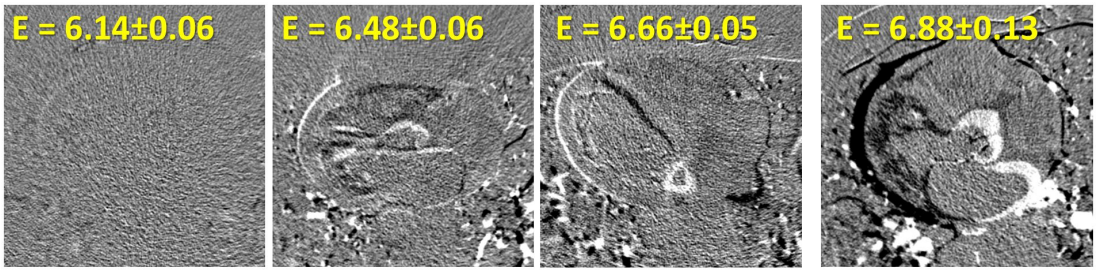

Figure 3.7: Various difference images obtained from overlapping stacks and the respective image entropies E. $C = 0$ HU, $W = 1000$ HU.

Partial angle reconstruction-based motion compensation

For the evaluation of the valve MoCo, clinical data with and without motion artifacts were selected. A cubic ROI with a width of 7 cm was centered around the AV. Only stacks that overlapped with the ROI were processed using valve MoCo. The CT images, both from WFBP and valve MoCo, were visually inspected for the presence of motion artifacts and distortions. The images were displayed as oblique planes that are parallel to the base of the AV (AV planes). For each case, one AV setting was determined and used for all reconstructions of the respective case. The AV plane orientation was determined similar to methods given in literature [122]. Starting from an orthogonal view of the CT volume centered at the AV, the sagittal and coronal planes are aligned with the long axis of the aortic root and the axial slice is tilted such that it is orthogonal to the former three. The tilted axial slice is moved along the aortic root long axis to the base of the AV and the orientation of the former is adjusted such that it intersects all three hinge points. This can be easily checked by regarding whether all three hinge points appear at the same time, when shifting the slice upwards, away from the ventricle and bringing the AV into view. Finally, two AV slices are selected. One at the AV base with the hinge points, and one at the center ov the AV. These steps are illustrated in figure 3.8. The hinge point coordinates in 3D space and the AV slice coordinates on the aortic root long axis were stored for repeated use. Reconstructions were performed at 50% and 70% cardiac phase. Given one phase with minimal motion artifacts, the respective image served as a reference. The initial reconstructions are classified as one of three categories: with major motion artifacts, with minor motion artifacts or without motion artifacts. A major artifact case constitutes any image where the structure/shape of the AV is clearly disrupted. For the classification, motion artifacts in and at the entire AV are considered, however stack transition artifacts are not. The hereafter displayed image slices for the evaluation of the valve MoCo will be positioned at the center and at the base of the AV, respectively. Figure 3.9 displays examples for the three classifications of artifacts in different slices. The motion-compensated images are checked for changes in image quality. The output is classified as one of four categories: all/most artifacts removed, some artifacts removed, unchanged image quality and a

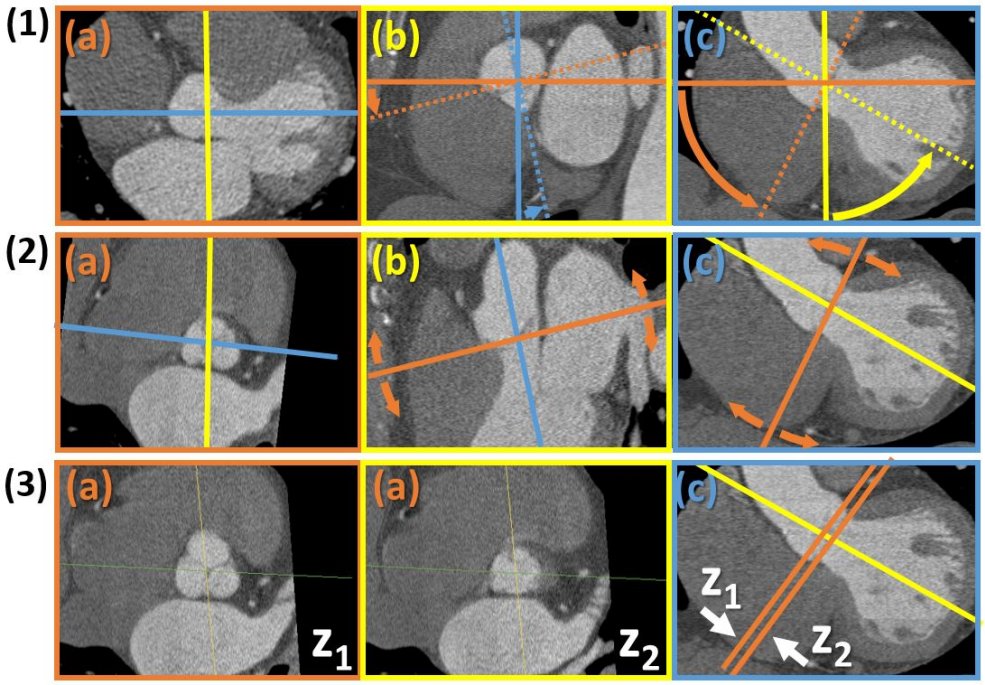

Figure 3.8: Illustration of the steps performed to acquire the AV plane. **(a)** Short-axis views, starting with the axial view. **(b)** Long-axis side views, starting with the sagittal view. **(c)** Long-axis frontal views, starting with the coronal view. The position of one view/slice is marked in the others. $C = 200$ HU, $W = 1200$ HU. **(1)** The slices are centered at the AV and are tilted to align with the long axis of the aortic root. **(2)** The tilted axial slice is shifted along the aortic root long axis to the AV base and its orientation is adjusted such that it intersects with all three AV hinge points, therefore acquiring the AV plane. **(3)** The AV plane is shifted along the aortic root long axis to determine two positions z_1 and z_2 at the AV center and at the AV base.

degraded image. In addition to using clinical data sets, scans of a (moving) AV phantom were evaluated. There was no synchronization of the scan with the motion, causing the position of the AV phantom to vary not only in the final reconstruction, but also in individual stacks. In order to reliably compare the results to the ground truth, the latter was artificially shifted along the z-axis to minimize the RMSE to individual stacks, before extracting equivalent image slices and computing difference images.

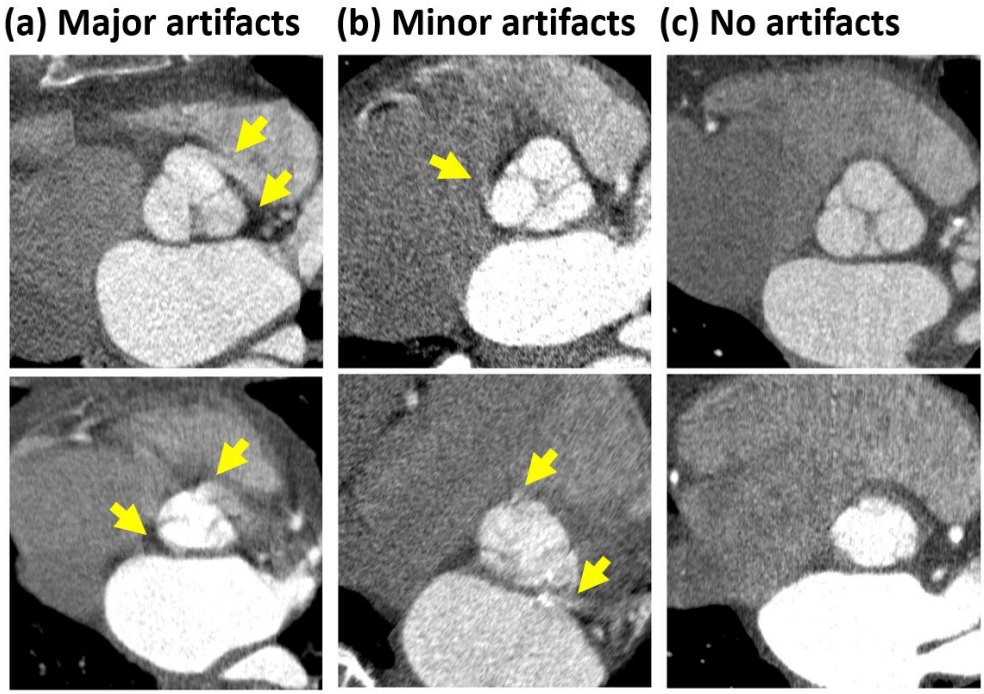

Figure 3.9: CT image slices parallel to the AV plane with artifacts classified as one of three categories: **(a)** Major motion artifacts. **(b)** Minor motion artifacts. **(c)** No motion artifacts. The artifact locations are marked. Each slice originates from a different data set. C = 200 HU; W = 1200–1500 HU;

4 Materials

Twenty four clinical cardiac CT data sets were used in this work. The data originated from various clinics, were cleared for the use in research and finally provided by Siemens Healthineers (cases 1-5; 7-21;) and Prof. Dr. Michael Lell of the Klinikum Nuernberg (cases 28-30; 56;). The majority of the data were retrospectively gated spiral scans acquired at a Somatom AS+ CT scanner (Siemens Healthineers, Forchheim, Germany). Further details can be found in table 4.1. The rotation times were 280 ms except for one Somatom AS data set (330 ms). The data sets 10 and 56 were used for simulations and the therefrom generated synthetic data is labeled S1 and S2. Phantom measurements were performed at a Somatom CounT at the German Cancer Research Center. The respective data is labeled P1 to P6 for scans with motion and PA to PD for scans without motion. The used reconstruction software was ReconCT (Siemens Healthineers). In addition to WFBP, a motion-compensated reconstruction for the coronary arteries (PAMoCo) [26] was used. Furthermore, parts of the utelized software (outside ReconCT) were provided by RayConStruct® GmbH, Nürnberg. The hardware used for all computations was an Asus Notebook Model G752VY with an Intel Core i7-6700HQ CPU and a Nvidia Geforce GTX 980M GPU.

Case	Scanner	Acquisition	Tube voltage	eff. mAs	Heart rate	Pitch	Table increment
1	AS+	spiral	120 kV	143 mAs	68 bpm	0.23	
2	AS+	spiral	80 kV	103 mAs	69 bpm	0.22	
3	AS+	spiral	80 kV	103 mAs	66 bpm	0.20	
4	AS+	spiral	100 kV	92 mAs	65 bpm	0.21	
5	AS+	spiral	100 kV	104 mAs	62 bpm	0.20	
7	AS+	spiral	100 kV	92 mAs	60 bpm	0.23	
8	AS+	spiral	80 kV	105 mAs	55 bpm	0.21	
9	AS+	spiral	120 kV	144 mAs	80 bpm	0.27	
10	AS+	spiral	100 kV	119 mAs	72 bpm	0.24	
11	AS+	spiral	80 kV	104 mAs	59 bpm	0.21	
12	AS+	spiral	100 kV	93 mAs	82 bpm	0.17	
13	AS+	spiral	100 kV	88 mAs	75 bpm	0.22	
14	AS+	spiral	100 kV	125 mAs	64 bpm	0.17	
15	AS+	spiral	80 kV	110 mAs	75 bpm	0.25	
16	AS+	spiral	100 kV	110 mAs	70 bpm	0.17	
17	AS+	spiral	100 kV	110 mAs	74 bpm	0.17	
18	AS+	spiral	80 kV	61 mAs	70 bpm	0.23	
19	AS+	spiral	100 kV	106 mAs	71 bpm	0.26	
20	AS+	spiral	80 kV	98 mAs	51 bpm	0.21	
21	AS+	spiral	100 kV	83 mAs	63 bpm	0.22	
28	Force	sequence	70 kV	323 mAs	63 bpm		37 mm
29	Force	sequence	70 kV	276 mAs	80 bpm		42 mm
30	Force	sequence	110 kV	216 mAs	61 bpm		47 mm
56	AS	spiral	80 kV	566 mAs	79 bpm	0.30	

Table 4.1: Patient data overview. For Sequence scans mAs is given instead of the eff. mAs.

5 Results

The following sections include results for STAR, and the valve MoCo. The two methods are reviewed individually in the following two sections. Finally, a joint use is reviewed. The herein discussed results for STAR have been previously published in [131]. The results for the valve MoCo are partially included in a manuscript currently under consideration for publication.

5.1 Stack Transition Artifact Removal

Numerical results for STAR are displayed in table 5.1. That includes the smoothing parameters and maximum computed deformation vectors. Furthermore, each registration, i.e. each overlap/stack transition, is evaluated individually using the RMSE between the stack overlaps and the image entropy of the difference image at the stack transition, as well as the mean difference image entropy for the whole volume. The registration results are first sorted by case and second by the position of the stack transition within the respective patient volume.
Images are displayed for different cases. Figures 5.1 and 5.2 display results along with the original data for cases 4 and 7. Case 7 shows stronger displacements, larger smoothing parameters are automatically selected and a larger MVF is computed. Image quality is improved considerably in both cases. Some artifacts remain for case 4.
Figures 5.3 and 5.4 displays axial images for cases 4 and 7 along with difference images from the overlapping stacks. The strong displacement of the aortic valve for case 7 is obvious in the difference image. The differences are clearly reduced using STAR. No distortions such as stretching or tearing were introduced into the results. Apart from the removal of the stack transition artifacts, image quality appears to be virtually unchanged. Figure 5.5 displays results for case 14. This case includes strong stack transition artifacts, similar to case 7. Most artifacts were removed by STAR. Figure 5.6. displays axial images and exemplifies when a correction might be neither achieved nor desired. The shape of the ventricle and/or the distribution of the contrast agent varies strongly between the stacks and would require strong deformations of considerable magnitude compared to the ventricle size and strong local MVF gradients, that are not performed given the selected smoothing parameter. The stack difference at the ventricle is reduced but not to the same extent as for some other structures. While figure 5.5 includes some corrected artifacts in the lung, the axial images in figure 5.6 barely show any improvement in the lung for this particular stack pair. Figures 5.7

Case &	$\sigma_{\text{ad.}}$	MVF_{max}	RMSE [HU]			E			
stack number	[mm]	[mm]	Initial	STAR	Δ_{RMSE}	Mean	Initial	STAR	Δ_{E}
2.1	2.4	3.1	112± 1	93± 1	19± 1	5.69	6.09±0.07	5.95±0.11	0.14±0.13
2.2	2.0	2.5	109± 2	84± 1	25± 2	5.69	6.06±0.07	5.82±0.11	0.24±0.13
4.1	3.6	2.5	187± 5	123± 3	64± 5	5.91	6.48±0.06	6.12±0.07	0.36±0.09
4.2	2.6	3.2	165± 5	121± 2	44± 5	5.91	6.41±0.06	6.16±0.07	0.25±0.09
7.1	4.2	5.5	296± 7	176± 5	120± 9	5.97	6.88±0.13	6.38±0.14	0.50±0.19
7.2	5.0	3.1	255± 7	203± 6	52± 9	5.97	6.73±0.13	6.48±0.14	0.25±0.19
7.3	5.2	6.5	287± 4	148± 2	139± 4	5.97	6.94±0.13	6.34±0.14	0.60±0.19
9.1	2.3	2.2	282±41	190±39	92±57	5.64	6.25±0.08	5.98±0.07	0.27±0.11
9.2	2.8	4.1	159± 6	101± 4	58± 7	5.64	6.26±0.08	5.82±0.07	0.44±0.11
11.1	3.1	3.6	205± 4	145± 3	60± 5	6.10	6.55±0.11	6.27±0.12	0.28±0.16
11.2	2.0	4.5	152± 3	98± 1	54± 3	6.10	6.35±0.11	5.93±0.12	0.42±0.16
12.1	2.3	3.0	202± 3	127± 1	75± 3	6.15	6.66±0.05	6.23±0.06	0.43±0.08
14.1	4.0	5.8	265± 4	153± 1	103± 4	5.95	6.82±0.14	6.38±0.12	0.44±0.18
14.2	3.8	6.7	287± 7	224± 6	63± 9	5.95	6.90±0.14	6.62±0.12	0.28±0.18
16.1	3.1	4.0	167± 3	98± 1	69± 3	5.88	6.37±0.20	5.98±0.18	0.39±0.27
16.2	2.8	4.1	199± 6	116± 4	83± 7	5.88	6.54±0.20	6.14±0.18	0.40±0.27
17.1	2.2	2.8	156± 2	98± 1	58± 2	5.86	6.39±0.09	6.01±0.11	0.38±0.14
17.2	2.2	2.7	157± 1	98± 1	59± 1	5.86	6.35±0.09	5.99±0.11	0.36±0.14
28.1	2.4	4.1	339± 5	254± 5	85± 7	6.09	6.88±0.11	6.58±0.09	0.30±0.14
28.2	3.8	3.4	334± 7	272± 6	62± 9	6.09	6.88±0.11	6.64±0.09	0.24±0.14
29.1	2.8	1.9	361± 7	235± 6	126± 9	6.00	6.89±0.09	6.55±0.07	0.34±0.11
29.2	2.7	2.9	278± 5	200± 4	78± 6	6.00	6.58±0.09	6.33±0.07	0.25±0.11
30.1	3.9	3.7	222± 3	137± 1	85± 3	5.57	6.33±0.10	6.02±0.07	0.31±0.12
30.2	2.5	3.2	200± 2	96± 1	104± 2	5.57	6.06±0.10	5.82±0.07	0.24±0.12
56.1	3.1	2.0	195± 6	149± 5	46± 8	6.08	6.58±0.10	6.30±0.12	0.28±0.12
56.2	2.0	2.3	190± 7	140± 3	50± 8	6.08	6.52±0.10	6.24±0.12	0.28±0.12
56.3	2.6	2.3	189± 3	145± 2	44± 4	6.08	6.56±0.10	6.32±0.12	0.24±0.12
56.4	2.0	2.9	198± 3	145± 2	53± 4	6.08	6.64±0.10	6.34±0.12	0.30±0.12
56.5	3.4	2.1	188± 3	143± 2	45± 4	6.08	6.57±0.10	6.35±0.12	0.22±0.16
56.6	2.8	3.3	208± 2	153± 2	55± 3	6.08	6.66±0.10	6.40±0.12	0.26±0.12
56.7	5.4	1.6	203± 3	165± 3	38± 4	6.08	6.65±0.10	6.47±0.12	0.18±0.12
56.8	2.4	2.9	187± 3	137± 2	50± 4	6.08	6.56±0.10	6.28±0.12	0.28±0.12
56.9	2.2	3.2	157± 2	123± 1	34± 2	6.08	6.45±0.10	6.21±0.12	0.24±0.12

Table 5.1: Numeric results for individual registrations. From left to right: case and stack number, smoothing parameter σ_{adaptive}, maximal deformation vector length MVF_{max}, RMSE between stacks (overlaps) prior to and after STAR with the respective difference Δ_{RMSE}, difference image entropy E for the whole volume (mean value) and at the stack transition prior to and after STAR with the respective difference Δ_{E}.

and 5.8 display results for patients 7, 14, 12 and 16. Coronary arteries were reviewed by extracting curved MPRs. In addition to WFBP, a motion compensated reconstruction aimed at coronary arteries [26] was used for cases 14 and 16. The coronary artery MoCo is referred to as PAMoCo and is not to be confused with the valve MoCo. The stack transition artifacts at the coronary arteries were mostly corrected, where for patient 14 registration performance improved with the use of the motion compensated reconstruction. For patient 16 obvious discontinuities remain. An (almost) perfect match would require changing the diameter of the coronary artery and MVF smoothing intentionally prevents this situation to avoid misrepresenting anatomy. The numeric results in table 5.1 show consistent improvement in terms of the RMSE and the difference image entropy. The difference image entropy was improved by a margin of at least one standard deviation for all registrations. It did not drop to the respective mean value for the volume. Using smoothing parameters in the range 2.0 to 5.4 mm, MVFs with maximal deformation lengths of 1.9 to 6.7 mm were computed. Stronger deformations (e.g. $\mathrm{MVF}_{\max} > 4$ mm) did appear to coincide with stronger changes in difference image entropy (e.g. $\Delta_{\mathrm{E}} > 0.4$), but due to the statistical errors the improvements in entropy can not be conclusively compared to each other. In case of the RMSE, varying noise levels and patterns also make inter patient comparison difficult.
Figures 5.9 and 5.10 display results for patients 14 and 16 with different smoothing parameters. Included are axial ROIs containing a coronary artery. The settings $\sigma = 0.5$ mm, that is used for the initial MVF , and $\sigma = 1.0$ mm result in the best registration performance but distort parts of the volume, most importantly the coronary artery. The latter appears distorted with a reduced diameter. Distorted images are marked with a cross in figure 5.9 and 5.10. Stronger smoothing reduces performance but yields undistorted volumes. Images from the latter are marked with a check mark. A good compromise for a constant parameter for both patients is $\sigma = 4.0$ mm. It negatively affects performance for case 16 compared to the adaptive setting but ensures proper MVF smoothing for case 14. The adaptive parameterization yields the best results overall.

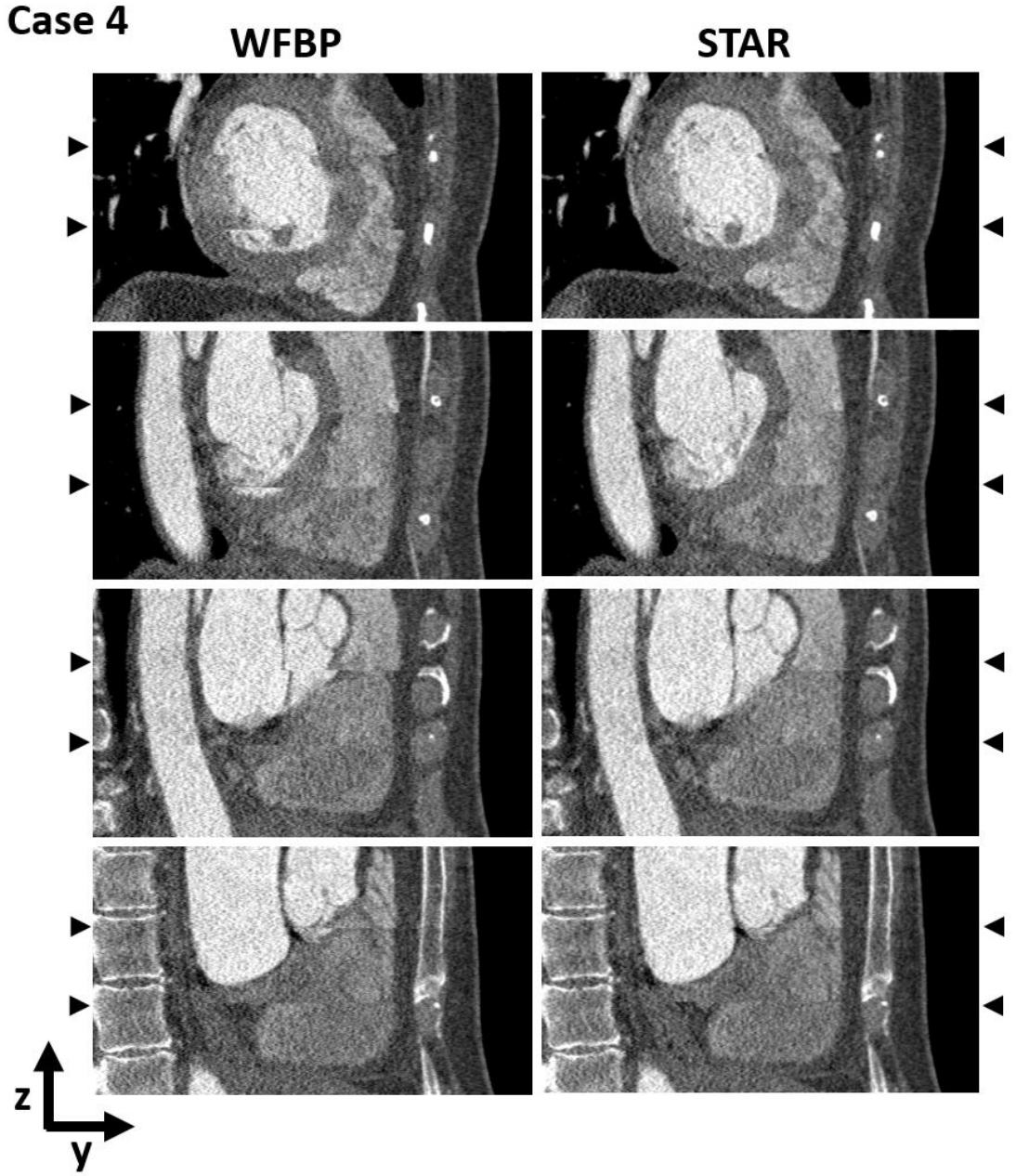

Figure 5.1: Results for case 4. Sagittal slices. Adaptive smoothing parameter $\sigma_{\text{adaptive}} =$ 3.6 mm; 2.6 mm. Stack transitions are marked with triangles. $C = 200$ HU, $W = 1000$ HU.

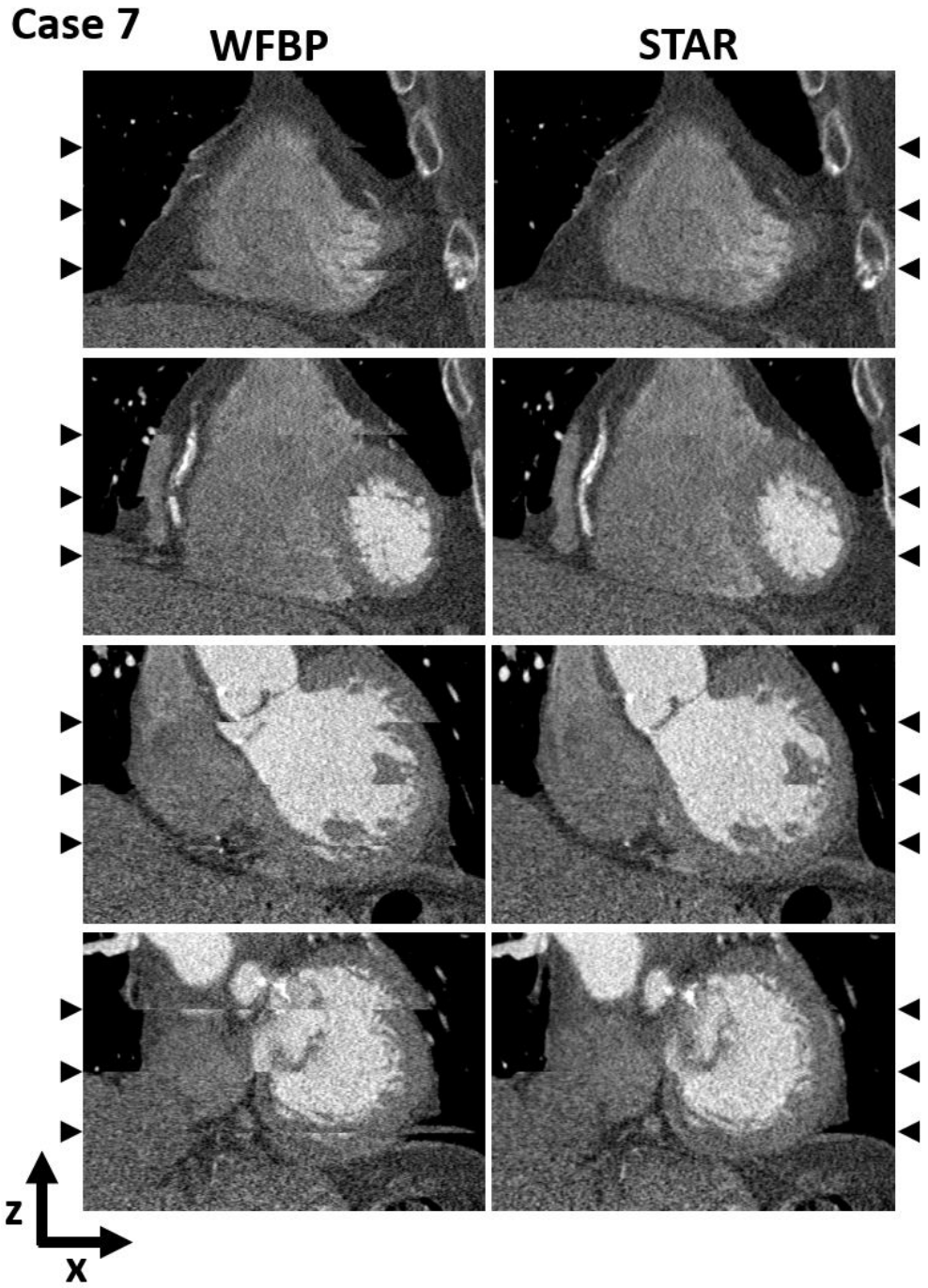

Figure 5.2: Results for case 7. Coronal slices. Adaptive smoothing parameter $\sigma_{\text{adaptive}} = 4.2$ mm; 5.0 mm; 5.2 mm. Stack transitions are marked with triangles. $C = 200$ HU, $W = 1000$ HU.

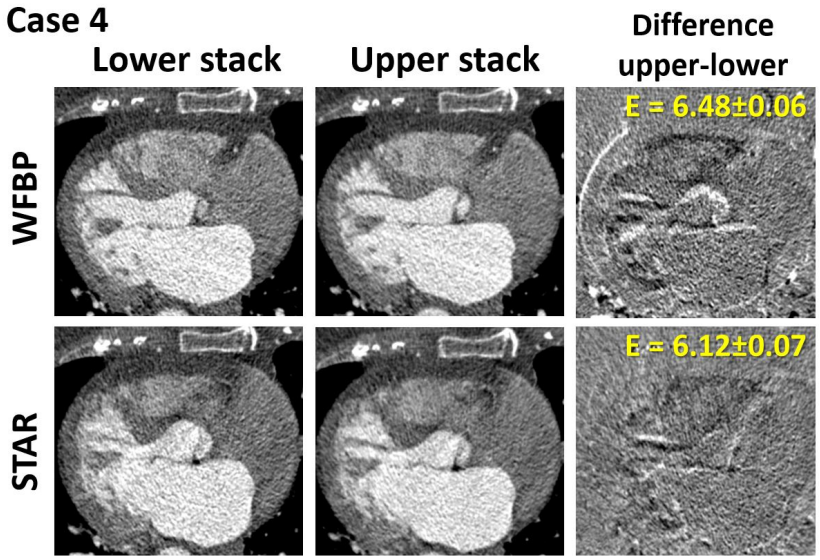

Figure 5.3: Results for case 4. ROI from axial slices. Adaptive smoothing parameter $\sigma_{\text{adaptive}} = 3.6$ mm for the shown stacks. E is the image entropy of the difference images. $C = 200$ HU, $W = 1000$ HU. Difference images: $C = 0$ HU, $W = 1000$ HU.

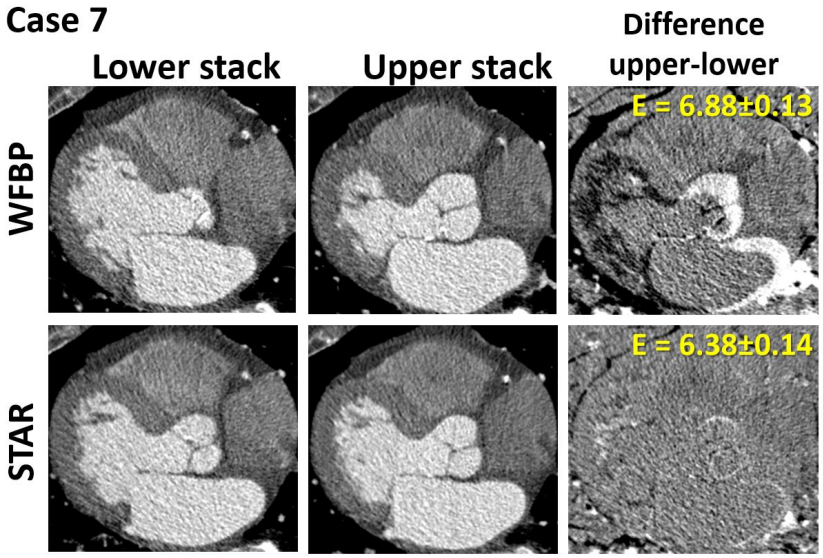

Figure 5.4: Results for case 7. ROI from axial slices. Adaptive smoothing parameter $\sigma_{\text{adaptive}} = 4.2$ mm for the shown stacks. E is the image entropy of the difference images. $C = 200$ HU, $W = 1000$ HU. Difference images: $C = 0$ HU, $W = 1000$ HU.

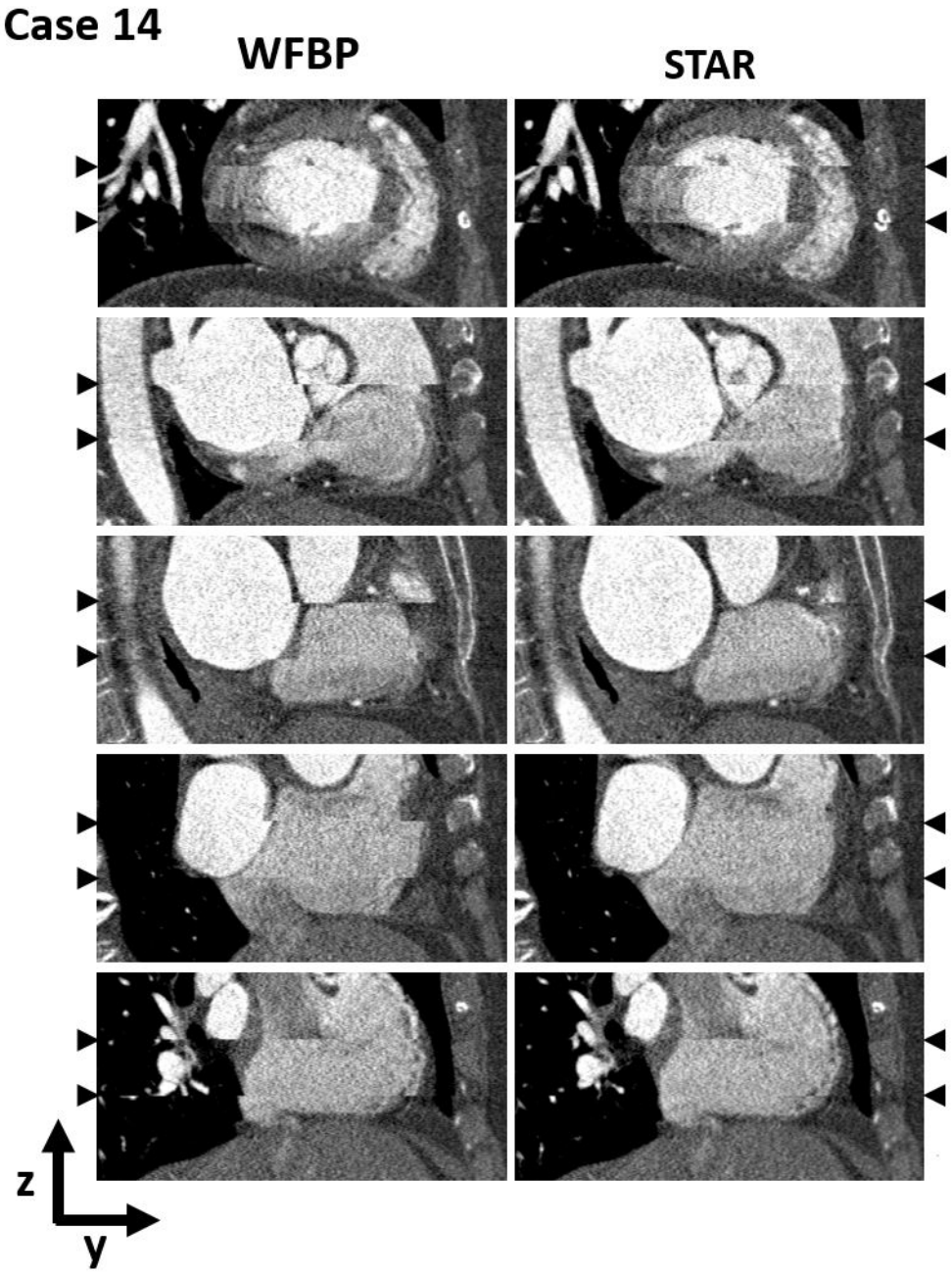

Figure 5.5: Results for case 14. Sagittal slices. Adaptive smoothing parameter $\sigma_{\text{adaptive}} = 4.0$ mm; 3.8 mm. Stack transitions are marked with triangles. $C = 200$ HU, $W = 1000$ HU.

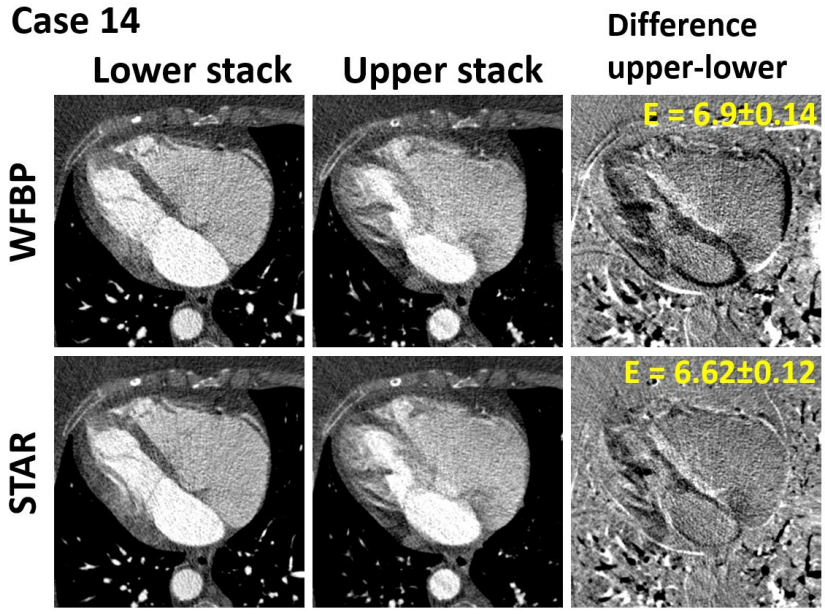

Figure 5.6: Results for case 14. Axial slices. Adaptive smoothing parameter $\sigma_{\text{adaptive}} = 3.8$ mm for the shown stacks. E is the image entropy of the difference images. $C = 200$ HU, $W = 1000$ HU. Difference images: $C = 0$ HU, $W = 1000$ HU.

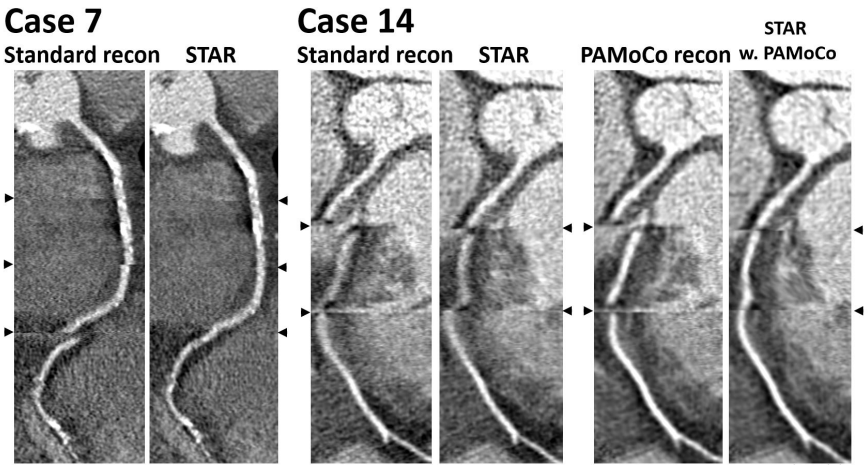

Figure 5.7: Results for cases 7 and 14. Curved MPRs containing the RCA. Adaptive smoothing parameters $\sigma_{\text{adaptive}} = 4.2$ mm; 5.0 mm; 5.2 mm and $\sigma_{\text{adaptive}} = 4.0$ mm; 3.8 mm. Stack transitions marked with triangles. $C = 200$ HU, $W = 1000$ HU.

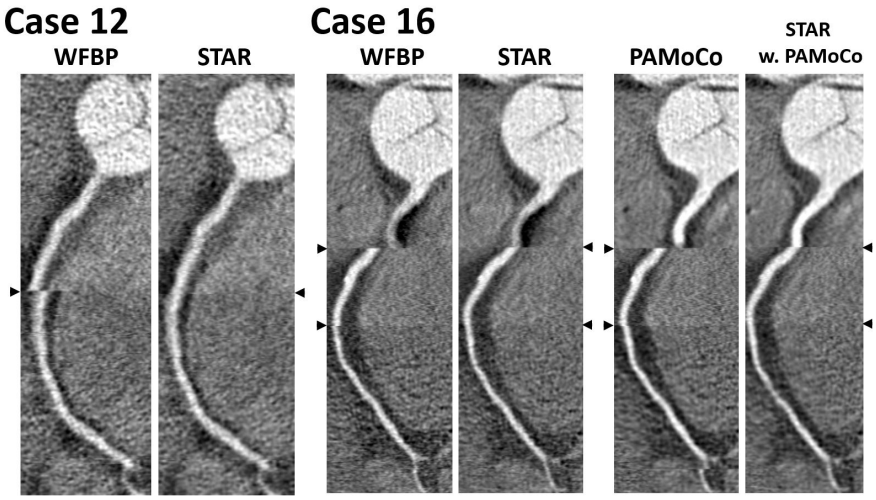

Figure 5.8: Results for cases 12 and 16. Curved MPRs containing the RCA. Adaptive smoothing parameters $\sigma_{\text{adaptive}} = 2.3$ mm and $\sigma_{\text{adaptive}} = 3.1$ mm; 2.8 mm. Stack transitions are marked with triangles. $C = 200$ HU, $W = 1000$ HU.

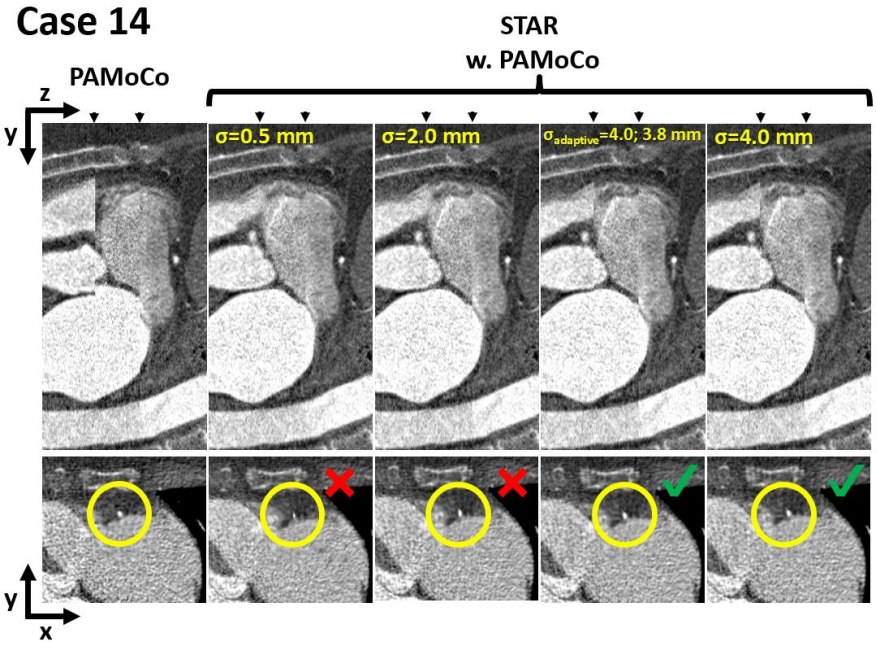

Figure 5.9: Results for case 14 and different smoothing parameters. Sagittal slices. Stack transitions are marked with triangles. Images that are deemed too distorted are marked with a cross. Undistorted images are marked with a check mark. $C = 200$ HU, $W = 1000$ HU.

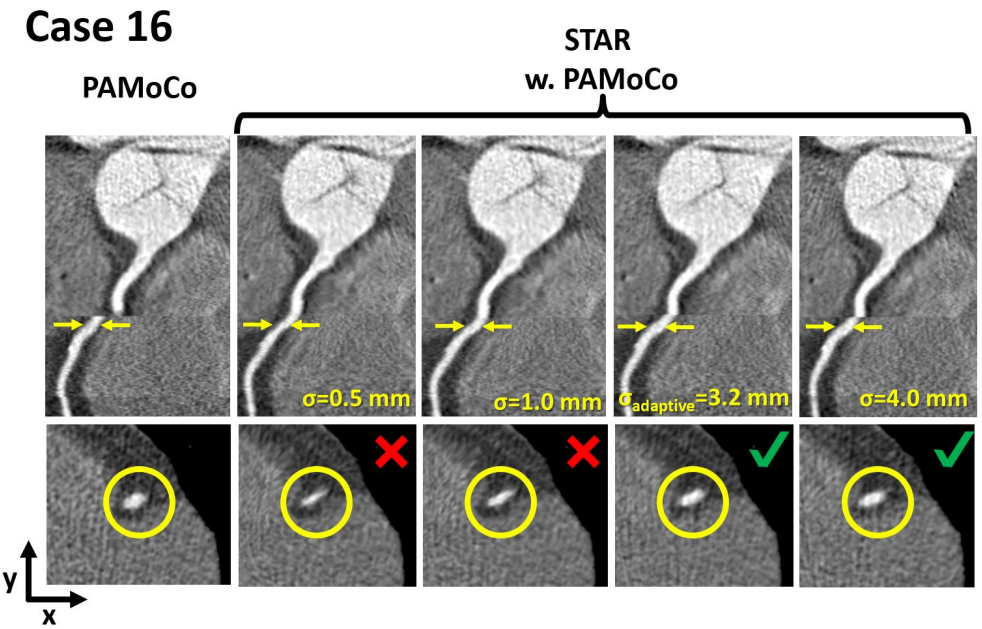

Figure 5.10: Results for case 16 and different smoothing parameters. Curved MPRs containing the RCA. Images that are deemed too distorted are marked with a cross. Undistorted images are marked with a check mark. $C = 200$ HU, $W = 1000$ HU.

Simulation Results

The results from the simulations are summarized in table 5.2. Uniform motion was simulated with different amplitudes and directions. The table includes the MVF error computed as mean amplitude of the difference vector between the computed MVF and the ground truth. In addition, it includes the RMSE between the stacks prior and after STAR. The directions are given using spherical coordinates θ and ϕ. Simulations were performed for polar angles $\theta < 90°$, where gray values are pushed towards the upper/lower stack and overlap boundary or beyond it. In case the MVF is reaching outside of the stack, the closest boundary values are copied. While the same MVFs were simulated for the data sets S1 and S2, both had different overlap sizes 6.3 mm and 4 mm. The data show stronger deviations from the ground truth for larger MVFs, but mostly for larger z-components. For MVF z-components around half the overlap size, the MVF error rose beyond 1 mm. For more extreme cases where more data were pushed out of the overlap, the error increased to multiple mm. Otherwise the error remained well in the range between 0.05 mm and 0.4 mm. The RMSE value was consistently improved in all cases. Figure 5.11 shows results for non-uniform simulated MVFs for cases S1 and S2, including MVF amplitude images. For case S1, the simulated MVF expands/contracts the stacks and can almost entirely be reproduced by STAR. In case S2 the simulated MVF had a constant direction but spatial variations for the amplitude. At a MVF amplitude of 3 mm STAR struggles to reproduce some of the finer features of the MVF ground truth. At $D = 3$ mm and $\theta = 30°$, i.e. a MVF z-component of 65% of the overlap depth, STAR further deviates from the ground truth throughout the image but still resembles the shape given by the ground truth.

Pat.	θ \ D	1 mm	3 mm	6 mm	9 mm
S1	0°	**0.05 mm** **329→57 HU**	**1.8 mm** **265→149 HU**	5.3 mm 319→255 HU	8.3 mm 357→278 HU
	30°	**0.06 mm** **160→66 HU**	**0.37 mm** **255→114 HU**	4.8 mm 309→222 HU	8.2 mm 346→273 HU
	60°	**0.04 mm** **169→53 HU**	**0.16 mm** **301→79 HU**	**2.0 mm** **380→172 HU**	4.0 mm 432→248 HU
	90°	**0.1 mm** **187→53 HU**	**0.11 mm** **329→57 HU**	**0.12 mm** **426→172 HU**	**0.32 mm** **494→116 HU**
S2	90°	**0.08 mm** **199→69 HU**	**0.09 mm** **296→80 HU**	**0.09 mm** **372→88 HU**	**0.09 mm** **428→92 HU**
	60°	**0.05 mm** **188→69 HU**	**1.2 mm** **294→128 HU**	2.8 mm 370→180 HU	4.1 mm 433→208 HU
	30°	**0.2 mm** **188→69 HU**	2.1 mm 294→128 HU	5.0 mm 370→180 HU	7.7 mm 433→208 HU
	0°	**0.19 mm** **157→92 HU**	2.9 mm 234→174 HU	6.3 mm 287→216 HU	8.97 mm 325→265 HU

Table 5.2: Numeric results for the simulations for different directions (θ: polar angle) and amplitudes (D) of a uniform MVF. Included are MVF error in mm and the RMSE between the stacks prior and after STAR. The MVF error is the mean amplitude of the difference vector between the computed MVF and the ground truth. The overlap depths for cases S1 and S2 are 6.3 mm and 4 mm. Results where the z-component of the MVF is smaller than half the overlap depth are highlighted.

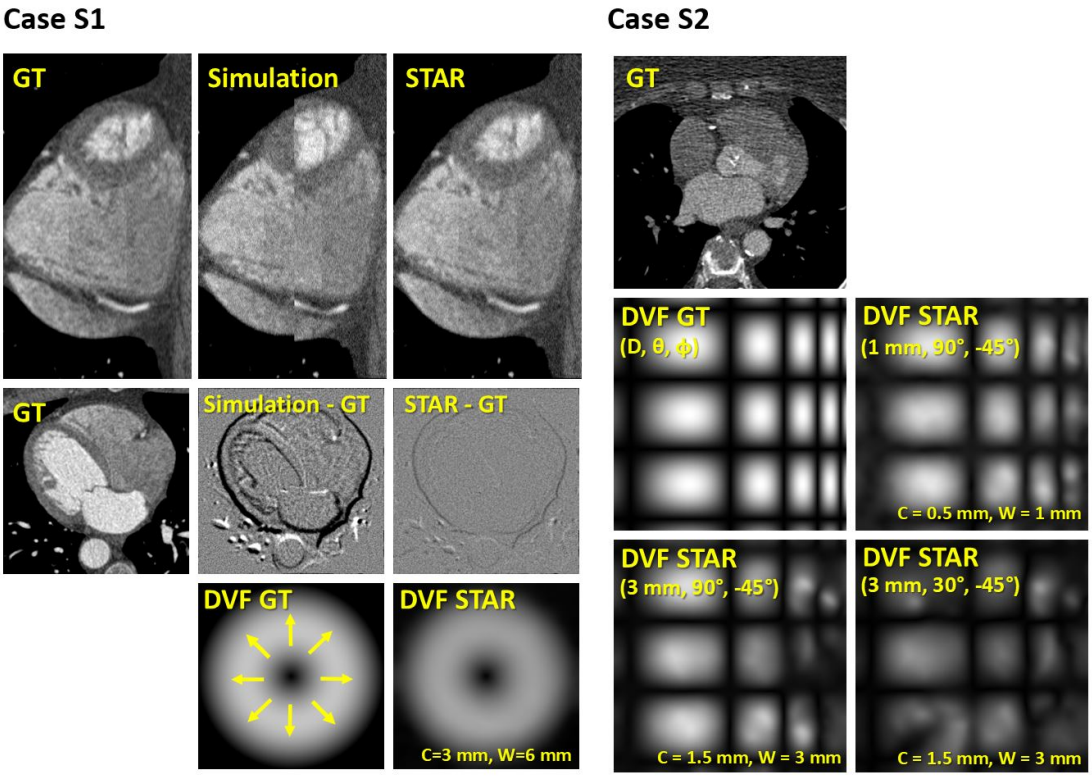

Figure 5.11: Simulation results for STAR. Case S1: Coronal slices from the ground truth (GT), volume with applied simulated motion and result for STAR. Axial slices at stack transition from lower stack for GT, difference images and MVF amplitude images. The varying directions of the GT MVF are illustrated using arrows. Case S2: Axial slices at stack transition from lower stack for GT, MVF GT, and computed MVF for varying MVF directions and amplitudes. D is the max. amplitude. CT–slices: $C = 200$ HU, $W = 1000$ HU. Difference images: $C = 0$ HU, $W = 1000$ HU.

5.2 Partial Angle Reconstruction Based Motion Compensation

For all results, MPRs parallel to the aortic valve plane are displayed. Two slices roughly at the height of the AV and the leaflets, as well as at the height of the valve base are shown. "WFBP" and "MoCo" refer to the original WFBP and the motion-compensated volumes, respectively. Reconstructions were performed at 50% and 70% R-R cardiac phase. Generally, there are considerably more motion artifacts in the 50% than in the 70% images, with the latter serving as a reference to ensure that the motion compensation did not distort the 50% images. Figures 5.12 and 5.13 display results for cases 3 and 10. For the former, the motion artifacts around the AV are mostly removed, while for the latter the artifacts are removed only partially. In both cases, the closed state of the AV does not appear to change between the WFBP and the MoCo image, the shape of the AV remains similar to the 70% reference image and other distortions are not observed. However, a minor stack transition artifact is introduced for case 10, directly at the AV. Figures 5.14 and 5.15 display results for cases 13 and 17. The motion artifacts were particularly strong at the AV for case 13 and could be mostly corrected. Case 17 was artifact-free and while the image quality was largely maintained by the MoCo, a weak blurring was introduced. Figures 5.16 and 5.17 display results for cases 4 and 21, both of which were successfully corrected for motion. For case 4, stack transition artifacts were also removed by the valve MoCo. Results for 19 cases at

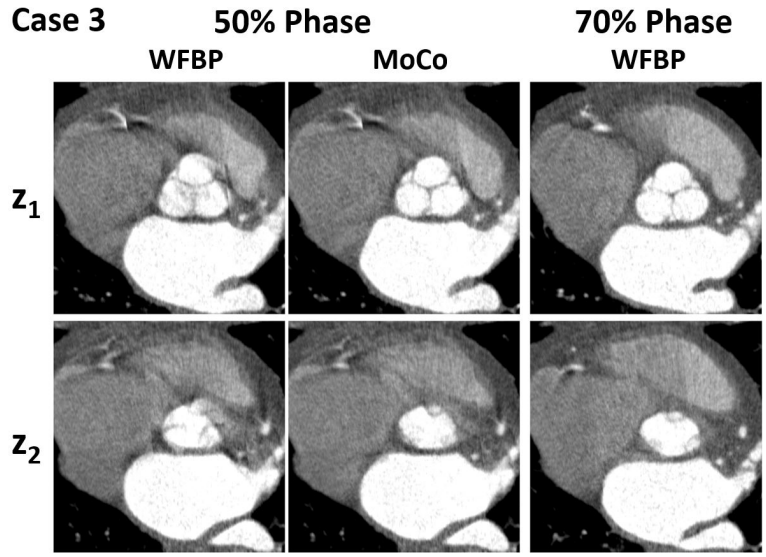

Figure 5.12: Results for Case 3. AV images including the leaflets (z_1) and the base (z_2) at 50% and 70% phase. $C = 200$ HU, $W = 1500$ HU.

50% and 70% can be found in appendix B. In total, 18 of 38 reconstructions showed motion artifacts at the AV. For 16 out of these 18, major image quality improvements and for 1 out of these 18, minor improvements were achieved. For one reconstruction

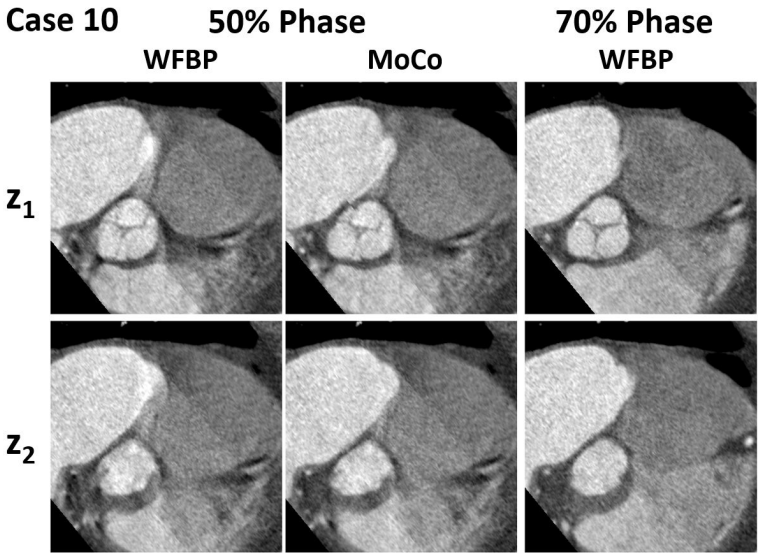

Figure 5.13: Results for Case 10. AV images including the leaflets (z_1) and the base (z_2) at 50% and 70% phase. $C = 200$ HU, $W = 1200$ HU.

with minor artifacts, no improvement was achieved. For the 21 artifact-unimpaired reconstructions the image quality remained largely unchanged. Generally, the possibility for minor blurring by the valve MoCo exists. The results are summarized in table 5.3. The maximum computed velocities in the individual stacks MVFs were in the range of roughly 30 mm/s to 70 mm/s and therefore generally below the reference $V_{\text{ref}} = 70$ mm/s. The maximum gradient metric ratio q_{grad} showed values in the range of 0.5 to 1.5. The gradient reference value $G_{\text{ref}} = 0.15$ was exceeded multiple times, also for reconstructions with no observed motion artifacts. Figures 5.18, 5.19, 5.20 and 5.21 display results for cases 4, 10, 14 and 16, for a joint artifact correction consisting of valve MoCo, first, and STAR, second. Results are also displayed for the valve MoCo alone. The valve MoCo images for the four cases feature minor stack transition artifacts. The joint approach removed most stack artifacts that previously were either partially reduced (cases 4, 16), enhanced (case 14) or introduced (case10) by valve MoCo. Some stack artifacts remain and the images for the joint approach in cases 4 and 14 are slightly displaced in orthogonal direction to the image plane. Figures 5.22 and 5.23 display results for the joint artifact correction for cases 4 and 13 in 3-chamber view. Motion artifacts at and around the AV and stack transition artifacts were reduced in accordance with the previous results.

Case	c	Stack number	q_{vel}	q_{grad}	Artifacts	Change
1	70%	1	0.41	0.88	++	++
		2	0.50	1.00		
		3	0.57	1.04		
	50%	1	0.43	0.99	++	++
		2	0.78	1.15		
		3	0.61	1.22		
2	70%	1	0.67	1.35	0	0
		2	0.24	0.64		
		3	0.51	1.17		
	50%	1	0.52	1.02	+	+
		2	0.54	1.11		
		3	0.89	1.26		
3	70%	1	0.27	0.64	0	0
		2	0.31	0.56		
		3	0.37	0.79		
		4	0.54	1.05		
	50%	1	0.29	0.80	++	++
		2	0.53	0.99		
		3	0.92	1.46		
		4	0.72	1.22		
4	70%	1	0.37	0.92	0	0
		2	0.72	1.20		
		3	0.84	1.27		
		4	0.60	1.21		
	50%	1	0.90	1.23	++	++
		2	0.49	1.23		
		3	0.49	1.23		
		4	0.74	1.26		
5	70%	1	0.24	0.47	0	0
		2	0.31	0.74		
		3	0.51	0.85		
		4	0.56	1.22		
		5	0.64	1.34		
	50%	1	0.46	0.81	++	++
		2	0.68	1.01		
		3	0.95	1.30		
		4	0.84	1.35		
7	70%	1	0.43	0.92	0	0
		2	0.58	1.09		
		3	0.52	1.00		
		4	0.39	0.75		
	50%	1	0.91	1.11	+	++
		2	0.80	1.28		
		3	0.80	1.31		
8	70%	1	0.31	0.96	+	++
		2	0.48	1.08		
		3	0.42	0.89		
	50%	1	0.44	0.72	0	0
		2	0.45	1.28		
		3	0.52	0.91		
9	70%	1	0.31	0.92	0	0
	50%	1	0.38	0.88	0	0
		2	0.54	1.25		
10	70%	1	0.52	1.19	0	0
		2	0.45	1.01		
	50%	1	0.51	1.33	++	+
		2	0.68	1.16		
11	70%	1	0.42	0.98	0	0
		2	0.51	1.10		
	50%	1	0.50	1.01	+	+
		2	0.88	1.12		
		3	0.88	1.30		
13	70%	1	0.41	0.75	0	0
		2	0.65	1.15		
		3	0.47	0.92		
		4	0.67	1.38		
	50%	1	0.50	0.88	++	++
		2	0.83	0.87		
		3	0.72	1.22		
		4	1.04	1.28		
14	70%	1	0.34	0.63	0	0
		2	0.51	1.17		
		3	0.63	1.01		
		4	0.82	1.39		
		5	0.52	1.10		
	50%	1	0.47	0.95	+	0
		2	0.71	1.30		
		3	0.60	1.18		
		4	0.89	1.27		
		5	0.64	1.16		
15	70%	1	0.36	0.74	0	0
		2	0.64	1.15		
		3	0.45	0.94		
	50%	1	0.46	0.92	++	++
		2	0.87	1.39		
		3	1.08	1.39		
16	70%	1	0.37	0.49	+	++
		2	0.40	0.67		
		3	0.91	0.95		
		4	0.60	1.00		
		5	0.68	1.26		
	50%	1	0.31	0.74	+	++
		2	0.95	1.08		
		3	0.51	1.03		
		4	0.69	1.31		
		5	0.61	1.20		
17	70%	1	0.39	1.04	0	0
		2	0.55	1.04		
		3	0.66	1.35		
		4	0.51	0.89		
	50%	1	0.54	1.15	0	0
		2	0.80	1.42		
		3	0.49	0.89		
18	70%	1	0.22	0.73	0	0
		2	0.29	0.82		
		3	0.44	1.33		
		4	0.59	1.32		
	50%	1	0.30	0.71	+	++
		2	0.45	0.95		
		3	0.75	1.19		
		4	0.91	1.41		
19	70%	1	0.41	0.75	0	0
		2	0.86	1.21		
		3	0.44	1.15		
	50%	1	0.44	0.99	+	+
		2	0.66	1.32		
		3	0.77	1.35		
20	70%	1	0.31	0.66	0	0
		2	0.37	0.98		
		3	0.52	1.17		
	50%	1	0.29	0.70	0	0
		2	0.48	0.98		
		3	0.62	1.21		
21	70%	1	0.38	0.84	0	0
		2	0.78	1.14		
		3	0.88	1.33		
	50%	1	0.40	0.94	++	++
		2	0.79	1.29		
		3	0.82	1.21		

Table 5.3: Valve MoCo results. The ratios $q_{E/\text{vel/grad}}$ are given for individual stacks. The artifact evaluation is done for the entire CT volume. The artifact magnitude is represented with ++ (strong artifacts), + (minor artifacts) or 0 (no artifacts). The change of image quality is represented with ++ (major improvement), + (minor improvement) or 0 (no change).

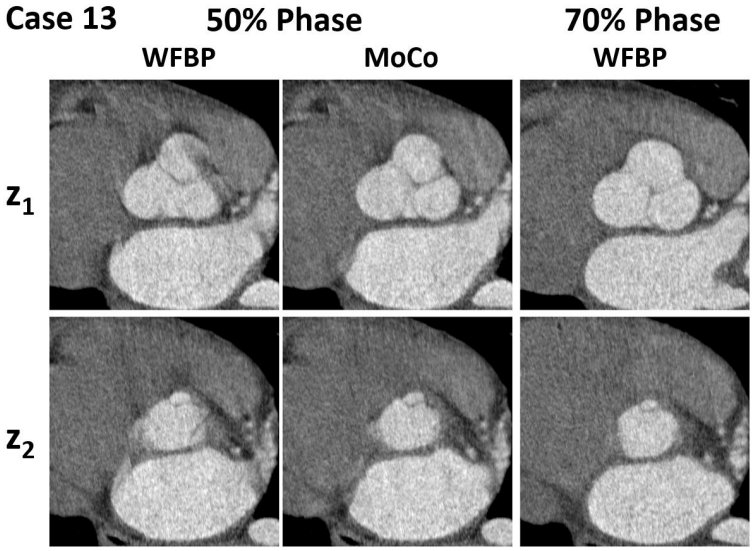

Figure 5.14: Results for Case 13. AV images including the leaflets (z_1) and the base (z_2) at 50% and 70% phase. $C = 200$ HU, $W = 1200$ HU.

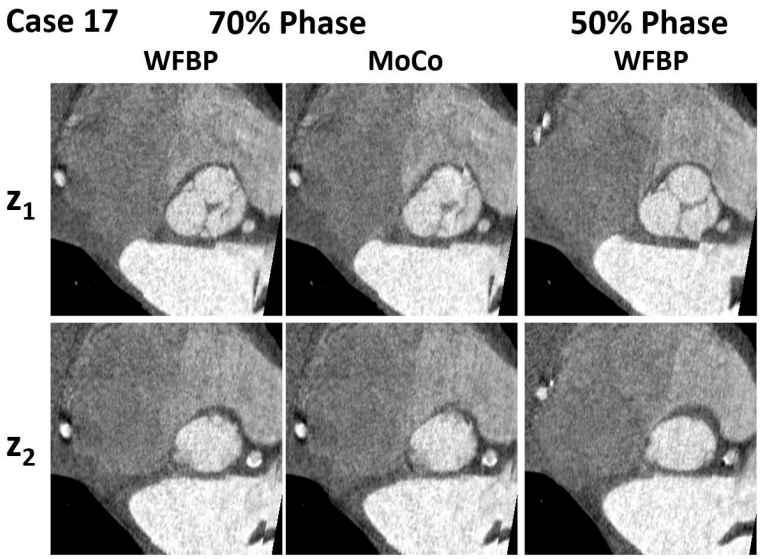

Figure 5.15: Results for Case 17. AV images including the leaflets (z_1) and the base (z_2) at 50% and 70% phase. $C = 200$ HU, $W = 1200$ HU.

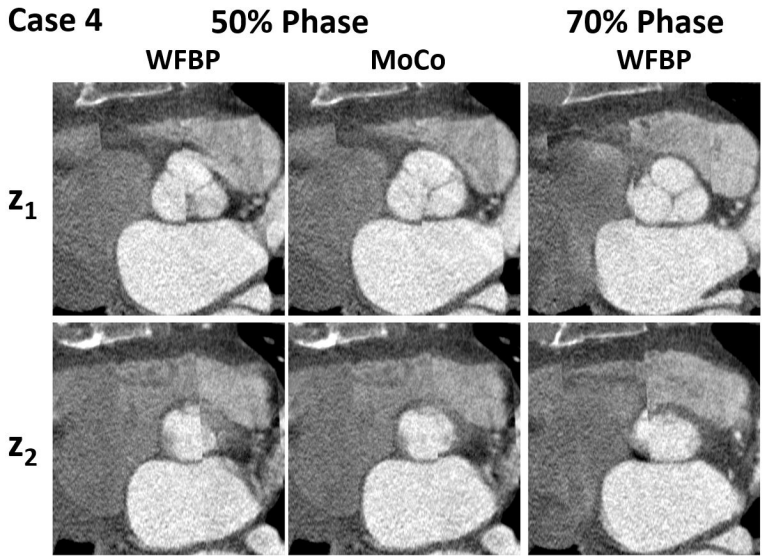

Figure 5.16: Results for Case 4. AV images including the leaflets (z_1) and the base (z_2) at 50% and 70% phase. $C = 200$ HU, $W = 1200$ HU.

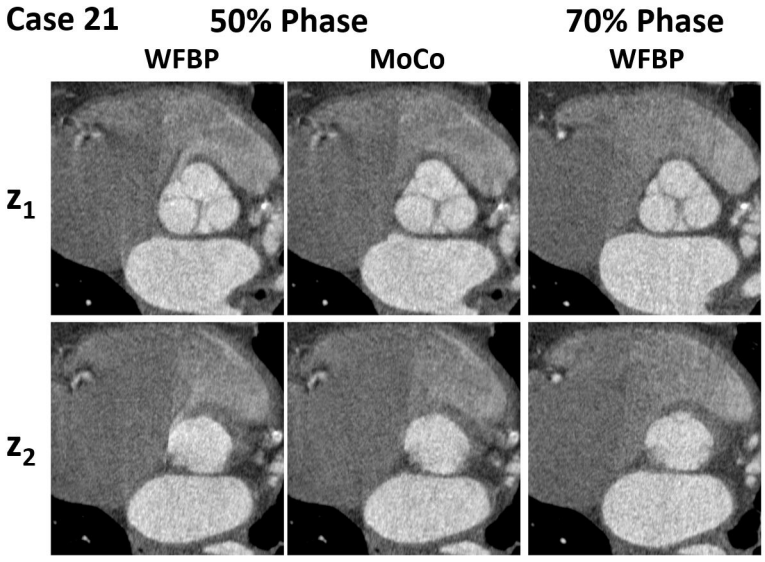

Figure 5.17: Results for Case 21. AV images including the leaflets (z_1) and the base (z_2) at 50% and 70% phase. $C = 200$ HU, $W = 1200$ HU.

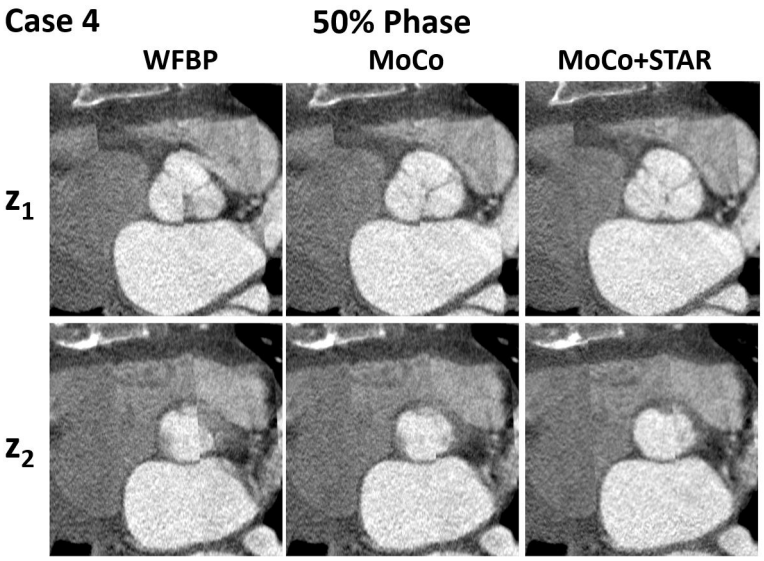

Figure 5.18: Combined valve MoCo and STAR results. Case 4. AV images including the leaflets (z_1) and the base (z_2) at 50% phase. $C = 200$ HU, $W = 1200$ HU.

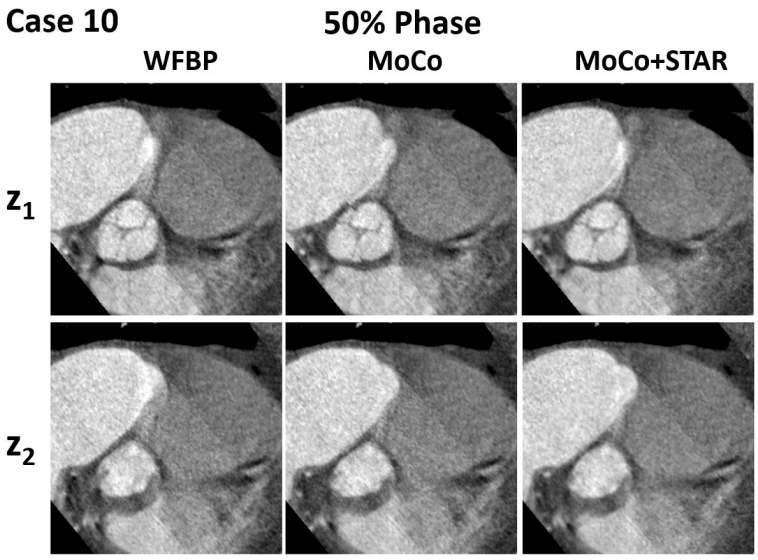

Figure 5.19: Combined valve MoCo and STAR results. Case 10. AV images including the leaflets (z_1) and the base (z_2) at 50% phase. $C = 200$ HU, $W = 1200$ HU.

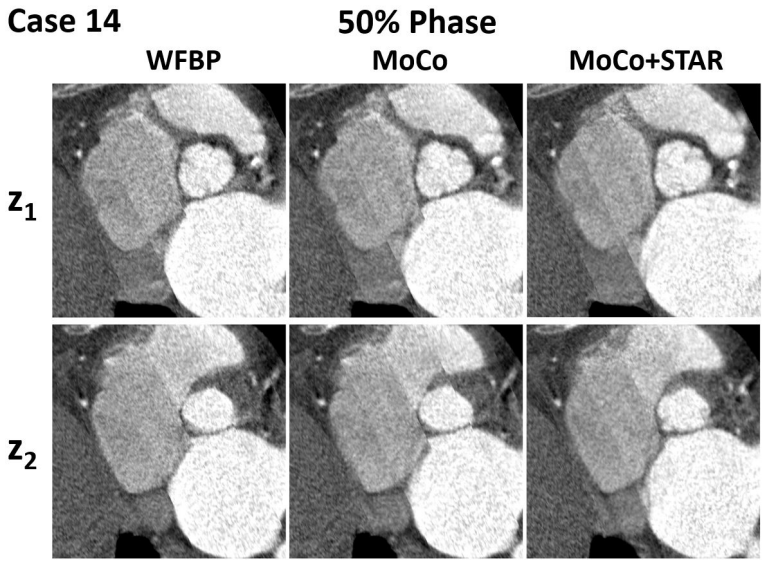

Figure 5.20: Combined valve MoCo and STAR results. Case 14. AV images including the leaflets (z_1) and the base (z_2) at 50% phase. $C = 200$ HU, $W = 1200$ HU.

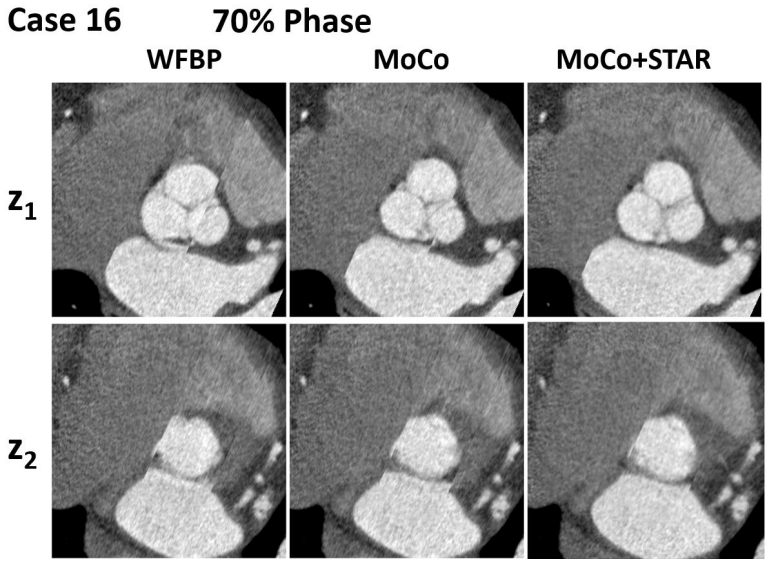

Figure 5.21: Combined valve MoCo and STAR results. Case 16. AV images including the leaflets (z_1) and the base (z_2) at 50% phase. $C = 200$ HU, $W = 1200$ HU.

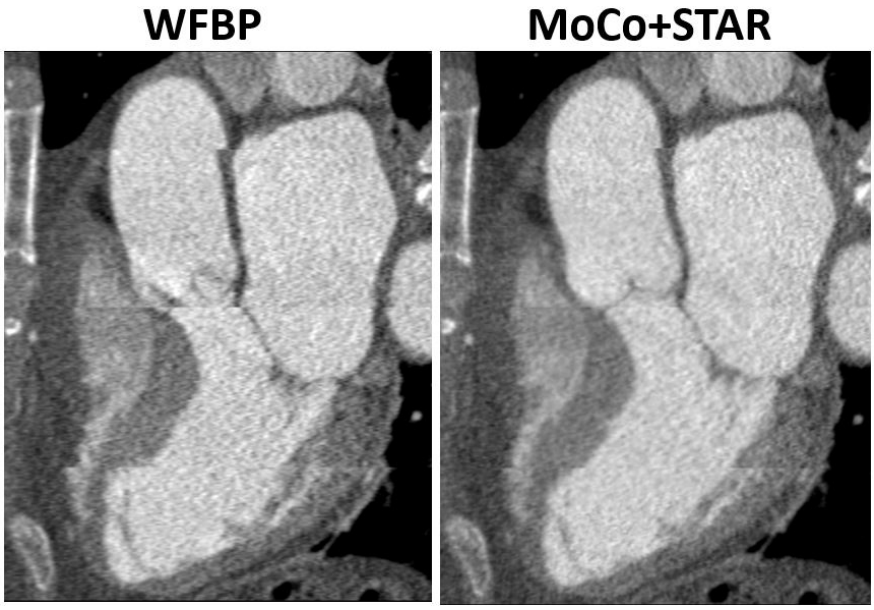

Figure 5.22: Combined valve MoCo and STAR results for case 4 at 50% phase. 3-chamber view. $C = 200$ HU, $W = 1200$ HU.

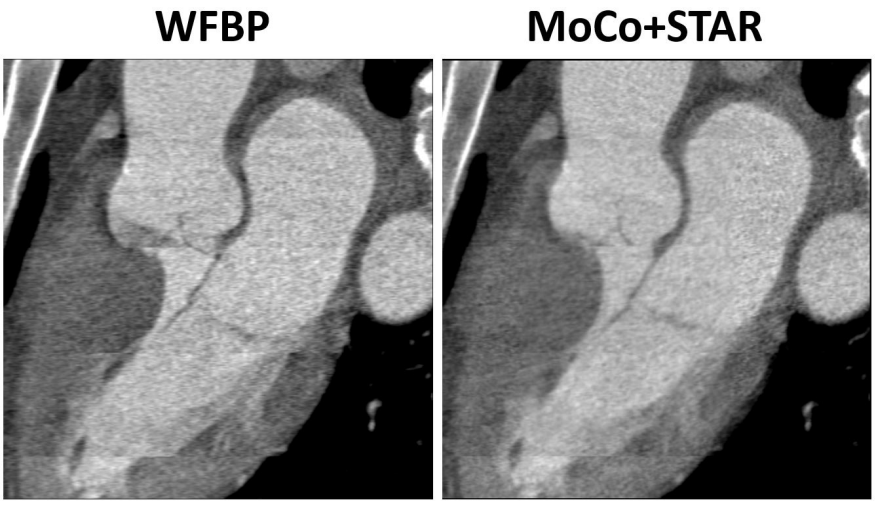

Figure 5.23: Combined valve MoCo and STAR results for case 13 at 50% phase. 3-chamber view. $C = 200$ HU, $W = 1200$ HU.

Phantom Measurement Results

The valve MoCo was applied to phantom measurements as well. Figure 5.24 displays slices from a reconstruction of the motion-free phantom ground truth image and the result after applying valve MoCo to this data set. While the image quality remains mostly unchanged, minor blurring and minor stack transition artifacts are introduced by the MoCo. Motion impaired phantom data was labeled P1 to P6. It was found that $G_{\text{ref}} = 0.4$ is required for the best performance with the phantom data. Figure 5.25 displays results for $G_{\text{ref}} = 0.15$ and $G_{\text{ref}} = 0.4$ along with the WFBP and a ground truth image. Only partial image quality improvement is achieved, even with the higher G_{ref}-setting. Stack transition artifacts can be observed as well. $G_{\text{ref}} = 0.4$ has been used for all other phantom data reconstructions, including in figure 5.24. Figures 5.26,

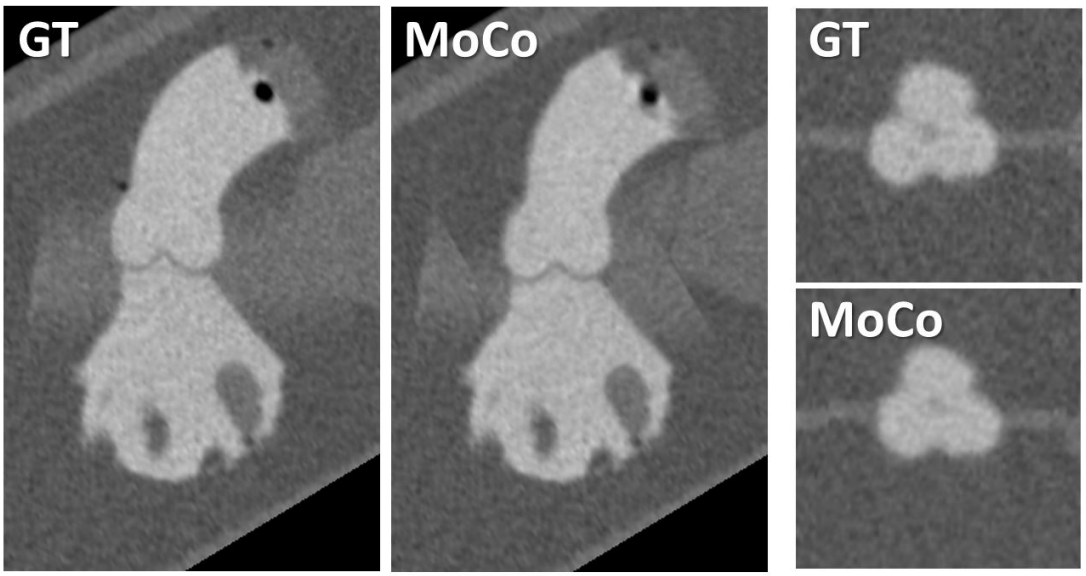

Figure 5.24: Slices from the motion-free reconstruction (case PA) of the AV phantom and valve MoCo images. $C = 200$ HU, $W = 1200$ HU.

5.27 and 5.28 display results for the phantom measurement cases P1 to P6 at the AV. Difference images with respect to the ground truth are included. While image quality is generally improved, especially at the leaflets ($z1$), the ground truth image quality was not achieved for any case. For case P4, image quality was slightly degraded. Even with motion artifacts removed, the difference images continue to show distinct features, indicating that the edges in the motion compensated images do not exactly align with the ground truth. It was observed, that the most improvements for the phantom data are observed along the aorta and not at the AV. Figure 5.29 displays examples from case P6. Table 5.4 includes numerical results for valve MoCo applied to the phantom data. Four motion-free data sets are included and labeled PA to PD. Valve MoCo computes MVFs with considerable velocity and gradient ratios q_{vel} and q_{grad}, also for the motion-free cases. For most of the phantom data cases, the gradient reference value

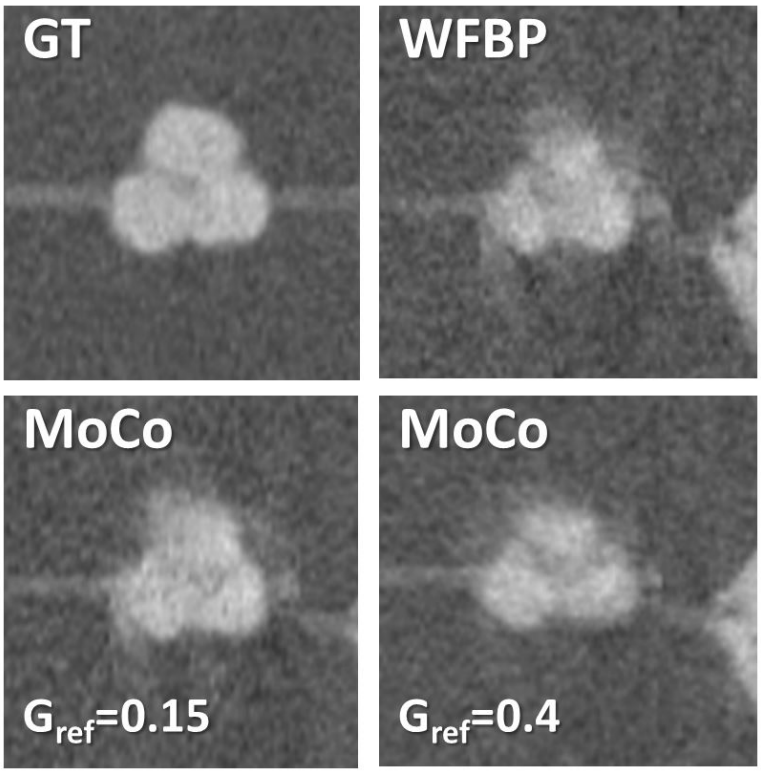

Figure 5.25: Phantom measurement results. Case P1. Results for two valve MoCo settings $G_{\text{ref}} = 0.15$ and $G_{\text{ref}} = 0.4$. $C = 200$ HU, $W = 1200$ HU.

G_{ref} is exceeded. Furthermore, the computed maximum velocity exceeds the phantoms maximum velocity $v_{\max}$ in most cases.

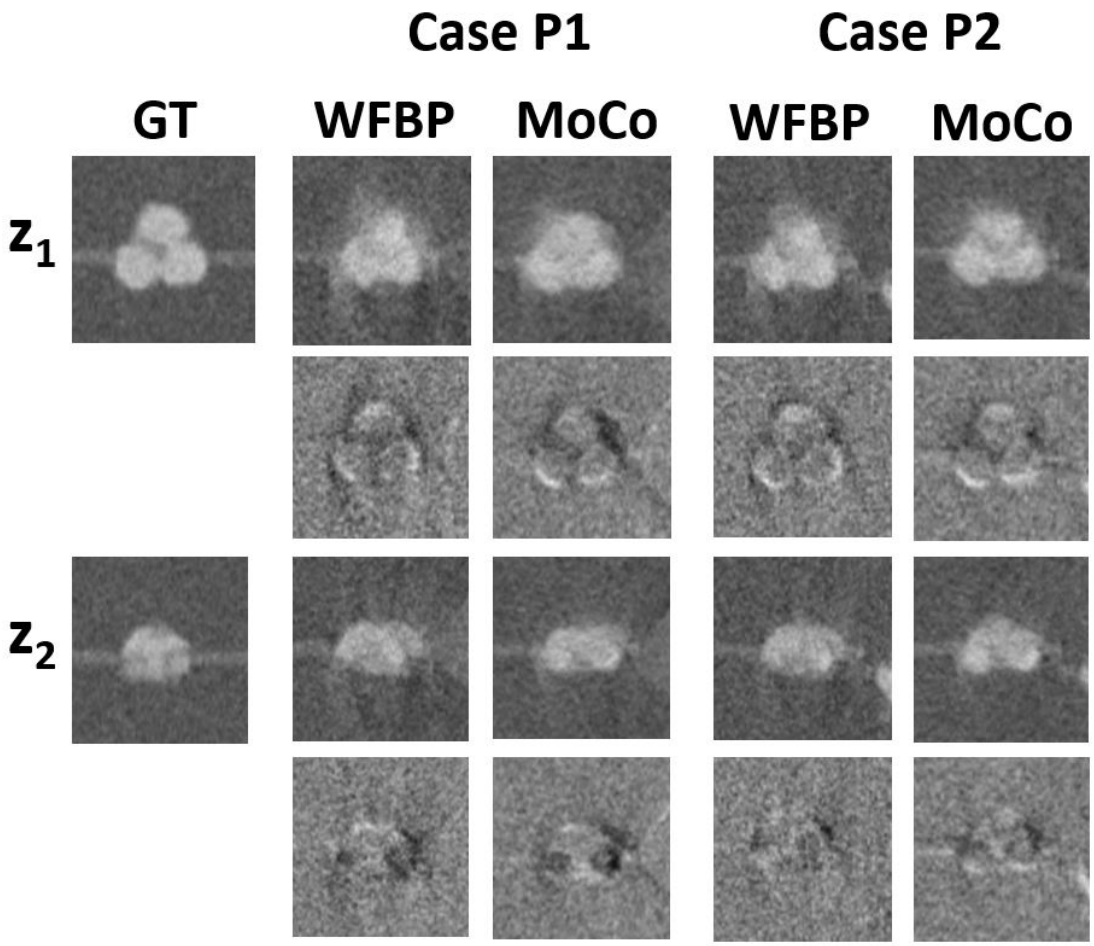

Figure 5.26: Phantom measurement results. Cases P1 and P2. AV images including the leaflets (z_1) and the base (z_2). Ground truth (GT) and difference images with respect to the ground truth are included. $C = 200$ HU, $W = 1200$ HU.

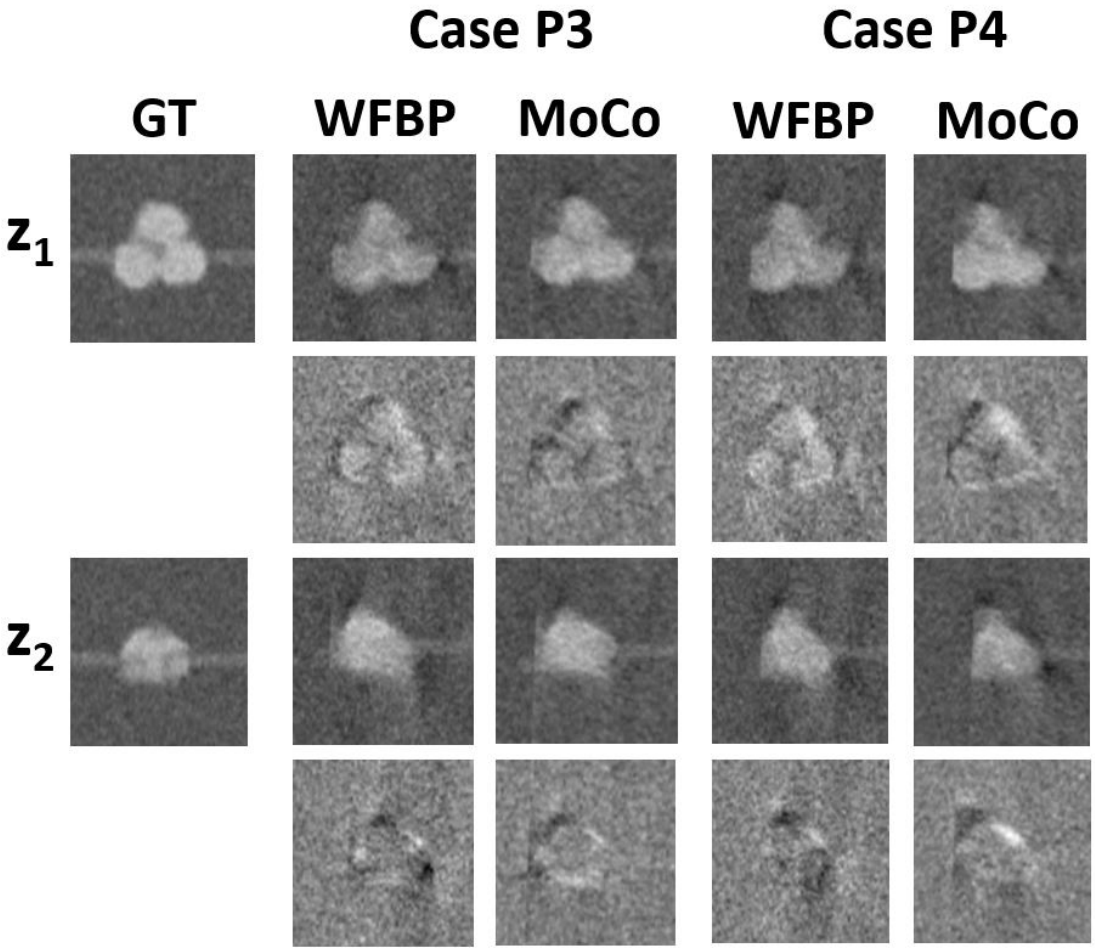

Figure 5.27: Phantom measurement results. Cases P3 and P4. AV images including the leaflets (z_1) and the base (z_2). Ground truth (GT) and difference images with respect to the GT are included. $C = 200$ HU, $W = 1200$ HU.

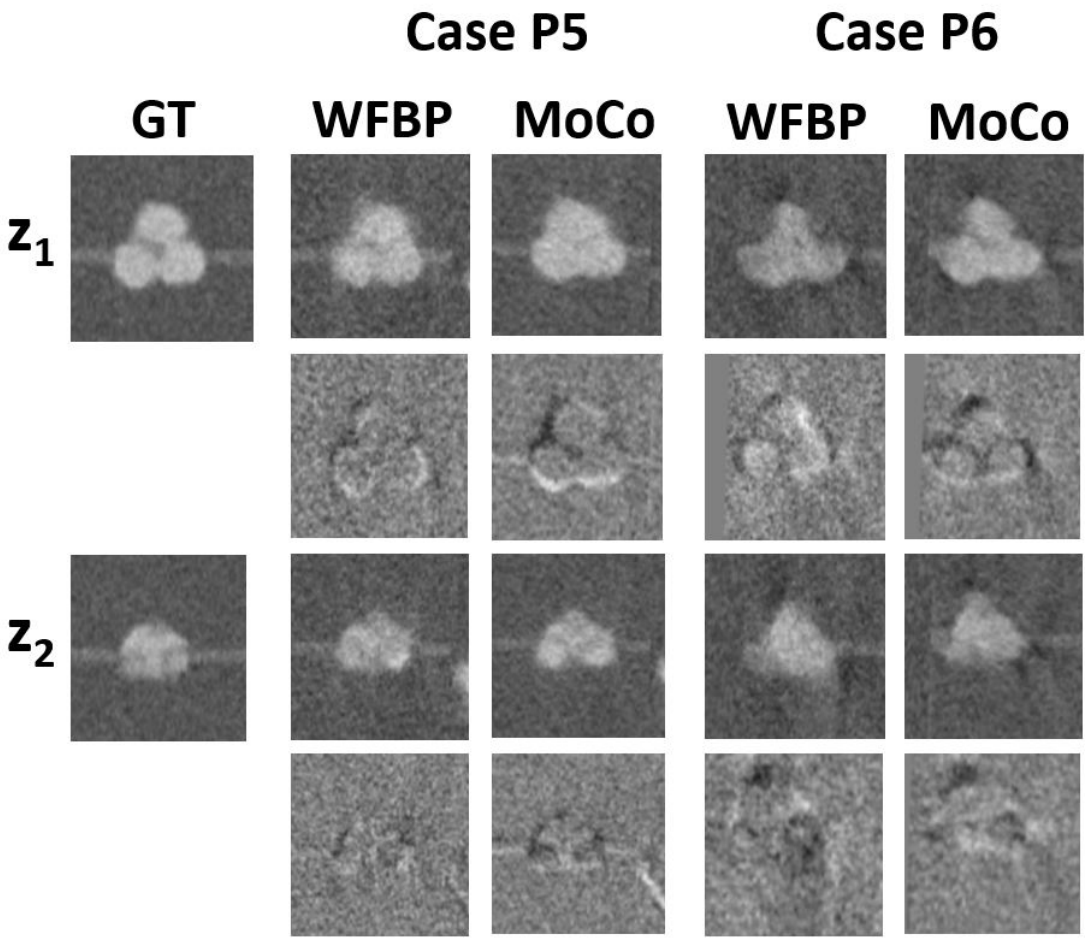

Figure 5.28: Phantom measurement results. Cases P5 and P6. AV images including the leaflets (z_1) and the base (z_2). Ground truth (GT) and difference images with respect to the GT are included. $C = 200$ HU, $W = 1200$ HU.

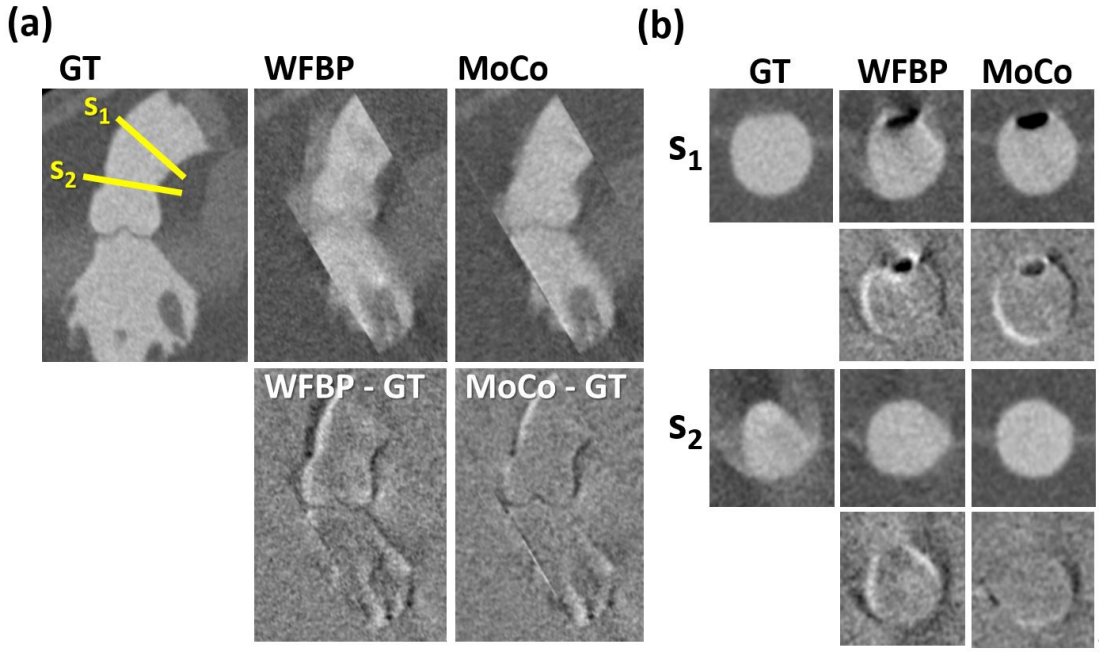

Figure 5.29: Phantom measurement results. Case P6. **(a)** Image slices orthogonal to the AV plane. s_1 and s_2 are two slice positions. **(b)** Image slices orthogonal to the aorta. The slice positions are marked in (a). Ground truth (GT) and difference images with respect to the GT are included in (a) and (b). $C = 200$ HU, $W = 1200$ HU.

Case & stack number	$v_{\max}$ [mm/s]	q_{vel}	q_{grad}	Case stack number	$v_{\max}$ [mm/s]	q_{vel}	q_{grad}
PA.1	0	0.69	1.21	P2.3	35	0.50	1.06
PA.2	0	0.76	1.18	P2.4	35	0.60	1.20
PA.3	0	0.86	1.22	P3.1	35	0.72	1.27
PB.1	0	0.55	1.29	P3.2	35	0.74	1.25
PB.2	0	0.63	1.16	P3.3	35	0.57	1.21
PB.3	0	0.79	1.36	P3.4	35	0.65	1.32
PC.1	0	1.00	1.15	P4.1	35	0.58	1.22
PC.2	0	0.41	0.48	P4.2	35	0.48	0.93
PC.3	0	0.76	0.91	P4.3	35	0.63	1.25
PD.1	0	0.98	1.00	P4.4	35	0.60	1.16
PD.2	0	0.53	0.40	P5.1	35	0.57	1.21
PD.3	0	0.68	0.48	P5.2	35	0.53	1.36
P1.1	35	0.52	0.68	P5.3	35	0.70	1.25
P1.2	35	0.63	1.22	P5.4	35	0.75	1.33
P1.3	35	0.71	1.29	P6.1	35	0.74	1.27
P1.4	35	0.70	1.24	P6.2	35	0.73	1.23
P2.1	35	0.63	1.21	P6.3	35	0.51	1.09
P2.2	35	0.61	1.33	P6.4	35	0.70	1.14

Table 5.4: Numerical results for valve MoCo with phantom data. $v_{\max}$ is the maximum AV phantom velocity.

6 Discussion

Stack Transition Artifact Removal

The stack transition artifact removal method with automatic registration parameter selection considerably improved image quality for stack transition artifact impaired data sets. It includes safeguards that prevent the introduction of distortions and extensive manipulation of individual and small anatomical structures, such as coronary arteries or valve leaflets. While this limits the precision of the method, it enables a presumed safe application to different data sets without user input. If one has to choose a constant parameter, $\sigma = 4.0$ mm is a good compromise for all data sets, but the adaptive setting yields better results overall. Thirteen patient data sets resulting in 33 individual registrations performed were evaluated. Using two numerical measures, the RMSE and the difference image entropy, visually observed improvements in image quality were affirmed. Generally, all evaluated data sets showed significant improvements in terms of the numeric measures. A more precise error estimation may prove beneficial and an improvement of the RMSE or the difference entropy alone does not generally guarantee a complete removal of stack transition artifacts. Further internal settings of the algorithm, for example automatic smoothing parameter selection, may be adjusted to improve registration performance, but have been fixed for this work to ensure a "safe" deformation of the volumes and yielded satisfactory results. The presence of motion artifacts may partly obscure stack transition artifacts and affect registration performance. Using motion compensation for coronary arteries resulted in better registration performance in one case. Given a constant smoothing parameter, applying the method to volumes of a different scale, e.g. pediatric images, would require a reevaluation and probably an adaption of the parameterization. The automatic parameterization will potentially make such a switch easier, as it relies on an initialization that yields case-dependent results as opposed to fixed, scale/size range-dependent values. The simulation study, that was performed using two further patient data sets, showed that generally, STAR managed to compute similar MVFs to the ground truth or approach it. Important factors for achieving or deviating from the ground truth include missing shared data or anatomical structures in the overlap region. Furthermore, not every MVF gradient of the ground truth may be reproduced given the MVF regularization. The simulations suggest that given a ground truth, STAR will approach it within the restrictions imposed by the MVF regularization and by the required data redundancy in the overlap region. STAR performed for a range of different stack overlaps in this study. Theoretically,

registration can be performed with minimal overlaps of the stacks. For instance with less than 1 mm or just one slice. However, it is to be expected that minimal overlaps may negatively affect registration performance. The algorithm may pull in gray values from outside the overlap but if a structure is not present in one of the stacks at all, proper registration is impossible. That is generally more likely with smaller overlaps. Given overlapping stacks, the Demons algorithm requires at least some overlap between equivalent structures to perform properly. STAR could be applied to cardiac data with various motion/displacement magnitudes without requiring user input and performed satisfactory.

Partial Angle Based Motion Compensation

A motion compensation method using PARs and the image entropy with adaptively weighted regularization was implemented and validated using clinical data. Nineteen data sets were reconstructed at two phases and a motion artifact-free reconstruction provided a reference for evaluation for many of the cases. The focus was on the AV. The valve MoCo was able to improve the image quality of each motion impaired reconstruction, while maintaining image quality in case of artifact-free images. A considerable improvement has been observed for most of the motion artifact impaired reconstructions and for major and minor artifacts alike. Blurring has been observed in the valve MoCo results. Blurring can generally be an effect of interpolation but herein it also may have been favored by the cost function itself. Results from phantom data showed that valve MoCo may compute MVFs and introduce blurring in motion-free regions. MVFs with velocities and gradients of similar magnitude, both for some artifact-impaired and unimpaired reconstructions were computed for clinical and phantom data alike. For the artifact-free/motion-free cases, the changes introduced by the MoCo were minimal, especially for clinical data. The valve MoCo was capable of improving image quality for phantom data, however the performance was considerably worse than for clinical data. Furthermore, the phantom data required a higher strain limit. This can be explained by considering that the MoCo was optimized for an elastic motion and the phantom performed a translation with static surroundings. The phantom measurements showed that the valve MoCo may converge to local minima unrelated to moving structures. That is likely tied to the image noise. Nevertheless, these factors did not seem to dominate the results for clinical data. Therein, valve MoCo reliably removed motion artifacts and no indications were found that the shape of the corrected AV was excessively or unexpectedly altered from the reference images. The closed state of the valves did not seem to have been artificially changed as well. The most obvious improvements have been observed for strong, tail or streak-shaped artifacts at the outer AV boundaries. It can be argued that the artifact classification was subjective or to some extent, loose, however the magnitude of many of the removed artifacts was obvious. Very fine and complex motion, most importantly of the valve leaflets themselves, was not addressed and would require a more specialized motion model. It should be noted, that image quality was improved at the valve leaflets but also that the AV was closed in most reconstructions. Consequently, the valve leaflets are not expected to have been

viewed at peak velocities. The MVF velocities and strain values were constrained to feasible values found in literature. For the clinical data, the constraints included rather the lower than the upper range of said values, as peak velocity and strain are not expected at the AV. The last statement excludes the individual movement of the valve leaflets, which can be rapid. The MVF constraints were applied isotropically and did not reflect the fact, that cardiac velocity and strain vary with location and direction. The valve MoCo was also jointly applied with STAR, which benefited image quality. That includes cases, where valve MoCo had previously introduced or enhanced stack transition artifacts. Finally, the greatest improvement in image quality for the therefor displayed cases was achieved through combination of the two artifact removal methods.

7 Conclusions

The stack transition artifact removal method and the partial angle reconstruction based motion compensation have both been shown to be feasible and produced satisfactory results. The selection of some of the method's parameters that were crucial for performance and stability was automated and carried out for each individual artifact correction task. Automation did not only improve ease of use but was also an important factor to ensure that the transformations applied to the clinical data were realistic. Prior knowledge about cardiac anatomy has been succefully used and more detailed, anatomical information, for example about the orientation of the heart, may further improve motion compensation performance. The automated extraction of such complex information may be enabled through the use of neural networks. While the validation data pool would benefit from higher numbers and being more diverse, for example with respect to CT scanners, the capabilities of the artifact correction methods could be clearly observed. In conclusion, STAR and valve MoCo both contribute solutions aimed at known problems in cardiac CT and provide measures to clearly improve image quality.

Bibliography

[1] J. Taron, B. Foldyna, P. Eslami, U. Hoffmann, K. Nikolaou, and F. Bamberg. Cardiac computed tomography – More than coronary arteries? A clinical update. *RöFo*, 191(9):817–826, 2019.

[2] G. Feuchtner. Imaging of cardiac valves by computed tomography. *Scientifica*, 2013:1–13, 2013.

[3] C. R. Hamilton-Craig, D. Friedman, and S. Achenbach. Cardiac computed tomography—Evidence, limitations and clinical application. *Heart, Lung & Circulation*, 21(2):70–81, 2011.

[4] M. M. Lell, J. E. Wildberger, H. Alkadhi, J. Damilakis, and M. Kachelrieß. Evolution in computed tomography: the battle for speed and dose. *Investigative Radiology*, 50(9):629–644, Sept. 2015.

[5] M. M. Lell and M. Kachelrieß. Recent and upcoming technological developments in computed tomography: High speed, low dose, deep learning, multienergy. *Investigative Radiology*, 55(1):8–19, 2020.

[6] M. Kachelrieß and W. A. Kalender. Electrocardiogram–correlated image reconstruction from subsecond spiral computed tomography scans of the heart. *Medical Physics*, 25(12):2417–2431, Dec. 1998.

[7] M. Kachelrieß, S. Ulzheimer, and W. A. Kalender. ECG–correlated image reconstruction from subsecond multi–slice spiral CT scans of the heart. *Medical Physics*, 27(8):1881–1902, Aug. 2000.

[8] M. Kachelrieß, S. Ulzheimer, and W. A. Kalender. ECG–correlated imaging of the heart with subsecond multislice CT. *IEEE Transactions on Medical Imaging*, 19(9):888–901, Sept. 2000.

[9] B. M. Ohnesorge, C. R. Becker, T. Flohr, A. Knez, and M. Reiser. *Multi-slice and Dual-source CT in Cardiac Imaging. Principles – Protocols – Indications – Outlook*. Springer Berlin Heidelberg, second edition edition, 2007.

[10] ICRP. Radiologocal protection in cardiology. ICRP publication 120. *Annals of the ICRP*, 42(1), 2013.

[11] H. Scheffel, H. Alkadhi, S. Leschka, A. Plass, L. Desbiolles, I. Guber, T. Krauss, J. Gruenenfelder, M. Genoni, T. F. Luescher, B. Marincek, and P. Stolzmann. Low–dose CT coronary angiography in the step–and–shoot mode: Diagnostic performance. *Heart*, 94(9):1132–1137, 2008.

[12] H. Alkadhi, P. Stolzmann, L. Desbiolles, S. Baumueller, R. Goetti, A. Plass, H. Scheffel, G. Feuchtner, V. Falk, B. Marincek, and S. Leschka. Low-dose, 128-slice, dual-source CT coronary angiography: Accuracy and radiation dose of the high-pitch and the step-and-shoot mode. *Heart*, 96(12):933–938, 2010.

[13] J.-F. Paul, A. Rohnean, E. Elfassy, and A. Sigal-Cinqualbre. Radiation dose for thoracic and coronary step-and-shoot CT using a 128-slice dual-source machine in infants and small children with congenital heart disease. *Pediatric Radiology*, 41(2):244–249, 2011.

[14] S. Abbara, P. Blanke, C. D. Maroules, M. Cheezum, A. D. Choi, B. K. Han, M. Marwan, C. Naoum, B. L. Norgaard, R. Rubinshtein, P. Schoenhagen, T. Villines, and J. Leipsic. SCCT guidelines for the performance and acquisition of coronary computed tomographic angiography: A report of the Society of Cardiovascular Computed Tomography guidelines committee: Endorsed by the North American Society for Cardiovascular Imaging (NASCI). *Journal of Cardiovascular Computed Tomography*, 10(6):435–449, 2016.

[15] H. Schödube, T. Allmendinger, K. Stierstorfer, H. Bruder, and T. Flohr. Evaluation of a novel CT image reconstruction algorithm with enhanced temporal resolution. *SPIE Medical Imaging Proc.*, 7961:79611N-1–7, 2011.

[16] J. Tang, J. Hsieh, and G.-.-H. Chen. Temporal resolution improvement in cardiac CT using PICCS: performance studies. *Medical Physics*, 37(8):4377–4388, Aug. 2010.

[17] M. Kachelrieß. Iterative reconstruction techniques: what do they mean for cardiac CT? *Curr. Cardiovasc. Imaging Rep.*, 6:268–281, 2013.

[18] U. v. Stevendaal, J. v. Berg, C. Lorenz, and M. Grass. A motion–compensated scheme for helical cone-beam reconstruction in cardiac CT angiography. *Medical Physics*, 35(7):3239–3251, 2008.

[19] U. Jandt, D. Schäfer, M. Grass, and V. Rasche. Automatic generation of time resolved motion vector fields of coronary arteries and 4D surface extraction using rotational x-ray angiography. *Physics in Medicine and Biology*, 54:45–64, 2009.

[20] A. Isola, M. Grass, and W. Niessen. Fully automatic nonrigid registration–based local motion estimation for motion–corrected iterative cardiac CT reconstruction. *Medical Physics*, 37(3):1093–1109, 2010.

[21] A. A. Isola, C. T. Metz, M. Schaap, S. Klein, M. Grass, and W. J. Niessen. Cardiac motion–corrected iterative cone–beam CT reconstruction using a semi–automatic minimum cost path–based coronary centerline extraction. *Compute. Med. Imag. Graph.*, 36(3):215–226, Apr. 2012.

[22] R. Bhagalia, J. Pack, and M. Miller J.V. Iatrou. Nonrigid registration-based coronary artery motion correction for cardiac computed tomography. *Medical Physics*, 39(7):4245–4254, 2012.

[23] Q. Tang, J. Cammin, S. Srivastava, and K. Taguchi. A fully four–dimensional, iterative motion estimation and compensation method for cardiac CT. *Medical Physics*, 39(7):4291–4305, 2012.

[24] S. Kim, Y. Chang, and J. B. Ra. Cardiac motion correction for helical CT scan with an ordinary pitch. *IEEE Transactions on Medical Imaging*, 37(7):1587–1596, 2018.

[25] C. Rohkohl, H. Bruder, K. Stierstorfer, and T. Flohr. Improving best–phase image quality in cardiac CT by motion correction with MAM optimization. *Medical Physics*, 40(3):031901-1–15, 2013.

[26] J. Hahn, H. Bruder, C. Rohkohl, T. Allmendinger, K. Stierstorfer, T. Flohr, and M. Kachelrieß. Motion compensation in the region of the coronary arteries based on partial angle reconstructions from short scan CT data. *Medical Physics*, 44(11):5795–5813, 2017.

[27] T. Lossau (née Elss), H. Nickisch, T. Wissel, R. Bippus, H. Schmitt, M. Morlock, and M. Grass. Motion estimation and correction in cardiac CT angiography images using convolutional neural networks. *Computerized Medical Imaging and Graphics*, 76:101640, 2019.

[28] J. Maier, S. Lebedev, E. Eulig, S. Sawall, E. Fourni, K. Stierstorfer, and M. Kachelrieß. Coronary artery motion compensation for short-scan cardiac CT using a spatial transformer network. In *Conference program of the 6th international conference on image formation in x-ray computed tomography*, pages 252–255, 2020.

[29] S. Jung, S. Lee, B. Jeon, Y. Jang, and H. J. Chang. Deep learning cross-phase style transfer for motion artifact correction in coronary computed tomography angiography. *IEEE Access*, 8:81849–81863, 2020.

[30] J. Maier, S. Lebedev, J. Erath, E. Eulig, S. Sawall, E. Fournie, K. Stierstorfer, and M. Kachelrieß. Deep learning-based coronary artery motion estimation and compensation for short-scan cardiac CT. *Medical Physics*:in print, 2021.

[31] S. Achenbach, M. Manolopoulos, A. Schuhbäck, D. Ropers, J. Rixe, C. Schneider, G. A. Krombach, M. Uder, C. Hamm, W. G. Daniel, and M. Lell. Influence of heart rate and phase of the cardiac cycle on the occurrence of motion artifact in dual-source CT angiography of the coronary arteries. *Journal of Cardiovascular Computed Tomography*, 6(2):91–98, 2012.

[32] T. Kondo, K. Takamura, S. Fujimoto, S. Takase, T. Sekine, H. Matsutani, F. J. Rybicki, and K. K. Kumamaru. Motion artifacts on coronary CT angiography images in patients with a pericardial effusion. *Journal of Cardiovascular Computed Tomography*, 8(1):19–25, 2014.

[33] G. Pontone, D. Andreini, E. Bertella, A. Baggiano, S. Mushtaq, M. Loguercio, C. Segurini, E. Conte, V. Beltrama, A. Annoni, A. Formenti, M. Petullà, A. I. Guaricci, P. Montorsi, D. Trabattoni, A. L. Bartorelli, and M. Pepi. Impact of an intra-cycle motion correction algorithm on overall evaluability and diagnostic accuracy of computed tomography coronary angiography. *European Radiology*, 26(1):147–156, 2016.

[34] D. Suchá, P. Symersky, W. Tanis, W. P. M. Mali, T. Leiner, L. A. Van Herwerden, and R. P. Budde. Multimodality imaging assessment of prosthetic heart valves. *Circulation: Cardiovascular Imaging*, 8(9):1–14, 2015.

[35] R. Manzke, M. Grass, T. Nielsen, G. Shechter, and D. Hawkes. Adaptive temporal resolution optimization in helical cardiac cone beam CT reconstruction. *Medical Physics*, 30(12):3072–3080, Dec. 2003.

[36] R. Manzke, M. Grass, and D. Hawkes. Artifact analysis and reconstruction improvement in helical cardiac cone beam CT. *IEEE Transactions on Medical Imaging*, 23(9):1150–1164, 2004.

[37] K. Taguchi, B. S Chiang, and I. Hein. Direct cone-beam cardiac reconstruction algorithm with cardiac banding artifact correction. *Medical Physics*, 33:521–39, Mar. 2006.

[38] T. Buzug. *Computed Tomography*. Springer, 2008.

[39] S. Greilich and J.-M. Osinga-Blättermann. Kapitel 1 - Strahlenphysik. In W. Schlegel, O. Jaekel, and C. Karger, editors, *Medizinische Physik*, pages 1–35. Springer, Heidelberg, 1st edition, 2017.

[40] D. Meschede. *Gerthsen Physik*. Springer Berlin Heidelberg, 24th edition, 2010.

[41] *Diagnostic Radiology Physics*. International Atomic Energy Agency, 2014.

[42] M. J. Berger, J. H. Hubbell, S. M. Seltzer, J. Chang, J. S. Coursey, R. Sukumar, D. S. Zucker, and K. Olsen. Xcom: Photon cross section database (version 1.5). *National Institute of Standards and Technologies (U.S. Department of Commerce)*, 2010. URL: `http://physics.nist.gov/xcom` (visited on 12/25/2020).

[43] R. H. Pratt, A. Ron, and H. K. Tseng. Atomic Photoelectric Effect Above 10 keV. *Rev. Mod. Phys.*, 45:273–325, 2, 1973.

[44] P. Kane, L. Kissel, R. Pratt, and S. Roy. Elastic scattering of γ-rays and x-rays by atoms. *Physics Reports*, 140(2):75–159, 1986.

[45] B. W. King, K. A. Landheer, and P. C. Johns. X-ray coherent scattering form factors of tissues, water and plastics using energy dispersion. *Physics in Medicine and Biology*, 56(14):4377–4397, 2011.

[46] B. van der Heyden, G. P. Fonseca, M. Podesta, I. Messner, N. Reisz, A. Vaniqui, H. Deutschmann, P. Steininger, and F. Verhaegen. Modelling of the focal spot intensity distribution and the off-focal spot radiation in kilovoltage x-ray tubes for imaging. *Physics in Medicine & Biology*, 65(2):025002, 2020.

[47] M. Kachelrieß. Kapitel 8 - Computertomographie. In W. Schlegel, O. Jaekel, and C. Karger, editors, *Medizinische Physik*, pages 153–203. Springer, Heidelberg, 1st edition, 2017.

[48] D. M. Tucker, G. T. Barnes, and D. P. Chakraborty. Semiempirical model for generating tungsten target x–ray spectra. *Medical Physics*, 18(3):211–218, Mar. 1991.

[49] R. Deslattes, E. Kessler Jr., P. Indelicato, L. de Billy, E. Lindroth, J. Anton, J. Coursey, D. Schwab, C. Chang, R. Sukumar, K. Olsen, and R. Dragoset. X-ray transition energies (version 1.2). *National Institute of Standards and Technologies (U.S. Department of Commerce)*, 2005. URL: `http://physics.nist.gov/XrayTrans` (visited on 01/03/2021).

[50] M. Nikl. Scintillation detectors for x-rays. *Measurement Science & Technology*, 17(4):R37–R54, 2006.

[51] M. Reiser. *Multislice CT*. Springer Berlin Heidelberg, 2009. ISBN: 978-3-540-33124-7.

[52] L. Klein, S. Dorn, C. Amato, S. Heinze, M. Uhrig, H.-P. Schlemmer, M. Kachelrieß, and S. Sawall. Effects of detector sampling on noise reduction in clinical photon-counting whole-body computed tomography. *Investigative Radiology*, 55(2):111–119, 2020.

[53] K. Taguchi and J. S. Iwanczyk. Vision 20/20: Single photon counting x–ray detectors in medical imaging. *Medical Physics*, 40(10):100901, Oct. 2013.

[54] M. Kachelrieß and W. A. Kalender. Presampling, algorithm factors and noise: considerations for CT in particular and for medical imaging in general. *Medical Physics*, 32(5):1321–1334, May 2005.

[55] H. Krieger. *Strahlungsmessung und Dosimetrie*. Springer Spektrum, 2013. ISBN: 978-3-658-00386-9.

[56] ICRP. The 2007 recommendations of the International Commission on Radiological Protection. ICRP publication 103. *Ann. ICRP*, 37(2-4), 2007.

[57] ICRP. Radiological protection in medicine. ICRP publication 105. *Ann. ICRP*, 37(6), 2007.

[58] S. J. Wilderman and Y. K. Dewaraja. Method for fast CT/SPECT-based 3D Monte Carlo absorbed dose computations in internal emitter therapy. *IEEE Transactions on Nuclear Science*, 54(1):146–151, 2007.

[59] J. J. DeMarco, C. H. Cagnon, D. D. Cody, D. M. Stevens, C. H. McCollough, M. Zankl, E. Angel, and M. F. McNitt-Gray. Estimating radiation doses from multidetector CT using Monte Carlo simulations: Effects of different size voxelized patient models on magnitudes of organ and effective dose. *Physics in Medicine and Biology*, 52(9):2583–2597, 2007.

[60] K. Perisinakis, A. Tzedakis, and J. Damilakis. On the use of Monte Carlo-derived dosimetric data in the estimation of patient dose from CT examinations. *Medical Physics*, 35(5):2018–2028, 2008.

[61] P. Deak, M. van Straten, P. C. Shrimpton, M. Zankl, and W. A. Kalender. Validation of a Monte Carlo tool for patient-specific dose simulations in multi-slice computed tomography. *European Radiology*, 18(4):759–772, 2008.

[62] L. J. Wilson, W. D. Newhauser, C. W. Schneider, F. Kamp, M. Reiner, J. C. Martins, G. Landry, A. Giussani, R.-P. Kapsch, and K. Parodi. Method to quickly and accurately calculate absorbed dose from therapeutic and stray photon exposures throughout the entire body in individual patients. *Medical Physics*, 47(5):2254–2266, 2020.

[63] K. B. Larson and S. C. Prasad. Absorbed-dose computations for inhomogeneous media in radiation-treatment planning using differential scatter-air ratios. In *Proceedings of the Annual Symposium on Computer Application in Medical Care*, 1978.

[64] E. T. Norris, X. Liu, and J. Hsieh. Deterministic absorbed dose estimation in computed tomography using a discrete ordinates method. *Medical Physics*, 42(7):4080–4087, 2015.

[65] C. McCollough, S. Leng, L. Yu, D. Cody, J. Boone, and M. McNitt-Gray. CT dose index and patient dose: They are not the same thing. *Radiology*, 259(2):311–316, 2011.

[66] ICRP. 1990 recomendations of the International Commision on Radiological Protection. ICRP publication 60. *Ann. of the ICRP*, 21(1-3), 1990.

[67] O. Gosling, R. Loader, P. Venables, N. Rowles, G. Morgan-Hughes, and C. Roobottom. Cardiac CT: Are we underestimating the dose? A radiation dose study utilizing the 2007 ICRP tissue weighting factors and a cardiac specific scan volume. *Clinical Radiology*, 65(12):1013–1017, 2010.

[68] W. Huda, S. Tipnis, A. Sterzik, and J. Schoepf. Computing effective dose in cardiac CT. *Physics in Medicine and Biology*, 55(13):3675–3684, 2010.

[69] Bundesamt für Strahlenschutz. What is the level of natural radiation exposure in Germany? 2016. (Visited on 12/30/2020).

[70] A. Schegerer, R. Loose, L. J. Heuser, and G. Brix. Diagnostic reference levels for diagnostic and interventional x-ray procedures in Germany: Update and handling. *Röfo*, 191:1438–9029, 8, 2019.

[71] M. Koplay, S. Guneyli, H. Akbayrak, K. Demir, M. Sivri, A. Avci, H. Erdogan, and Y. Paksoy. Diagnostic accuracy and effective radiation dose of high pitch dual source multidetector computed tomography in evaluation of coronary artery bypass graft patency. *Wiener Klinische Wochenschrift*, 128(13):488–494, 2016.

[72] Y. Matsunaga, A. Kawaguchi, K. Kobayashi, M. Kobayashi, Y. Asada, K. Minami, S. Suzuki, and K. Chida. Effective radiation doses of CT examinations in Japan: A nationwide questionnaire-based study. *British Journal of Radiology*, 89(1058):20150671–20150671, 2016.

[73] M. Alkhorayef, A. Sulieman, K. Alzahrani, M. Abuzaid, O. I. Alomair, M. Almuwannis, S. Alghamdi, N. Tamam, and D. A. Bradley. Radiation risk for patients undergoing cardiac computed tomography examinations. *Applied radiation and isotopes*, 168:109520–109520, 2021.

[74] A. Kosmala, B. Petritsch, A. M. Weng, T. A. Bley, and T. Gassenmaier. Radiation dose of coronary CT angiography with a third-generation dual-source CT in a "real-world" patient population. *European radiology*, 29(8):4341–4348, 2019.

[75] D. Andreini, G. Pontone, S. Mushtaq, M. E. Mancini, E. Conte, M. Guglielmo, V. Volpato, A. Annoni, A. Baggiano, A. Formenti, V. Ditali, M. Perchinunno, C. Fiorentini, A. L. Bartorelli, and M. Pepi. Image quality and radiation dose of coronary CT angiography performed with whole-heart coverage CT scanner with intra-cycle motion correction algorithm in patients with atrial fibrillation. *European Radiology*, 28(4):1383–1392, 2018.

[76] G. L. Raff, K. M. Chinnaiyan, D. Share, T. Y. Goraya, E. A. Kazerooni, M. Moscucci, R. E. Gentry, and A. Abidov. Radiation dose from cardiac computed tomography before and after implementation of radiation dose-reduction techniques. *JAMA*, 301(22):2340–2348, 2009.

[77] A. Schmermund, M. Marwan, J. Hausleiter, S. Barth, O. Bruder, S. Kerber, G. Korosoglou, A. Leber, W. Moshage, S. Schröder, S. Schneider, J. Senges, and S. Achenbach. Declining radiation dose of coronary computed tomography angiography: German cardiac CT registry experience 2009–2014. *Clinical Research in Cardiology*, 106(11):905–912, 2017.

[78] D. Célier, P. Roch, C. Etard, H. Ducou Le Pointe, and H. J. Brisse. Multicentre survey on patient dose in paediatric imaging and proposal for updated diagnostic reference levels for france. Part 1: Computed tomography. *European Radiology*, 30(2):1156–1165, 2020.

[79] I. A. H. van den Berk, M. M. N. P. Kanglie, T. S. R. van Engelen, S. Bipat, M. G. W. Dijkgraaf, P. M. M. Bossuyt, W. de Monyé, J. M. Prins, and J. Stoker. Optimal imaging strategy in patients suspected of non-traumatic pulmonary disease at the emergency department: chest x-ray or ultra-low-dose CT (OPTIMACT)– a randomised controlled trial chest x-ray or ultra-low-dose CT at the ED: Design and rationale. *Diagnostic and Prognostic Research*, 2(1):20–20, 2018.

[80] C. Ludes, M. Schaal, A. Labani, M.-Y. Jeung, C. Roy, and M. Ohana. Ultra-low dose chest CT: The end of chest radiograph? *La Presse Medicale*, 45(3):291–301, 2016.

[81] Y. Kim, Y. K. Kim, B. E. Lee, S. J. Lee, Y. J. Ryu, J. H. Lee, and J. H. Chang. Ultra-low-dose CT of the thorax using iterative reconstruction: Evaluation of image quality and radiation dose reduction. *American Journal of Roentgenology*, 204(6):1197–1202, 2015.

[82] T. M. Svahn, T. Sjöberg, and J. C. Ast. Dose estimation of ultra-low-dose chest CT to different sized adult patients. *European Radiology*, 29(8):4315–4323, 2019.

[83] M. Taekker, B. Kristjansdottir, O. Graumann, C. B. Laursen, and P. I. Pietersen. Diagnostic accuracy of low-dose and ultra-low-dose CT in detection of chest pathology: A systematic review. *Clinical Imaging*, 74:139–148, 2021.

[84] C. Li, B. Liu, H. Meng, W. Lv, and H. Jia. Efficacy and radiation exposure of ultra-low-dose chest CT at 100 kvp with tin filtration in CT-guided percutaneous core needle biopsy for small pulmonary lesions using a third-generation dual-source CT scanner. *Journal of Vascular and Interventional Radiology*, 30(1):95–102, 2019.

[85] S. R. Konda, A. M. Goch, P. Leucht, A. Christiano, S. Gyftopoulos, G. Yoeli, and K. A. Egol. The use of ultra-low-dose CT scans for the evaluation of limb fractures: Is the reduced effective dose using CT in orthopaedic injury (reduction) protocol effective? *The Bone & Joint Journal*, 98-B(12):1668–1673, 2016.

[86] I. Corcuera-Solano, A. H. Doshi, A. Noor, and L. N. Tanenbaum. Repeated head CT in the neurosurgical intensive care unit: Feasibility of sinogram-affirmed iterative reconstruction-based ultra-low-dose CT for surveillance. *American Journal of Neuroradiology*, 35(7):1281–1287, 2014.

[87] C.-f. Jia, J. Zhong, X.-y. Meng, X.-x. Sun, Z.-q. Yang, Y.-j. Zou, X.-y. Wang, S. Pan, D. Yin, and Z.-q. Wang. Image quality and diagnostic value of ultra low-voltage, ultra low-contrast coronary CT angiography. *European Radiology*, 29(7):3678–3685, 2019.

[88] D. C. Benz, C. Gräni, B. Hirt Moch, F. Mikulicic, J. Vontobel, T. A. Fuchs, J. Stehli, O. F. Clerc, M. Possner, A. P. Pazhenkottil, O. Gaemperli, R. R. Buechel, and P. A. Kaufmann. A low-dose and an ultra-low-dose contrast agent protocol for coronary CT angiography in a clinical setting: Quantitative and qualitative comparison to a standard dose protocol. *British Journal of Radiology*, 90(1074):20160933–20160933, 2017.

[89] L. Zhao, J. Bao, Y. Guo, J. Li, X. Yang, T. Lv, F. Hao, Z. Wang, Z. Yang, and A. Liu. Ultra-low dose one-step CT angiography for coronary, carotid and cerebral arteries using 128-slice dual-source CT: a feasibility study. *Experimental and Therapeutic Medicine*, 17(5):4167–4175, 2019.

[90] A. Schuhbaeck, S. Achenbach, C. Layritz, J. Eisentopf, F. Hecker, T. Pflederer, S. Gauss, J. Rixe, W. Kalender, W. G. Daniel, M. Lell, and D. Ropers. Image quality of ultra-low radiation exposure coronary CT angiography with an effective dose <0.1 msv using high-pitch spiral acquisition and raw data-based iterative reconstruction. *European Radiology*, 23(3):597–606, 2013.

[91] A. N. Primak, C. H. McCollough, M. R. Bruesewitz, J. Zhang, and J. G. Fletcher. Relationship between noise, dose, and pitch in cardiac multi-detector row CT. *RadioGraphics*, 26(6):1785–1794, 2006.

[92] W. A. Kalender. *Computed Tomography- Fundamentals, System Technology, Image Quality, Applications*. Publicis Publ., 2011.

[93] G. S. Hurlock, H. Higashino, and T. Mochizuki. History of cardiac computed tomography: Single to 320-detector row multislice computed tomography. *The International Journal of Cardiovascular Imaging*, 25(S1):31–42, 2009.

[94] K. Stierstorfer, A. Rauscher, J. Boese, H. Bruder, S. Schaller, and T. Flohr. Weighted FBP — a simple approximate 3D FBP algorithm for multislice spiral CT with good dose usage for arbitrary pitch. *Physics in Medicine & Biology*, 49:2209–2218, 2004.

[95] M. K. Kalra, M. Woisetschläger, N. Dahlström, S. Singh, S. Digumarthy, S. Do, H. Pien, P. Quick, B. Schmidt, M. Sedlmair, J.-A. O. Shepard, and A. Persson. Sinogram-affirmed iterative reconstruction of low-dose chest CT: Effect on image quality and radiation dose. *American Journal of Roentgenology*, 201(2):235–244, 2013.

[96] J. Leipsic, G. Nguyen, J. Brown, D. Sin, and J. R. Mayo. A prospective evaluation of dose reduction and image quality in chest CT using adaptive statistical iterative reconstruction. *American Journal of Roentgenology*, 195(5):1095–1099, 2010.

[97] D. Marin, R. C. Nelson, S. T. Schindera, S. Richard, R. S. Youngblood, T. T. Yoshizumi, and E. Samei. Low-tube-voltage, high-tube-current multidetector abdominal CT: Improved image quality and decreased radiation dose with adaptive statistical iterative reconstruction algorithm—initial clinical experience. *Radiology*, 254(1):145–153, 2010.

[98] A. K. Hara, R. G. Paden, A. C. Silva, J. L. Kujak, H. J. Lawder, and W. Pavlicek. Iterative reconstruction technique for reducing body radiation dose at CT: Feasibility study. *American Journal of Roentgenology*, 193(3):764–771, 2009.

[99] S. Baumüller, A. Winklehner, C. Karlo, R. Goetti, T. Flohr, E. W. Russi, T. Frauenfelder, and H. Alkadhi. Low-dose CT of the lung: potential value of iterative reconstructions. *European Society of Radiology*, 22(12):2597–2606, 2012.

[100] H. Lu Liu. Model-based iterative reconstruction: A promising algorithm for today's computed tomography imaging. *Journal of Medical Imaging and Radiation Sciences*, 45(2):131–136, 2014.

[101] M. S. Bittencourt, B. Schmidt, M. Seltmann, G. Muschiol, D. Ropers, Daniel, and S. Werner Günther Achenbach. Model-based iterative reconstruction: A promising algorithm for today's computed tomography imaging. *The International Journal of Cardiovascular Imaging*, 27(7):1081–1087, 2011.

[102] M. J. Willemink, P. A. De Jong, T. Leiner, L. M. De Heer, R. A. J. Nievelstein, R. P. J. Budde, and A. M. R. Schilham. Iterative reconstruction techniques for computed tomography part 1: Technical principles. *European Radiology*, 23(6):1623–1631, 2013.

[103] M. Beister, D. Kolditzm, and W. A. Kalender. Iterative reconstruction methods in x-ray CT. *Physica Medica*, 28(2):94–108, 2012.

[104] M. Naoum Christopher, M. Blanke Philipp, and M. Leipsic Jonathon. Iterative reconstruction in cardiac CT. *Journal of Cardiovascular Computed Tomography*, 9(4):255–263, 2015.

[105] J. Leipsic, B. G. Heilbron, and C. Hague. Iterative reconstruction for coronary CT angiography: Finding its way. *The International Journal of Cardiovascular Imaging*, 28(3):613–620, 2012.

[106] H. Bruder, R. Raupach, J. Sunnegardh, M. Sedlmair, K. Stierstorfer, and T. Flohr. Adaptive iterative reconstruction. *SPIE Medical Imaging Proc.*, 7961:79610J-1–12, 2011.

[107] R. Wang, W. Yu, R. Wu, H. Yang, D. Lu, J. Liu, and C. Zhang Zhaoqi Zhang. Improved image quality in dual-energy abdominal CT: Comparison of iterative reconstruction in image space and filtered back projection reconstruction. *American Journal of Roentgenology*, 199(2):402–406, 2012.

[108] S. Singh, M. Kalra, J. Hsieh, and P. Licato. Abdominal CT : Comparison of adaptive statistical iterative and filtered back projection reconstruction techniques. *Radiology*, 257(2):373–383, 2010.

[109] P. J. Pickhardt, M. G. Lubner, D. H. Kim, J. Tang, J. a. Ruma, A. M. Del Rio, and G. H. Chen. Abdominal CT with model-based iterative reconstruction (MBIR): Initial results of a prospective trial comparing ultralow-dose with standard-dose imaging. *American Journal of Roentgenology*, 199(6):1266–1274, 2012.

[110] A. M. Kasel, S. Cassese, S. Bleiziffer, M. Amaki, R. T. Hahn, A. Kastrati, and P. P. Sengupta. Standardized imaging for aortic annular sizing: Implications for transcatheter valve selection. *JACC. Cardiovascular imaging*, 6(2):249–262, 2013.

[111] M. Loukas, E. Bilinsky, S. Bilinsky, C. Blaak, R. S. Tubbs, and R. H. Anderson. The anatomy of the aortic root. *Clinical Anatomy*, 27(5):748–756, 2014.

[112] B. Desjardins and E. A. Kazerooni. ECG-gated cardiac CT. *American Journal of Roentgenology*, 184(4):993–1010, 2004.

[113] K. Barrett, H. Brooks, S. Boitano, and S. Barman. *Ganong's Review of Medical Physiology*. McGraw Hill Professional, 2010. ISBN: 9780071605687.

[114] G. Shechter, J. R. Resar, and E. R. McCeigh. Displacement and velocity of the coronary arteries: Cardiac and respiratory motion. *IEEE Trans Med Imaging*, 25(3):369–375, 2006.

[115] F. Larrazet, D. Czitrom, F. Laborde, K. Bouabdallah, and T. Folliguet. Decreased right ventricular lateral wall velocities early after cardiac surgery. *Echocardiography*, 28(4):438–441, 2011.

[116] L. B. Pauliks, K.-C. Chan, D. Chang, S. K. Kirby, L. Logan, C. G. DeGroff, M. M. Boucek, and L. M. Valdes-Cruz. Regional myocardial velocities and isovolumic contraction acceleration before and after device closure of atrial septal defects: A color tissue Doppler study. *The American Heart Journal*, 150(2):294–301, 2005.

[117] D. F. Hernandez-Suarez and A. Lopez-Candales. Strain imaging echocardiography: What imaging cardiologists should know. *Current cardiology reviews*, 13(2):118–129, 2017.

[118] M. S. Amzulescu, M. De Craene, H. Langet, A. Pasquet, D. Vancraeynest, A. C. Pouleur, J. L. Vanoverschelde, and B. L. Gerber. Myocardial strain imaging: review of general principles, validation, and sources of discrepancies. *European heart journal cardiovascular imaging*, 20(6):605–619, 2019.

[119] A. Scatteia, A. Baritussio, and C. Bucciarelli-Ducci. Strain imaging using cardiac magnetic resonance. *Heart Failure Reviews*, 22(4):465–476, 2017.

[120] A. G. Cerillo, M. Mariani, S. Berti, and M. Glauber. Sizing the aortic annulus. *Annals of cardiothoracic surgery*, 1(2):245–256, 2012.

[121] M. T. Lu, H. Ersoy, A. G. Whitmore, M. J. Lipton, and F. J. Rybicki. Reformatted 4-chamber and short axis views of the heart using thin section ($\leq$2 mm) MDCT images. *Academic radiology*, 14(9):1108–1112, 2007.

[122] P. Blanke, J. R. Weir-McCall, S. Achenbach, V. Delgado, J. Hausleiter, H. Jilaihawi, M. Marwan, B. L. Nørgaard, N. Piazza, P. Schoenhagen, and J. A. Leipsic. Computed tomography imaging in the context of transcatheter aortic valve implantation (TAVI)/transcatheter aortic valve replacement (TAVR): An expert consensus document of the society of cardiovascular computed tomography. *JACC. Cardiovascular imaging*, 12(1):1–24, 2019.

[123] U. Hoffmann, M. Ferencik, R. C. Cury, and A. J. Pena. Coronary CT angiography. *The Journal of Nuclear Medicine*, 47(5):797–806, 2006.

[124] J. Hausleiter and T. Meyer. Estimated radiation dose associated with cardiac CT angiography. *JAMA*, 301(5):500–507, 2009.

[125] J. Hsieh, J. Londt, M. Vass, J. Li, X. Tang, and D. Okerlund. Step-and-shoot data acquisition and reconstruction for cardiac x-ray computed tomography. *Medical Physics*, 33(11):4236, 2006.

[126] B. Flach, M. Brehm, S. Sawall, and M. Kachelrieß. Deformable 3D–2D registration for CT and its application to low dose tomographic fluoroscopy. *Physics in Medicine & Biology*, 59:7865–7887, 2014.

[127] J. B. A. Maintz and M. A. Viergever. A survey of medical image registration methods. *Medical Image Analysis*, 2(1):1–36, 1998.

[128] J. Hahn, H. Bruder, T. Allmendinger, K. Stierstorfer, T. Flohr, and M. Kachelrieß. Reduction of motion artifacts in cardiac CT based on partial angle reconstructions from short scan data. In *Medical Imaging: Physics of Medical Imaging*, volume 9783 of *Proc. SPIE*, 2016.

[129] D. Škerl, D. Tomaževič, B. Likar, and F. Pernuš. Evaluation of similarity measures for reconstruction-based registration in image-guided radiotherapy and surgery. *International Journal of Radiation Oncology Biology Physics*, 65(3):943–953, 2006.

[130] S. Kim, Y. Chang, and J. B. Ra. Cardiac motion correction based on partial angle reconstructed images in x-ray CT. *Medical Physics*, 42:2560–2571, 2015.

[131] S. Lebedev, E. Fournie, K. Stierstorfer, and M. Kachelrieß. Stack transition artifact removal (STAR) for cardiac CT. *Medical Physics*, 46(11):4777–4791, 2019.

[132] S. Lebedev, E. Fournie, K. Stierstorfer, and M. Kachelrieß. Stack transition artifact removal for cardiac CT using patch-based similarities. In *Medical Imaging: Physics of Medical Imaging*, Proc. SPIE, 2018.

[133] S. Lebedev, E. Fournie, K. Stierstorfer, and M. Kachelrieß. Stack transition artifact removal for cardiac CT using a symmetric demons algorithm. In Proc. The Fifth International Conference on Image Formation in X-Ray Computed Tomography, 2018.

[134] J.-.-P. Thirion. Image matching as a diffusion process: an analogy with Maxwell's demons. *Medical Image Analysis*, 2(3):243–260, 1998.

[135] T. Vercauteren, X. Pennec, A. Perchant, and N. Ayache. Diffeomorphic demons: Efficient non–parametric image registration. *NeuroImage*, 45:S61–S72, 2009.

[136] F. N. Fritsch and R. E. Carlson. Monotone piecewise cubic interpolation. *SIAM journal on numerical analysis*, 17(2):238–246, 1980.

[137] R. J. Taylor, W. E. Moody, F. Umar, N. C. Edwards, T. J. Taylor, B. Stegemann, J. N. Townend, K. N. Hor, R. P. Steeds, W. Mazur, and F. Leyva. Myocardial strain measurement with feature-tracking cardiovascular magnetic resonance: Normal values. *European heart journal cardiovascular imaging*, 16(8):871–881, 2015.

[138] H. M. Almutairi, M. Y. Khanji, R. Boubertakh, M. E. Miquel, and S. E. Petersen. A comparison of cardiac motion analysis software packages: Application to left ventricular deformation analysis in healthy subjects. *Journal of Cardiovascular Magnetic Resonance*, 18(S1), 2016.

[139] M. Powell. An efficient method for finding the minimum of a function of several variables without calculating derivatives. *Computer Journal*, 7:155–162, 1964.

List of publications

Parts of this thesis have been published in the following journal articles and conference contributions:

Journal article

[1] **S. Lebedev**, E. Fournie, K. Stierstorfer, and M. Kachelrieß. Stack transition artifact removal (STAR) for cardiac CT. *Medical Physics*, 46(11):4777–4791, 2019.

Journal article under review

[2] **S. Lebedev**, J. Maier, E. Fournie, K. Stierstorfer, and M. Kachelrieß. Motion compensation for aortic valves using partial angle CT reconstructions. *Medical Physics*.

Conference contributions

[3] **S. Lebedev**, E. Fournie, K. Stierstorfer, and M. Kachelrieß. Stack transition artifact removal for cardiac CT using patch-based similarities. In *Medical Imaging: Physics of Medical Imaging*, Proc. SPIE, 2018.

[4] **S. Lebedev**, E. Fournie, K. Stierstorfer, and M. Kachelrieß. Stack transition artifact removal for cardiac CT using a symmetric demons algorithm. In Proc. The Fifth International Conference on Image Formation in X-Ray Computed Tomography, 2018.

Acknowledgments

Mein Dank gilt allen die mich während meiner Promotion unterstützt haben:

Prof. Dr. Peter Bachert für die Übernahme des Erstgutachtens und seine Beratung.

Prof. Dr. Marc Kachelrieß für die wissenschaftliche Betreuung und seine Rolle als Mentor während meiner Promotionszeit und davor.

Dr. Karl Stierstorfer für die Unterstützung und die Möglichkeit der Zusammenarbeit mit Siemens Healthineers und Eric Fournie für seine Unterstützung und Beratung. Ebenfalls die Kollegen von der Abteilung R&D CTC PSC.

Alle Kollegen der Arbeitsgruppe Röntgenbildgebung und Computertomographie am Dkfz für den informativen Austausch, Rat und die gesellige Atmosphäre. Ich möchte an dieser Stelle noch einmal namentlich Laura Klein, Carlo Amato, Steffan Sawall, Julien Erath, Joscha Maier und Tim Vöth für ihre fachliche Unterstützung danken.

Prof. Dr. Tilman Plehn und Prof. Dr. Norbert Herrmann für die Übernahme der mündlichen Prüfung.

I hereby assure, that I composed this work by myself and did not use any other than the listed resources.

Heidelberg, April 20, 2021

A Appendix

Acquisition of phantom measurements simulating cardiac motion at the aortic valve

Introduction

CT phantom measurements were obtained using a cardiac/AV phantom. The data was intended to contribute to the validation of valve MoCo. Similarities/relevance of the phantom measurement results to/for cardiac CT imaging were to be achieved as follows.

- Use of a cardiac phantom resembling the aorta, the left ventricle (LV) and the AV in between.
- Use of an iodine solution to fill the cardiac phantom with similar iodine concentrations used in cardiac CT.
- Use of a motion phantom to move the cardiac phantom during the scans.

Ground truth images can be reconstructed from motion-free scans. The MoCo results can be compared to the ground truth, however, the behavior of the method can be observed in the absence of motion as well. The AV phantom was purpose build for this measurement.

Materials/Hardware

- Anthropomorphic thorax phantom (QRM GmbH, Möhrendorf, Germany) and water basin insert (figure A.1)
- Motion phantom (figure A.2)
- 3D printed cardiac/AV phantom (figure A.3)
- Somatom CounT CT-Scanner (Siemens Healthineers, Forchheim, Germany) + work and control station at the German Cancer Research Center
- Two laptops for motion phantom and remote control
- Iodine solution (300 mg/ml), dropping glass, syringe and beakers

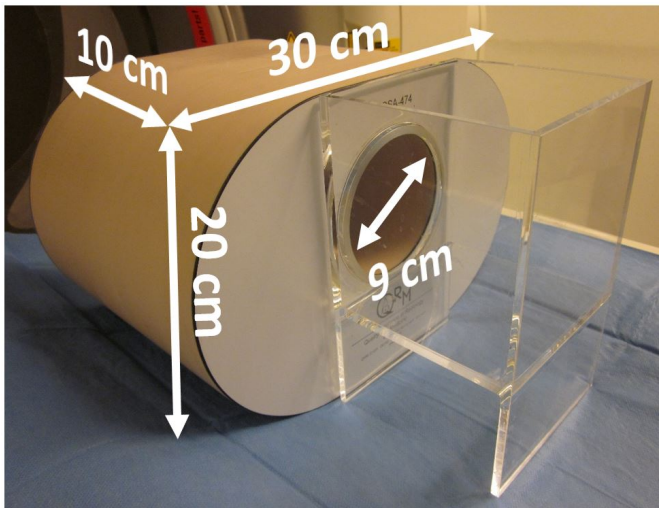

Figure A.1: Thorax phantom with water basin insert.

Motion Phantom

The motion phantom is a metal frame including stepper motors and stepper motor drivers that was available at the German Cancer Research Center. A motion that is horizontal, linear and periodic is generated through the use of a rotating disc and a rail mounted component that are connected by a transmission rod. Vertical motion is generated by lifting and lowering a component on a rotating oval shaped disc. The stepper motors are the models ST6018M2008/ST4118S1404-B and the stepper motor drivers are the model SMCI33-2 by Nanotec Electronic GmbH & Co. (Feldkirchen, Germany). The topmost component can be subjected to horizontal and vertical linear motions and an Acrylic glass rod can be attached using a fixing screw. Herein, only the horizontal motion option was used. The radius R between the rotating disc center and the attachment point of the transmission rod can be adjusted, but herein, was left fixed at $R = 2.25$. Therefore, the peak to peak amplitude of the horizontal motion is 4.5 cm. The motion phantom is displayed and the motion illustrated in figure A.2. The stepper motor drivers are controlled using a Laptop connected via a cable and the manufacturer provided software NanoPro 1.7. The Laptop itself, and therefore also the motion phantom, can be remotely controlled with another device. The angular velocity of a motor is set through a pulse frequency f_{M}. The resulting rotation frequency could be calculated as $\omega = 2\pi f_{\mathrm{M}}/400$ for the set angle step size. The mean velocity of the linear motion is then $\bar{v} = 2R\omega/\pi$ and the maximum velocity is $v_{\max} = R\omega$.

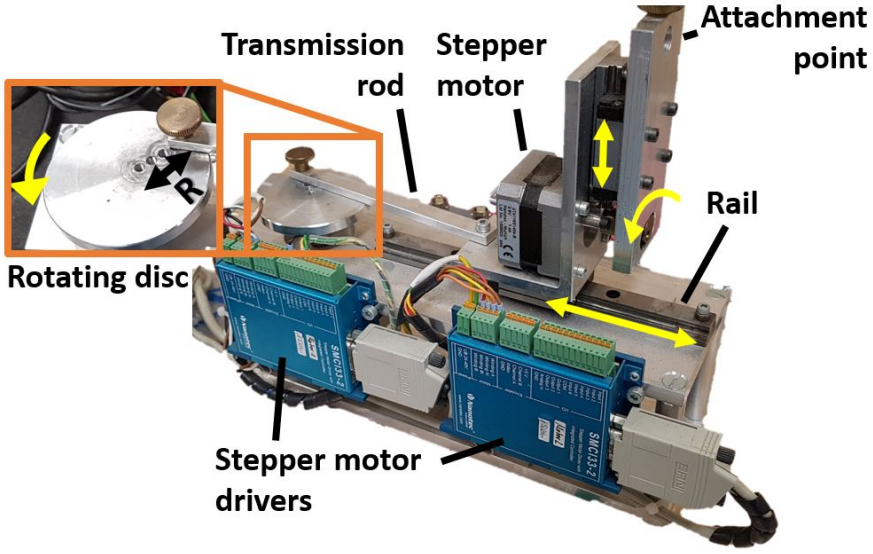

Figure A.2: Motion phantom setup. The various motions are illustrated with arrows.

Aortic Valve Phantom

A phantom modeling the closed aortic valve (AV) that can be filled with water and contrast agent was designed and produced prior to the measurements. The performed steps are illustrated in figure A.3 and described in the following.

1. A clinical cardiac CT data set is segmented to extract the aorta with the AV in its closed state and the LV, respectively, to generate two separate 3D models. First, the aorta and the LV are segmented together using thresholding. The former two are separated by performing manual voxel-wise segmentation. Additional structures like the coronary arteries are removed as well.

2. From the 3D models of the aorta and the LV, two hollow 3D models with a wall thickness of 2 mm are generated.

3. The hollow aorta and LV models are combined. The closed AV is now contained inside the resulting model, separating the aorta and the LV.

4. Supporting structures are added for stability. Screw plugs for the aorta and the LV cavities are added for filling and sealing the phantom. A structure to attach the phantom to a pole with a diameter of 2 cm that will be connected to the motion phantom is added as well.

5. 3D print the final model.

The segmentation was performed using the open source software 3D slicer and the 3D model processing was performed with the open source software Blender. The 3D printing was performed on a Objet 500 Connex 3 3D printer (Stratasys, Eden Prairie,

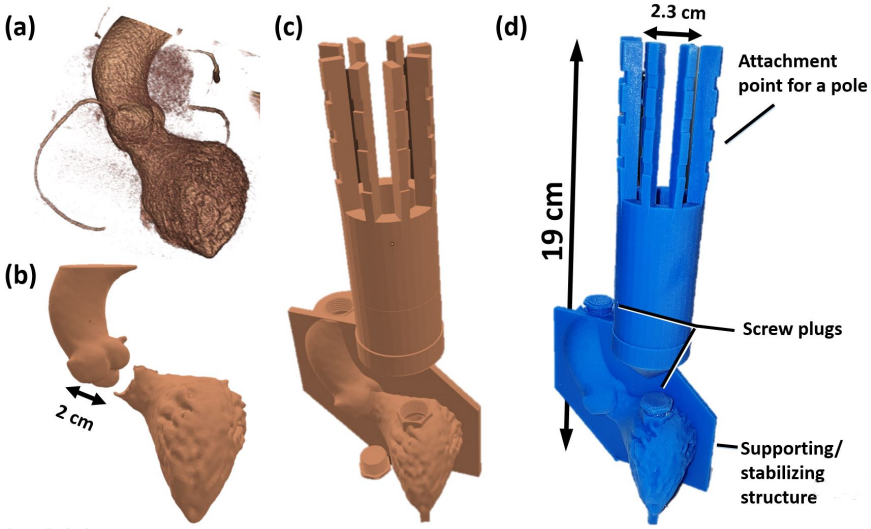

Figure A.3: Illustration of some of the steps performed to design and produce the AV phantom. **(a)** 3D volume rendering of the (threshold) segmented aorta and LV from step 1. The coronary arteries and some surrounding blood and tissue remain in the volume. **(b)** Rendering of the 3D models of the aorta and the LV from steps 1/2. **(c)** Rendering of the final 3D model including additional/support structures from step 3. **(d)** 3D printed phantom.

US/Rechovot, Israel) at the German Cancer Research Center. The material used is a polymer sold by Stratasys and named Vero. The size of the phantom had to be set to 8 cm×7 cm×19 cm to fit within the thorax phantom. The diameter of the phantom AV base was approximately 2 cm.

Somatom CounT CT Scanner

The Somatom CounT is a prototype CT scanner featuring both a photon counting and an energy integrating detector. Herein, only the latter was available for use. Relevant scanner parameters include a rotation time of 500 ms and 64 detector slices with a depth of 0.6 mm. The x-ray tube uses a flying focal spot with two positions in z-direction.

Measurement

All measurements/CT scans were performed in sequential mode using the energy integrating detector. Multiple circular short-scans with a rotation time of 500 ms are acquired to cover the extent of the thorax phantom. The tube voltage was set to 100 kV for all scans. The tube current is controlled via the tube current-time product, which was limited to a maximum of 237 mAs. All reconstructions were performed using a WFBP with the same reconstruction kernel (B25f). The created iodine solution had a concentration of approximately 17 mg I/ml, which resulted in a mean CT value

of approximately 420 HU in the reconstructions. Motion-free scans at 200 mAs were performed to acquire reference data. Reconstructions from the latter were to be used as ground truth. A motion phantom setting that resulted in clearly observable motion artifacts in the reconstructions was determined. The corresponding velocities were $\bar{v} = 22.5$ mm/s and $v_{\max} = 35.3$ mm/s. The scans with phantom motion were performed at 100 mAs. Four motion-free and six motion-impaired data sets suitable to be used for the validation were stored.

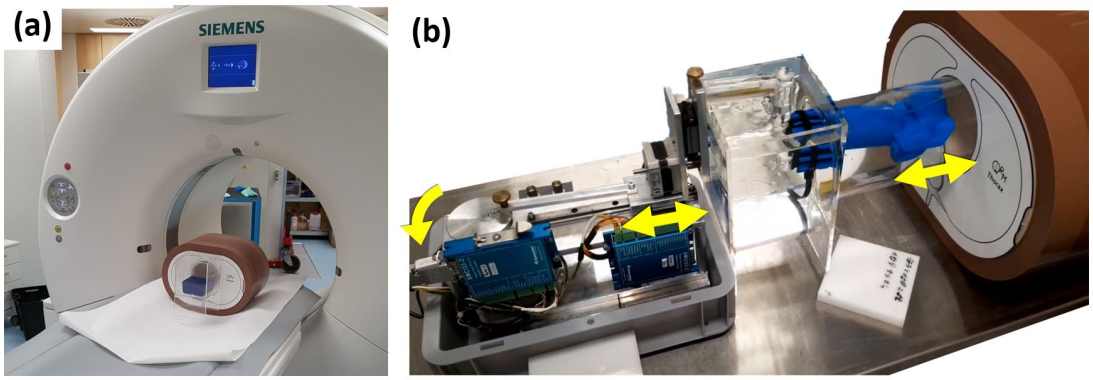

Figure A.4: **(a)** Thorax phantom placed on the Somatom CounT patient bed. **(b)** Phantom setup for the measurement. The water basin is not inserted into the thorax phantom in this image. The motions introduced by the motion phantom are marked with arrows.

B Appendix

Summary of partial angle-based motion compensation results

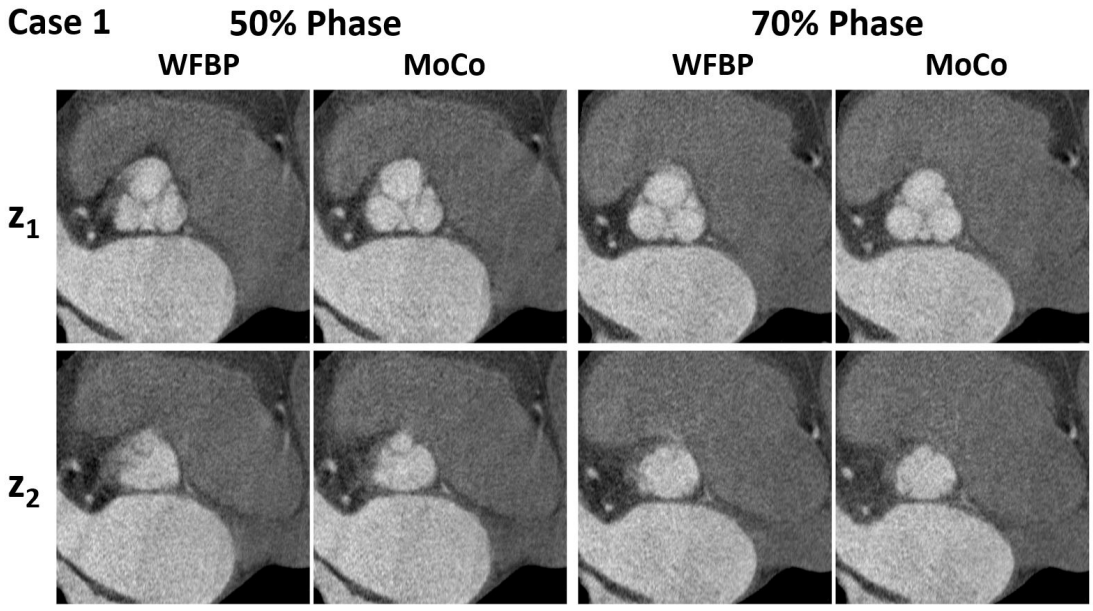

Figure B.1: Valve MoCo results for case 1. $C = 200$ HU, $W = 1200$ HU.

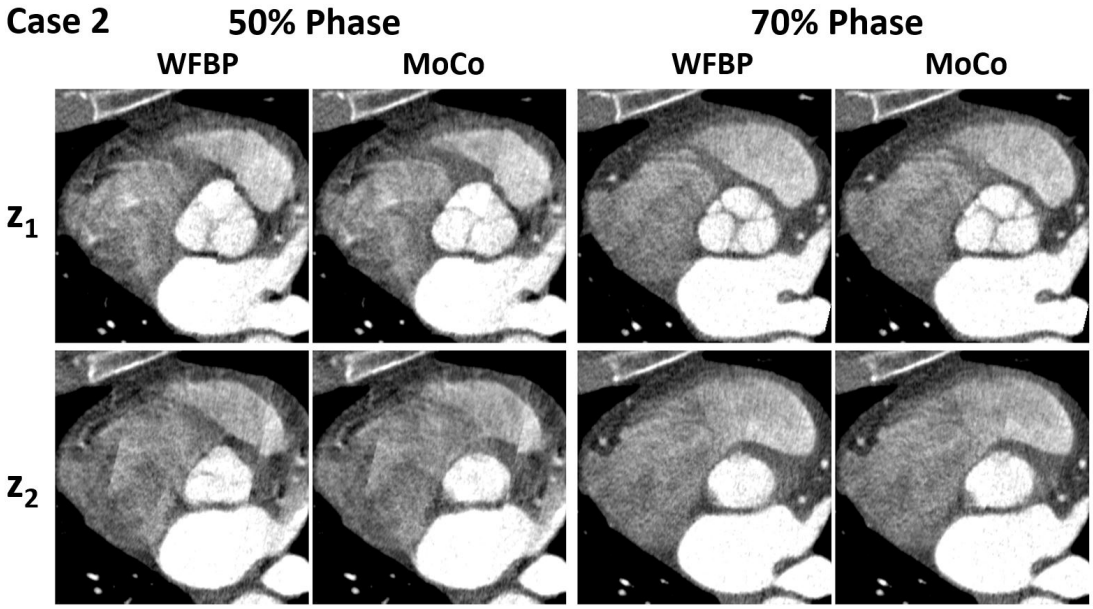

Figure B.2: Valve MoCo results for cases 2. $C = 200$ HU, $W = 1200$ HU.

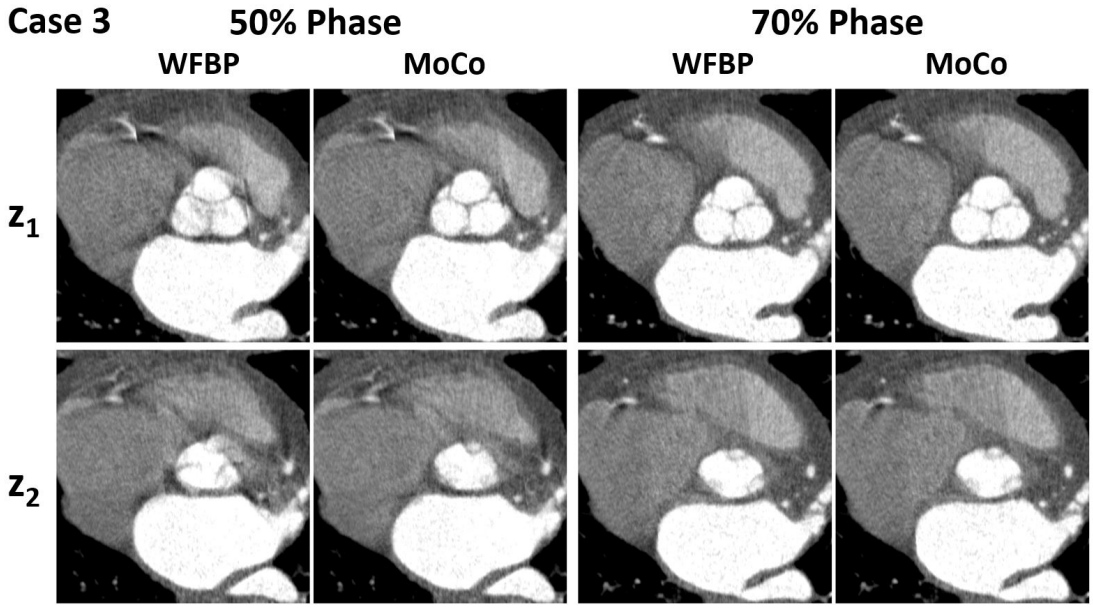

Figure B.3: Valve MoCo results for case 3. $C = 200$ HU, $W = 1500$ HU.

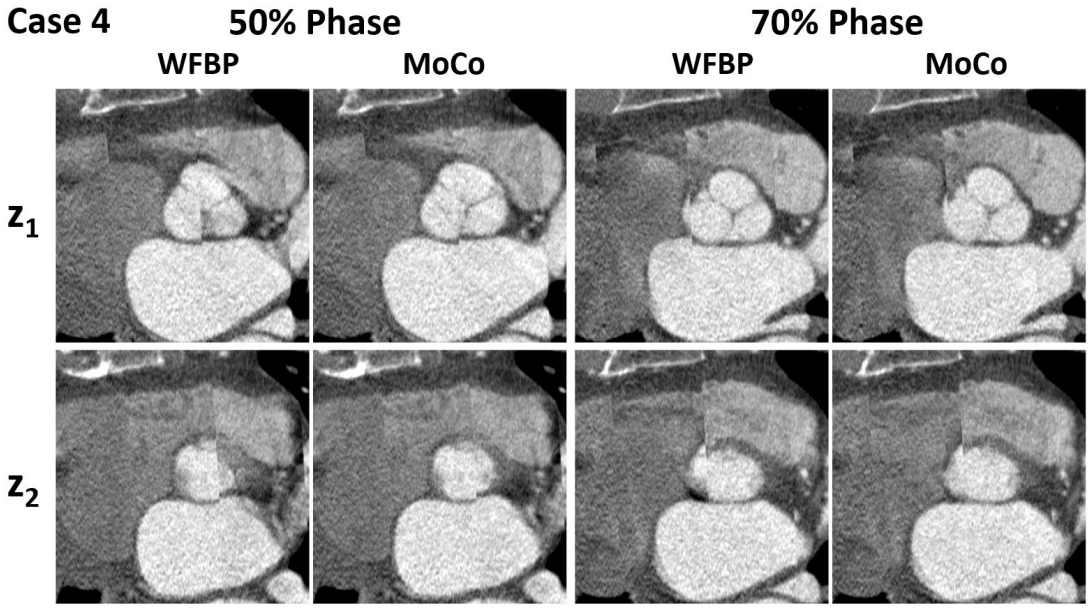

Figure B.4: Valve MoCo results for case 4. $C = 200$ HU, $W = 1200$ HU.

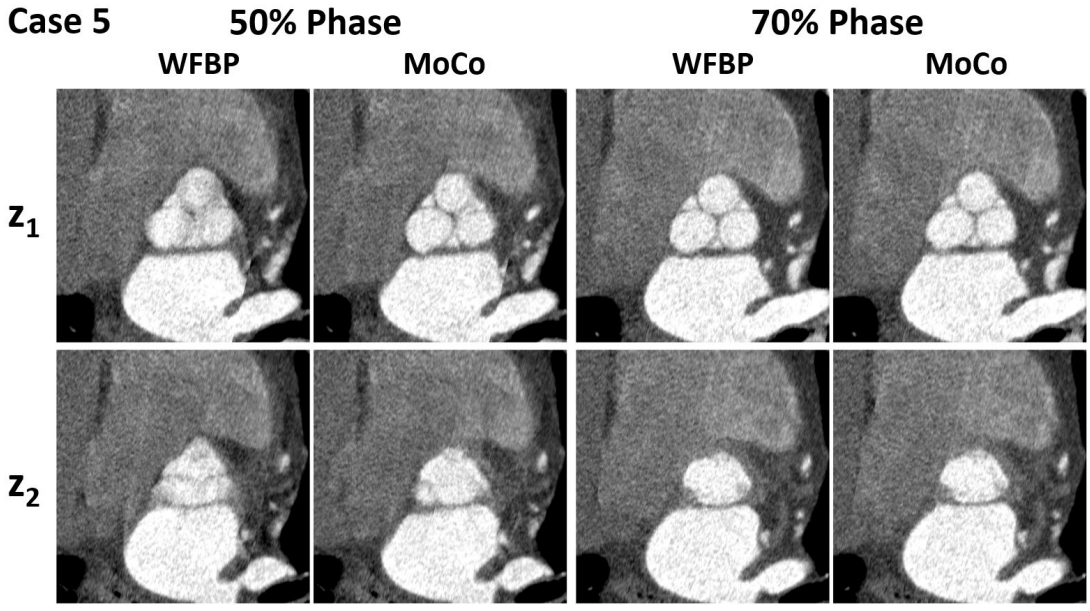

Figure B.5: Valve MoCo results for case 5. $C = 200$ HU, $W = 1200$ HU.

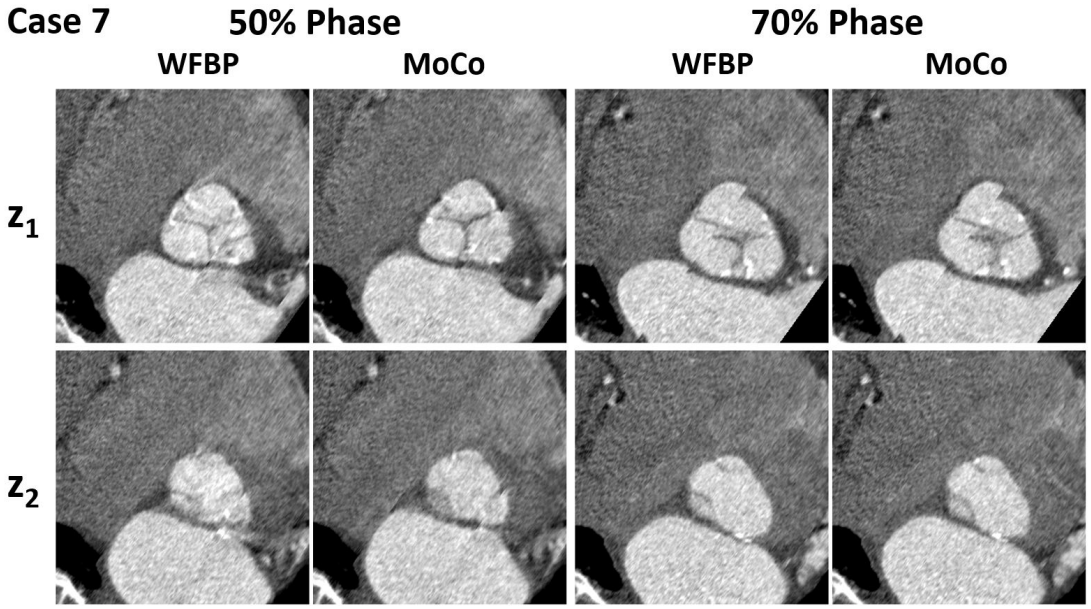

Figure B.6: Valve MoCo results for case 7. $C = 200$ HU, $W = 1200$ HU.

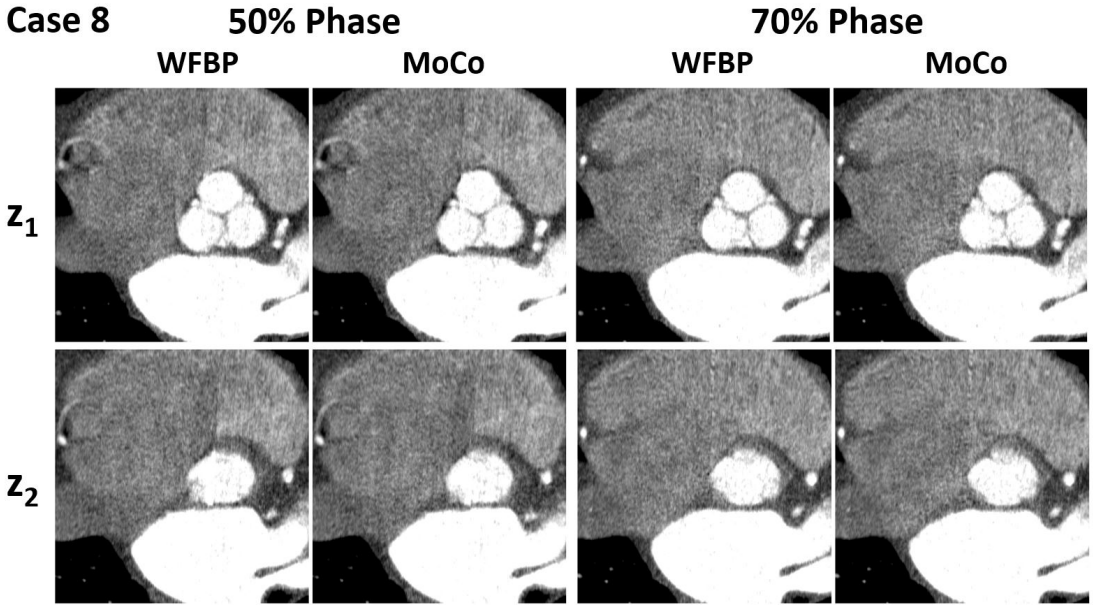

Figure B.7: Valve MoCo results for case 8. $C = 200$ HU, $W = 1200$ HU.

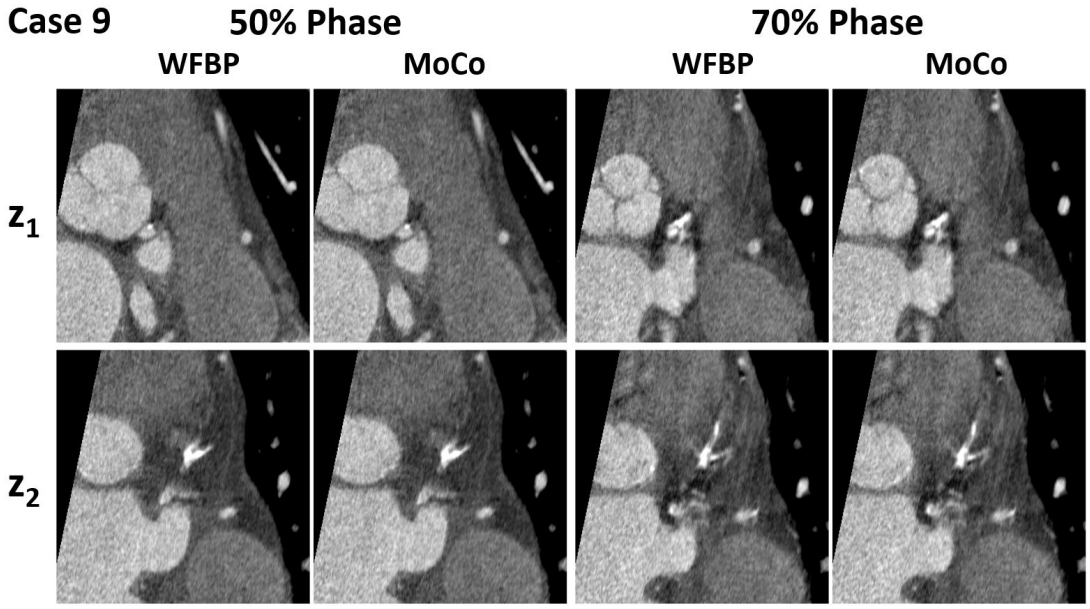

Figure B.8: Valve MoCo results for case 9. $C = 200$ HU, $W = 1200$ HU.

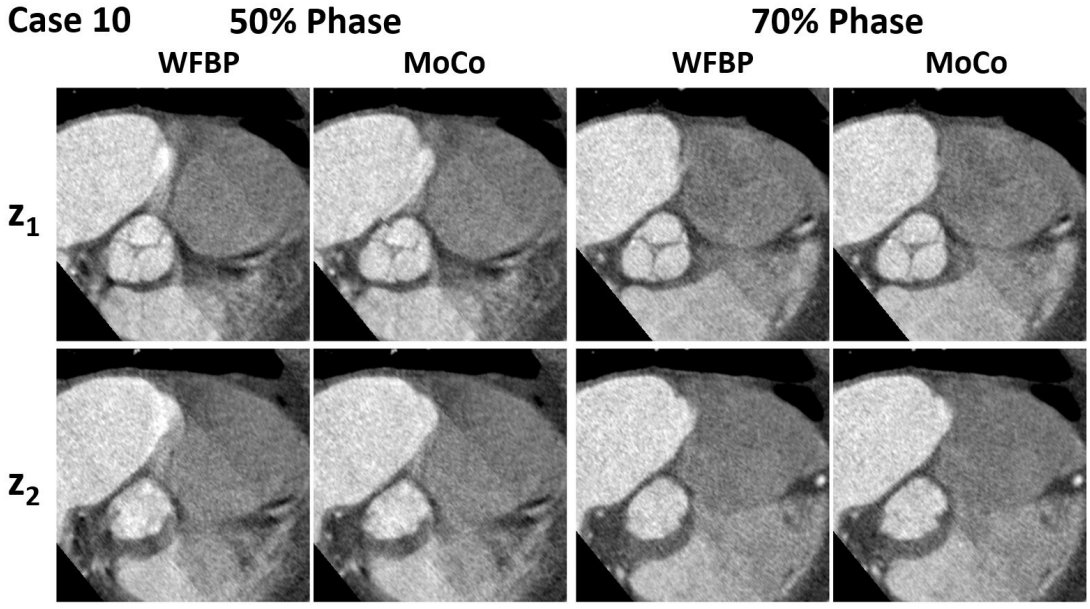

Figure B.9: Valve MoCo results for case 10. $C = 200$ HU, $W = 1200$ HU.

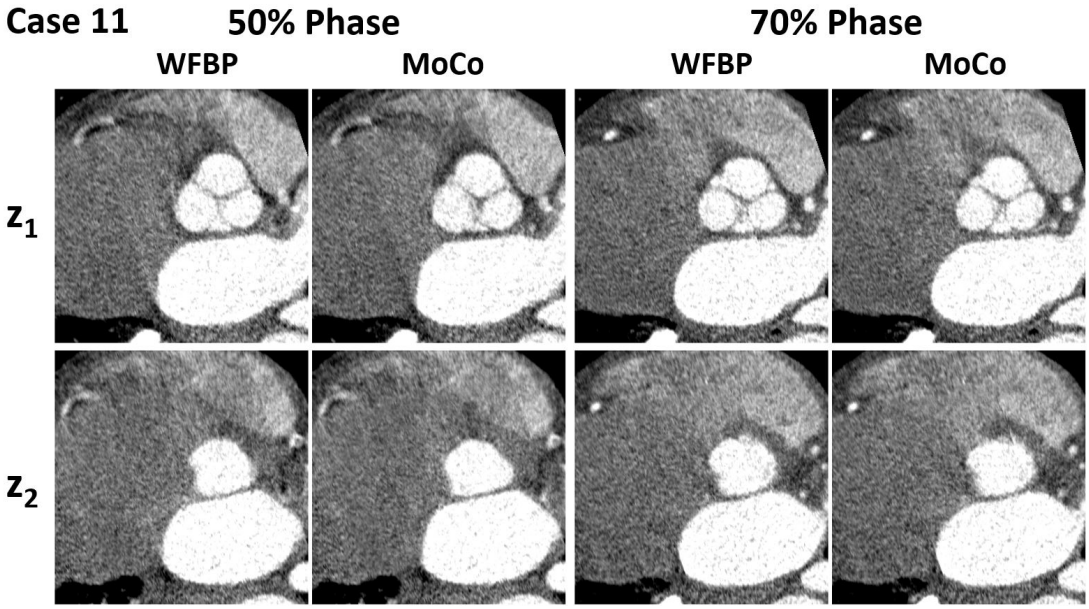

Figure B.10: Valve MoCo results for case 11. $C = 200$ HU, $W = 1200$ HU.

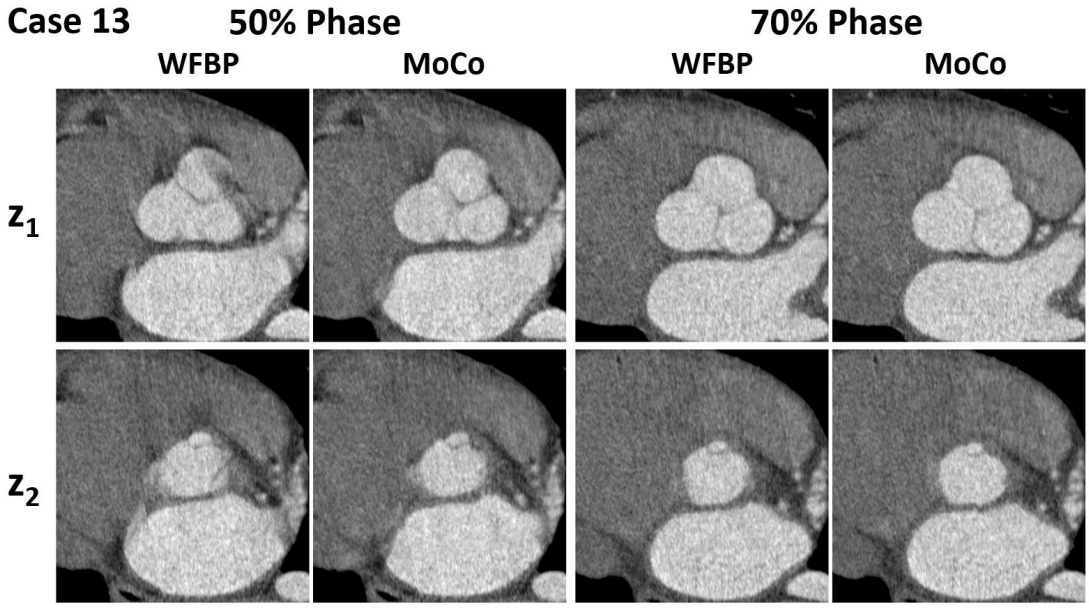

Figure B.11: Valve MoCo results for case 13. $C = 200$ HU, $W = 1200$ HU.

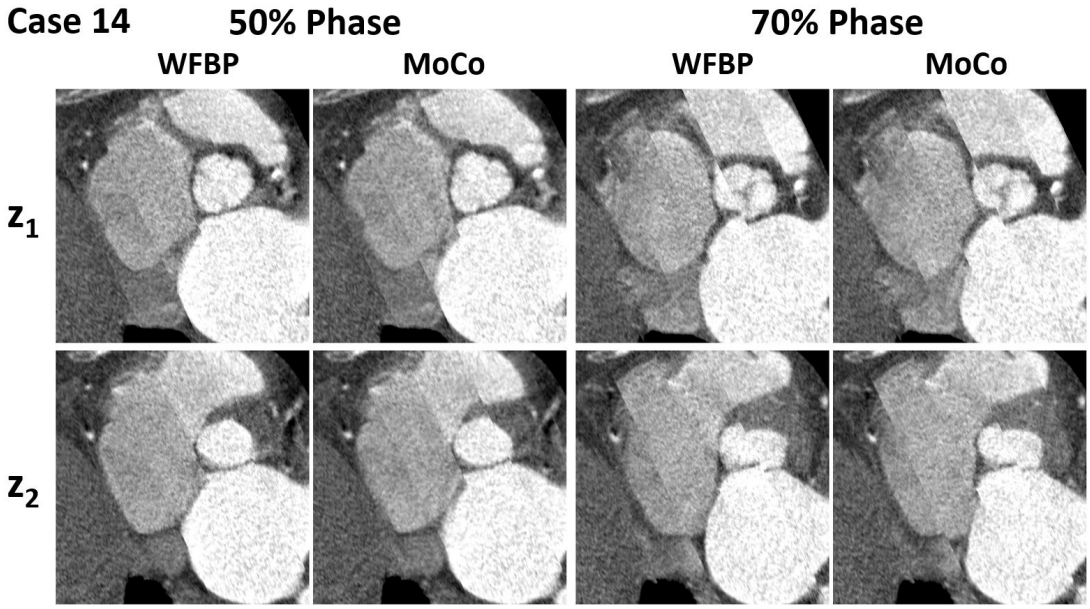

Figure B.12: Valve MoCo results for case 14. $C = 200$ HU, $W = 1200$ HU.

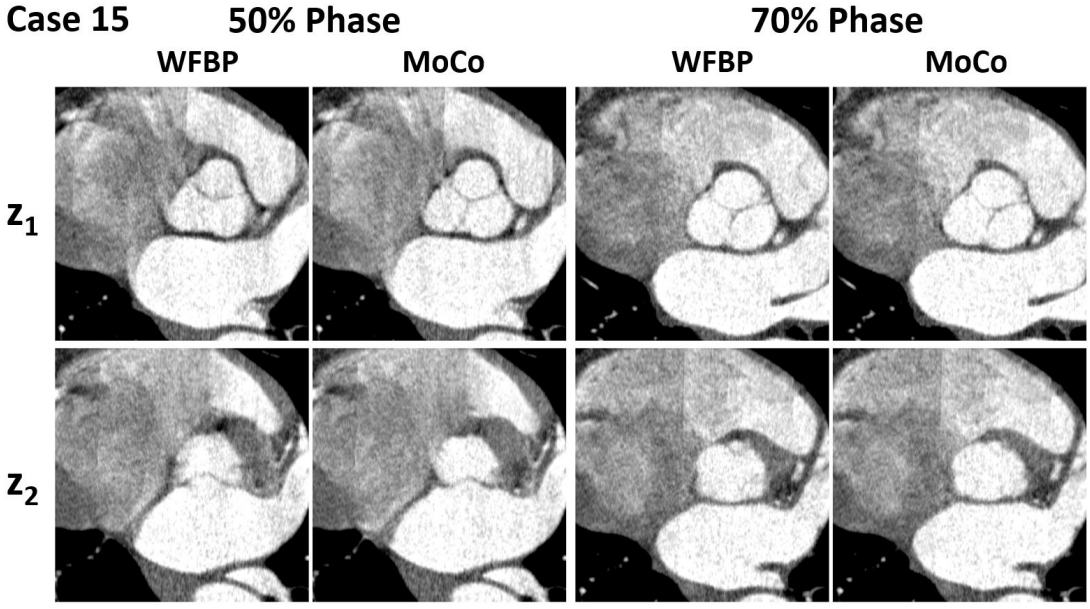

Figure B.13: Valve MoCo results for cases 15. $C = 200$ HU, $W = 1200$ HU.

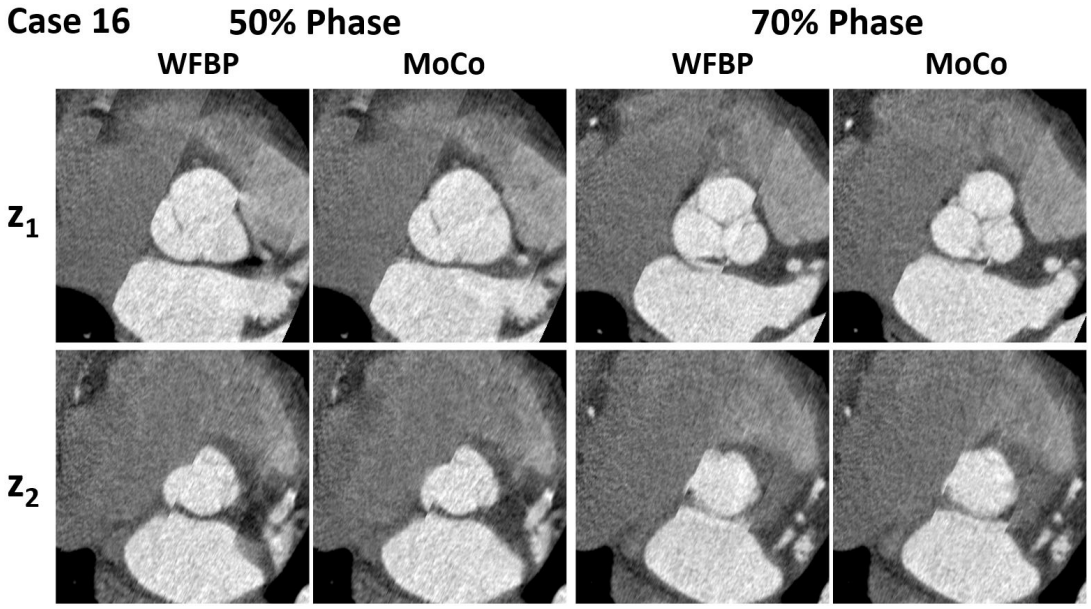

Figure B.14: Valve MoCo results for cases 16. $C = 200$ HU, $W = 1200$ HU.

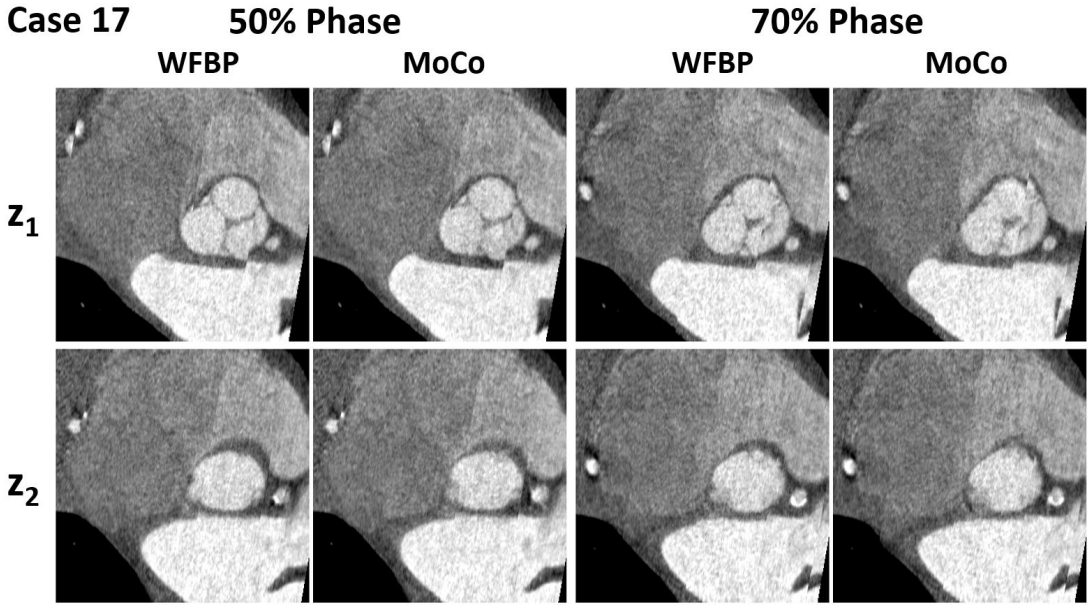

Figure B.15: Valve MoCo results for cases 17. $C = 200$ HU, $W = 1200$ HU.

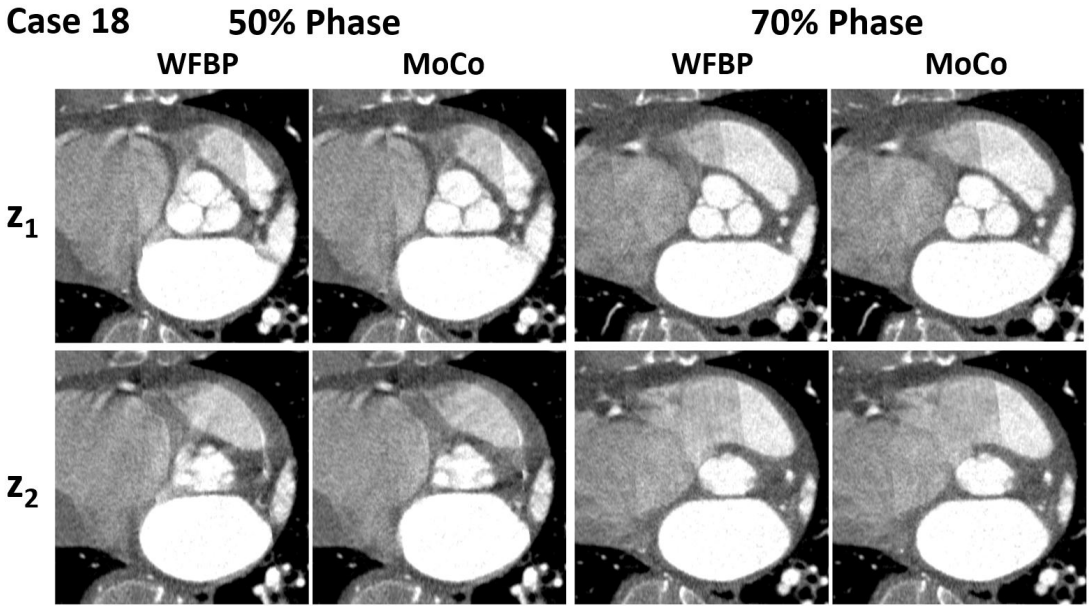

Figure B.16: Valve MoCo results for case 18. $C = 200$ HU, $W = 1500$ HU.

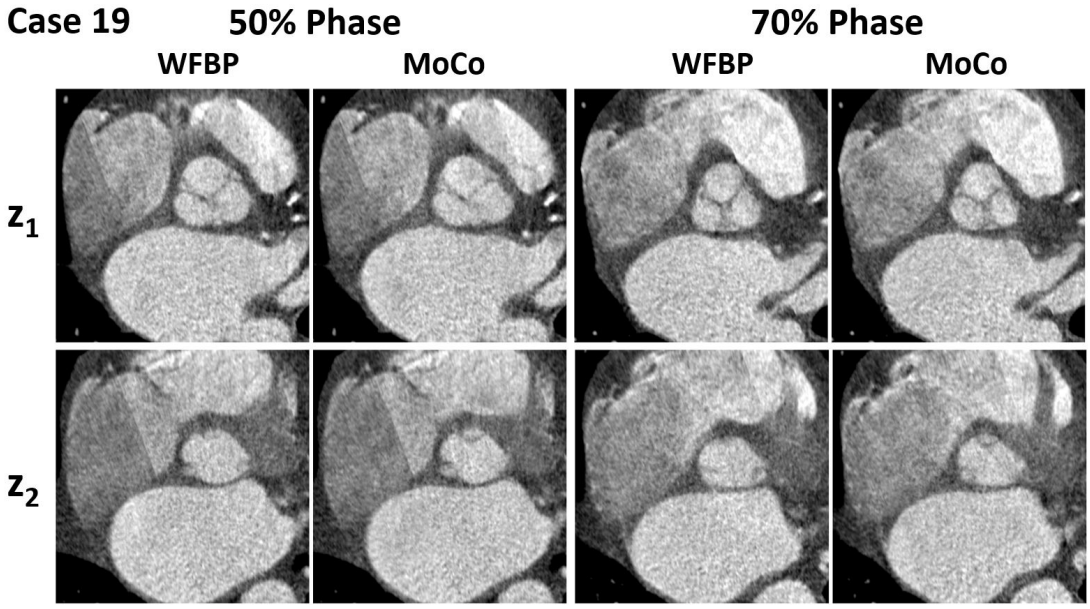

Figure B.17: Valve MoCo results for cases 19. $C = 200$ HU, $W = 1200$ HU.

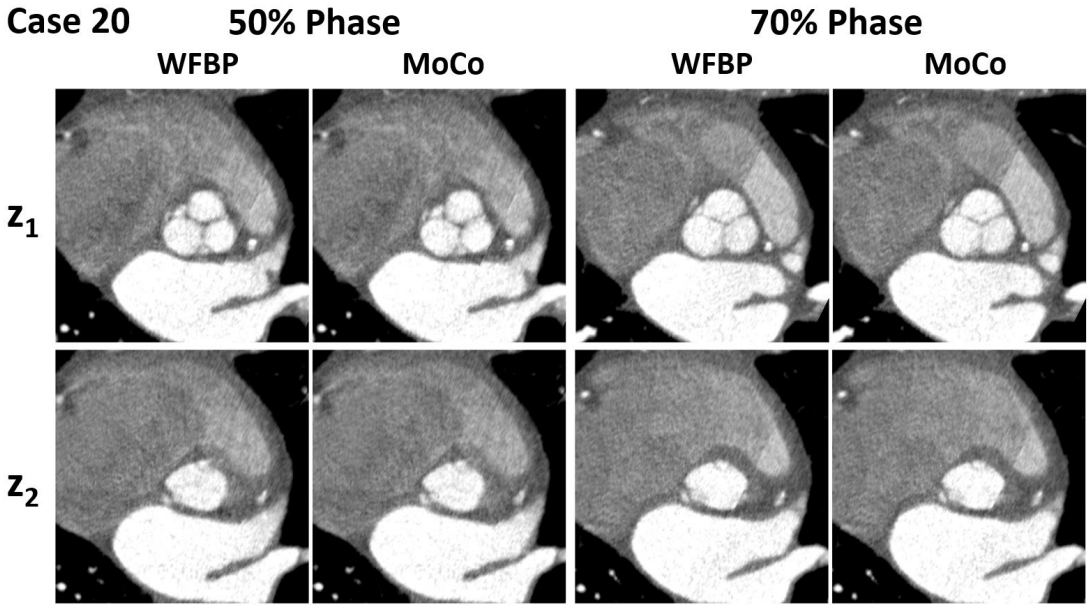

Figure B.18: Valve MoCo results for cases 20. $C = 200$ HU, $W = 1500$ HU.

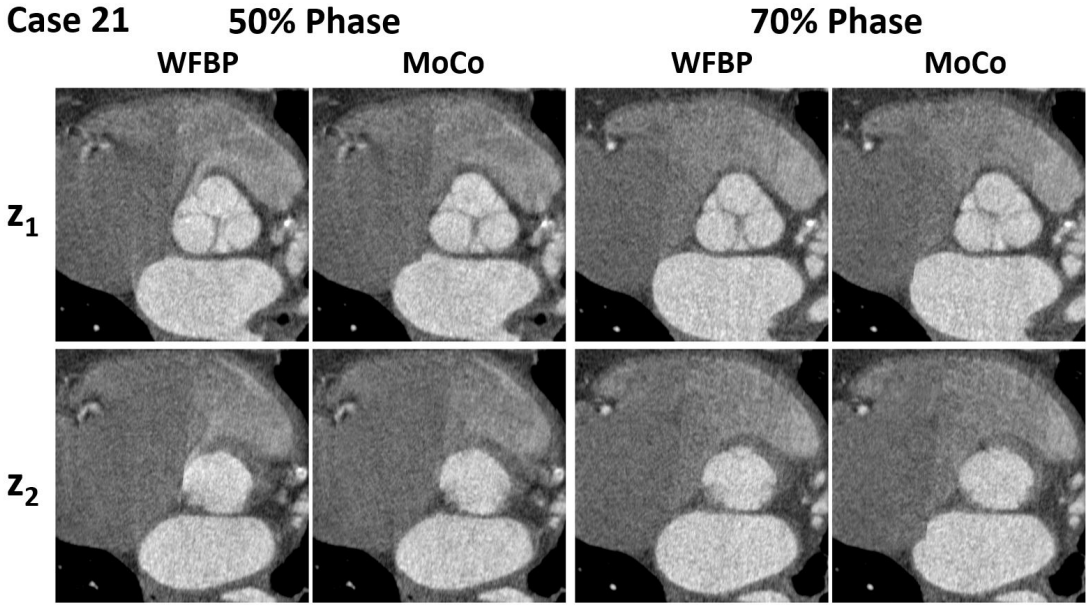

Figure B.19: Valve MoCo results for case 21. $C = 200$ HU, $W = 1200$ HU.